QUANTITATIVE ACETONE PLIF MEASUREMENTS OF JET MIXING WITH SYNTHETIC JET ACTUATORS

A Dissertation
Presented to
The Academic Faculty

by

Brian D. Ritchie

In Partial Fulfillment
Of the Requirements for the Degree
Doctor of Philosophy in Aerospace Engineering

Georgia Institute of Technology

May 2006

Quantitative Acetone PLIF Measurements of Jet Mixing with Synthetic Jet Actuators

Approved by:

Dr. Jerry Seitzman, Advisor
School of Aerospace Engineering
Georgia Institute of Technology

Dr. Tim Lieuwen
School of Aerospace Engineering
Georgia Institute of Technology

Dr. Jeff Jagoda
School of Aerospace Engineering
Georgia Institute of Technology

Dr. Ari Glezer
School of Mechanical Engineering
Georgia Institute of Technology

Dr. Suresh Menon
School of Aerospace Engineering
Georgia Institute of Technology

Date Approved: April 10, 2006

ACKNOWLEDGEMENTS

I would like to thank all of the people who made this possible. My advisor, Dr. Jerry Seitzman, taught me the skills necessary to do the work and helped guide me around the pitfalls along the way. Several students assisted me with parts of this research along the way, especially Thao Tran, Dilip Mujumdar and Mark Birney. Drs. Ari Glezer and Staci Davis of the Mechanical Engineering Fluid Mechanics Research Lab provided insight into the synthetic jet actuators, technical assistance with the velocity measurements in this system and all the velocity measurements in their similar rig. All the teachers and professors along the way that helped guide me onto this path also earned my heartfelt gratitude. For financial support, I need to thank the Army Research Office, MicroCoating Technologies and General Electric.

My deepest thanks go to my parents for making this possible. I need to thank my friends for helping me get through the process, too. Thanks to Dr. Rick Wainner for showing me the ropes and to Brian Scully for putting up with all the noise. Special thanks to Master Nils Onsager, Dr. Paul Gay, Dr. George Parlavantzas, Melissa Johnson and the rest of the gang for providing me with life skills, character development, bumps, bruises, stress relief and most importantly great friendship. I could not have asked for better friends and would not have made it without you.

TABLE OF CONTENTS

LIST OF TABLES

LIST OF FIGURES

NOMENCLATURE

A	area
B	background signal
C	constant, concentration
D	jet diameter
d	droplet diameter
E	laser energy
E'	laser energy correction coefficient
F	fluorescence
f	mixture fraction, mole fraction, focal length
f'	RMS mixture fraction fluctuations
$\bar{f}$	average mixture fraction
h	width of synthetic jet exit
I	laser intensity
K	absorption coefficient
L	path length
MW	molecular weight
m	mass
N	number of molecules
n	number of moles, number density, index of refraction
P	pressure, phosphorescence
r	radial coordinate

S	signal
T	temperature
t	time, pixel size
U	axial velocity
u'	axial velocity fluctuation
V	radial velocity
x	axial coordinate
α	absorption coefficient
η	fluorescence efficiency
λ	wavelength
ρ	density
μ	viscosity
σ	absorption cross-section, surface tension
Φ	phase
χ	mole fraction
Δ	voxel size
Δx	difference in axial distance

Subscripts

0	initial value
d	droplet
i	inner jet
o	outer jet
ref	reference value
v	vapor

SUMMARY

Fuel-air mixing enhancement in axisymmetric jets using an array of synthetic jet actuators around the perimeter of the flows (primarily parallel to the flow axis) was investigated using planar laser-induced fluorescence of acetone. The synthetic jets are a promising new mixing control and enhancement technology with a wide range of capabilities. An image correction scheme that improved on current ones was applied to the images acquired to generate quantitative mixing measurements. Both a single jet and coaxial jets were tested, including different velocity ratios for the coaxial jets. The actuators run at a high frequency (~1.2 kHz), and were tested with all of them on and in other geometric patterns. In addition, amplitude modulation was imposed at a lower frequency (10-100 Hz).

The actuators generated small-scale structures in the outer (and inner, for the coaxial jets) mixing layers. These structures significantly enhanced the mixing in the near field ($x/D < 1$) of the jets, which would be useful for correcting an off-design condition in a combustor. The amplitude modulation generated large-scale structures that became apparent farther downstream ($x/D > 1$). The impulse at the start of the duty cycle was responsible for creating the structures. The large structures contained broad regions of uniformly mixed fluid, and also entrained fluid significantly. In addition, highly asymmetric forcing geometries displayed the power of the actuators to control the spatial distribution of jet fluid. This spatial control is important for the correction of hot spots in the pattern factor.

In order to extend quantitative acetone PLIF to two-phase flows, the remaining unknown photophysical properties of acetone were identified. Tests showed that the technique could simultaneously capture acetone vapor and acetone droplets. A model of droplet fluorescence was developed, and applied to images acquired in a dilute spray. The sensitivity of the model to the value of the unknowns was evaluated, including a best and worst case. The results revealed that several liquid acetone photophysical properties must be measured for the further development of the technique, especially the phosphorescence yield. Quantitative two-phase acetone PLIF will provide a powerful new tool for studying spray flows.

CHAPTER 1

INTRODUCTION

Enhancing and controlling fuel-air mixing is important for modern combustion systems, and requires an understanding of mixing processes in systems typical of practical combustors. Changes in fuel-air mixing can lead to the reduction of pollutants, improved combustor efficiency, reduced combustor size, longer engine lifetimes and greater stability or operability.[1] While modern combustors perform quite well at specific design conditions, one area of concern is performance during off-design conditions, such as a high-altitude re-light of an aircraft engine. Improvements in off-design performance can be achieved through control and enhancement of the mixing process, but there are several constraints on the techniques that may be used.

Engines operate in off-design conditions for relatively short periods of time. This implies that the mixing control and enhancement system should be lightweight to minimize the penalty on normal performance, and of minimum complexity to maximize the reliability of the system. However, the system also needs to be very flexible to provide the ability to make large changes to correct for a variety of problems. A plugged fuel-injector requires spatial redistribution of the available fuel and air, while a high-altitude re-light requires the best possible fuel-air mixing to use what little air is currently available. In essence, the technique needs to work on both the large-scale stirring and the small-scale mixing.

Mixing Enhancement

Many mixing enhancement and control techniques have been used over the years. One common method is to change the geometry of the flow[1] to enhance the mixing. This is effective at mixing enhancement, but a passive technique is not helpful for a sudden off-design condition and does not provide spatial control. In fact, a passive system cannot meet all the requirements for controllability, although the simplicity of a passive system is desirable. The question then becomes what type of active technique is flexible enough for the purpose, yet minimizes the complexity of the system. There are many active control techniques in use, though. For example, one can temporally modulate the fuel or air flow, but this does not provide the desired azimuthal control. The addition of secondary air and fuel flows can provide the required spatial and temporal control, but requires a complex and bulky system that is undesirable for an aircraft engine. Other active mixing enhancement methods suffer from these and additional flaws. However, acoustic excitation at a natural frequency of the flow[2] is the only method of strong forcing to previously receive study in mixing measurements. Acoustic forcing is able to distort the jet shape of a round jet and increase the entrainment.[3] Forcing the annular flow in coaxial jets greatly affects the flow in both streams while forcing of the center jet did not have a significant effect on the outer flow,[4] leading to the conclusion that forcing of the annular flow is the most effective method to enhance mixing. Since these traditional methods are not suitable for the problem at hand, however, a new method is desirable. One method that has been suggested recently is to use synthetic jet actuators.[5]

Previous experimental study of synthetic jet actuators has focused on fluid mechanical effects and velocity measurements.[6,7] Synthetic jet actuators generally maintain either a constant frequency but varying amplitude (e.g., devices based on piezolelectric-driven membranes) or a constant displacement with variable frequency (e.g., driven piston systems). While some work has been done showing the impact of piston-based synthetic jet system on pattern factor downstream of a combustor,[8] a piezoelectric-driven vibrating membrane can run at a much higher frequency than a moving piston, has a variable strength, and is easy to control electronically. This type of synthetic jet has been modeled,[9,10] including the potential mixing enhancement.[11,12] The ability to use digital control implies that a lower frequency can be used to modulate the high frequency signal, potentially resulting in both large-scale and small-scale effects from the actuator. Velocity measurements indicate that piezoelectric synthetic jet actuators can in fact affect both the small and large scales.[13] However, the current body of work lacks mixing measurements to show the effectiveness of synthetic jet actuators for large- and small-scale mixing enhancement and control.

Jet Mixing

In the effort to evaluate mixing enhancement in a laboratory setting, free jet flows were used to simulate the flows of interest. Both an axisymmetric single jet and co-axial jets were used to provide a deeper understanding of the effects of the mixing enhancement devices. Jet flows have been studied extensively, but relatively little of the research is directly relevant to this work. Most jet research examined the far field of the

jet, not the near field (less than 5 jet diameters downstream) of interest in this investigation. Even less work focused on making quantitative, scalar mixing measurements in this field of interest. There are some key points that can be drawn from prior work, though.

Single jet work has found that fully developed pipe flow mixes on the centerline faster than a jet with a top-hat velocity profile.[14,15] It was also observed that large-scale structures dominate near field mixing.[16] Several investigations that did measure mixing[17,18,19] found that the Broadwell-Briedenthal model[20] of shear flow mixing held for their results. Coaxial jet flow studies[21,22,23] have found that the area ratio, velocity ratio and absolute velocities are the dominant variables affecting the flow. Interaction of the two flows is enhanced when the inner jet is slower than the annular jet ($U_i/U_o < 1$)[24] and reducing the area of the annular jet increases the effect.[24]

Mixing Measurement

An appropriate mixing-measurement technique to evaluate synthetic jet actuators should provide non-invasive, temporally- and spatially-resolved mixture fraction measurements, preferably down to very small spatial scales where diffusion ensures good molecular mixing, with a minimum of complexity. Non-invasiveness suggests use of an optical technique as opposed to an intrusive technique like gas sampling. Optical diagnostics vary in terms of resolution, though. Absorption techniques are simple and temporally-resolved, but lack spatial resolution since they average across the line of sight.[25] Rayleigh scattering[26] provides total density, requiring a large density difference

between the fuel and air to see mixing to low levels of fuel, and suffers from interference due to particles and spurious scattered laser light. Raman scattering[27] struggles to provide quantitative results over a large range of mixture fractions due to the low signal strength, and has a relatively large noise level. Planar laser-induced fluorescence (PLIF) is a good choice for gas-gas mixing measurements because it yields quantitative two-dimensional images of the flow field and is a proven approach for non-invasive measurements.[28] In order to maximize the quantitativeness of the results from PLIF, however, correction for several error sources must be made. While a complete correction scheme has been outlined previously,[29] no work in the literature has truly applied all of them. The choice of fluorescing molecule is also important to obtain the best results. For fuel-air mixing measurements, acetone is especially attractive[30] for reasons that will be covered in detail in Chapter 2. Acetone PLIF has proven to be a diverse and powerful technique, used for concentration measurements in a variety of flow fields including jets in cross-flow[31], supersonic flows[32] , heated non-reacting flows[33,34,35,36] and combusting flows.[37,38] It has also been used to measure multiple parameters simultaneously[39,40] in gaseous flows. In addition, the temperature[41,42] and pressure[43,44] dependencies of acetone fluorescence have been measured recently, along with excitation wavelength and ambient gas effects.

Two-Phase Measurement

While gaseous systems are of interest, liquid fuels are also very common and require non-intrusive, quantitative, spatially- and temporally- resolved gas-gas and two-phase mixture fraction measurements. Obtaining all of this from one technique would be ideal, minimizing the amount (and expense) of equipment and the complexity of the experimental setups required. Scattering can be used to measure the size, location and velocity of droplets or particles with good resolution, but scattering techniques are more difficult to use for gas-gas mixing.[25] Another common method used in the engine industry is to measure droplets with fluorescence from exciplexes.[45,46] An exciplex is an excited-state complex that requires doping the liquid, however, and the fluorescence is strongly quenched by oxygen[47] requiring an enclosed volume filled with no air if vapor measurements are desired. A related option used in industry is to use fuel fluorescence itself,[48] but this introduces the unknowns of the exact fuel composition and the photophysical properties of those components in addition to providing a nasty imaging environment.

PLIF of a fuel substitute can also have difficulties in two-phase flows, however. While fluorescence and scattering can be combined with some difficulty to improve the measurement, obtaining quantitative two-phase mixture fraction measurements from one technique would be better. Acetone PLIF has been used for quantitative vapor concentration measurements in two-phase flows before,[49] but the data was cut off whenever a droplet large enough to produce a signal greater than that from one pixel of the vapor in the flow field was encountered. Extending acetone PLIF to simultaneously

measure liquid and vapor mixture fraction without also using scattering would be a definite improvement over the current choices.

Outline

Chapter 2 provides a background on synthetic jets and acetone PLIF as a measurement technique in gaseous and two-phase flows. It also discusses a new model of acetone droplet fluorescence. Chapter 3 details the experimental setups and measurement methods used in this work. Chapter 4 presents qualitative imaging results, demonstrating the range of effects synthetic jet actuators can have on the flow fields. Chapter 5 provides quantitative results for mixing enhancement by synthetic jets on a single jet and on coaxial jets. Chapter 6 applies acetone PLIF to two-phase flows, uses the droplet model from Chapter 2 to calculate some numerical results, and explores what additional knowledge is needed to extend quantitative acetone PLIF to two-phase flows. Chapter 7 contains conclusions from the research and suggestions for future work.

CHAPTER 2

BACKGROUND

Synthetic Jets

A synthetic jet actuator is a zero net-mass-flux momentum-transfer device. The actuator is a cavity with an opening and a movable wall such as a vibrating membrane or piston (Figure 2.1). The motion of the wall sucks in gas from all directions in the flow and then ejects the gas in a directed jet of much higher velocity. Synthesis of the periodic flow caused by alternating suction and blowing through the actuator orifice creates a synthetic jet. Synthetic jet actuators are fairly simple since they require no external plumbing. They also offer the promise of spatial control since they can be distributed spatially and controlled individually.

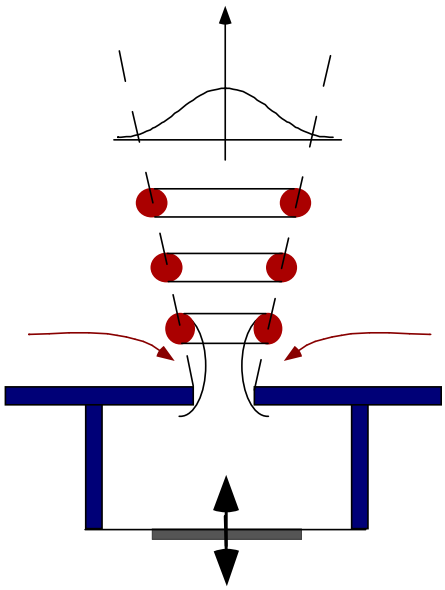

Figure 2.1. Schematic of a synthetic jet.

Acetone PLIF

Fluorescence

Luminescence occurs when excited molecules spontaneously emit light to relax to a lower energy state (usually the ground electronic state). If the excited and ground states share the same spin multiplicity (both are singlet states or both are triplet states), this process is called fluorescence. If the two states have different spin multiplicities (triplet to singlet or singlet to triplet), the process is called phosphorescence. Fluorescence is generally much faster than phosphorescence because the change in spin multiplicity is an unlikely event, often called a forbidden transition. Laser-induced fluorescence denotes a process in which the absorbing molecules are electronically excited by a laser beam of a

properly chosen wavelength. Optically converting the laser beam to a thin laser sheet yields planar laser-induced fluorescence.

Acetone

Acetone vapor luminescence has been studied for many years.[50,51,52,53] The research has continued to improve[54,55,56,57] as the available equipment has improved, but the work has focused on fluorescence[58,59,60,61] more than phosphorescence. The range of testing conditions, from near vacuum to atmospheric pressure and near to mid-UV excitation, has also lead to multiple studies of acetone's properties.[62,63,64,65,66,67]

Acetone has many advantages over other fluorescing alternatives. Most importantly, acetone fluorescence in isobaric, isothermal flows is known to scale linearly with concentration (and laser power under most conditions),[30] which is not true for many fluorescing molecules. At atmospheric conditions, the fluorescence yield of acetone is limited by rapid intersystem crossing from the first excited singlet state (S1), which fluoresces, to the first excited triplet state (T1), which phosphoresces (Figure 2.2). In the absence of O_2, the integrated phosphorescence emission for acetone vapor is stronger than its fluorescence; the phosphorescence yield is 1.8% to just 0.2% for the fluorescence yield.[68] Phosphorescence also has a much longer lifetime in vapor (200 μs versus 4 ns for fluorescence).[68]

While the two emissions can be separated temporally, spectral separation is difficult due to significant overlap of the spectra. Because acetone fluorescence is so short-lived, it is not significantly quenched by oxygen unlike many other fluorescing molecules.

However, the phosphorescence is strongly quenched by oxygen,[68] leaving just a strong fluorescence signal in the conditions in these experiments. Also, acetone absorbs ultraviolet light (225 - 320 nm) but fluoresces in the blue (350 - 550 nm). Elastically scattered light is easily filtered out by simple glass optics since the absorption and emission spectra do not overlap. Finally, acetone is much less toxic than many alternative molecules. Although prolonged exposure should be avoided, breathing small amounts of acetone vapor does not present a serious health risk.

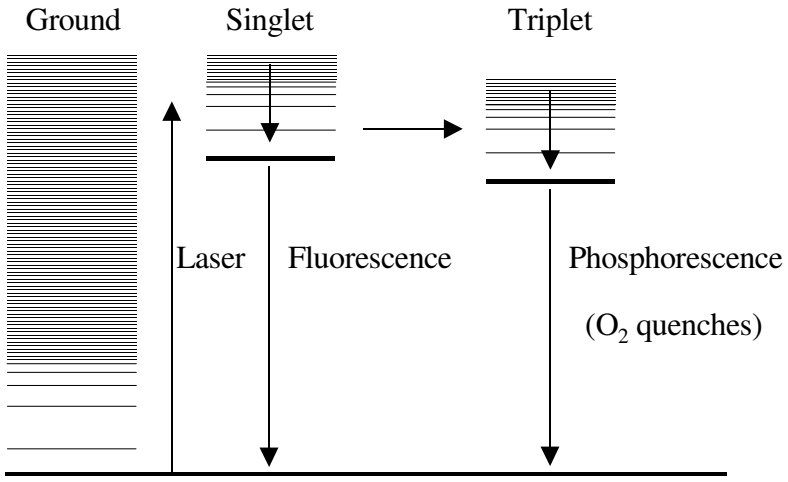

Figure 2.2. Diagram of acetone photophysics.

Measuring Mixture Fraction

The concentration field of acetone can be converted to mixture fraction, a measure of the average mixedness of the small volume imaged into a pixel, by using Equation 2.1. The mixture fraction (f) is defined as the ratio of the mass of fluid that originated from

one source to the total mass in a measurement volume (the extra mass having come from elsewhere). This investigation is focused on acetone-seeded jets into ambient air, so f = 1 for pure jet fluid and f = 0 for pure air. The source of the air (ambient or from another jet for a coaxial jet case) is immaterial to the mixture fraction of acetone.

The substitution of known values into the mixture fraction equation, as seen in Equations 2.1a - 2.1g, leads to the practical form of the equation shown as Equation 2.2. Starting from the original definition of the mixture fraction in Equation 2.1, the total mass is broken in to the sum of jet fluid and other fluid. Both the numerator and the denominator on the right side of the equation are then divided by the mass of jet fluid.

$$f \equiv \frac{m_{jet}}{m_{total}} = \frac{m_{jet}}{m_{jet} + m_{other}} = \frac{1}{1 + m_{other} / m_{jet}} \tag{2.1}$$

Equation 2.1a pulls out the ratio of the mass of other fluid to the mass of jet fluid. The mass is redefined as the product of the number of moles and the molecular weight of each type of fluid, netting the product of the ratio of the number of moles and the ratio of molecular weights.

$$\frac{m_{other}}{m_{jet}} = \frac{n_{other}}{n_{jet}} \frac{MW_{other}}{MW_{jet}} \tag{2.1a}$$

Equation 2.1b reduces the ratio of number of moles even further. First, it replaces the number of moles of other fluid with the total number of moles minus the jet fluid number

of moles. Dividing through by the total number of moles, it leaves the ratio of the number of moles of jet fluid to the total number of moles as the lone variable.

$$\frac{n_{other}}{n_{jet}} = \frac{n_{total} - n_{jet}}{n_{jet}} = \frac{1 - n_{jet} / n_{total}}{n_{jet} / n_{total}} \tag{2.1b}$$

Equation 2.1c simplifies the ratio of the number of moles by renaming it as the concentration of jet fluid. The concentration is also equal to the ratio of the number of moles of acetone at that location to the number of moles of acetone at the jet exit.

$$C \equiv \frac{n_{jet}}{n_{total}} = \frac{n_{acetone}}{n_{acetone,exit}} \tag{2.1c}$$

Substituting concentration back into Equation 2.1b results in Equation 2.1d.

$$\frac{n_{other}}{n_{jet}} = \frac{1 - C}{C} \tag{2.1d}$$

Equation 2.1e recognizes the experimental conditions of this research by defining the other fluid as air for the molecular weight.

$$MW_{other} = MW_{air} \tag{2.1e}$$

Similarly, Equation 2.1f redefines the jet fluid to fit the experiments. The molecular weight of the jet fluid is the sum of two things, the product of the concentration and molecular weight of acetone, and the product of the concentration and molecular weight of air.

$$MW_{jet} = C \cdot MW_{acetone} + (1 - C) MW_{air} \tag{2.1f}$$

Equation 2.1g combines the new molecular weight definitions from Equations 2.1e and f to redefine the ratio of molecular weights.

$$\frac{MW_{other}}{MW_{jet}} = \frac{1}{C \dfrac{MW_{acetone}}{MW_{air}} + (1 - C)} \tag{2.1g}$$

The substitution of Equation 2.1g into Equation 2.1a results in the final mass ratio equation, Equation 2.1h, in terms of the concentration and the molecular weights of air and acetone.

$$\frac{m_{other}}{m_{jet}} = \frac{\dfrac{(1 - C)}{C}}{C \cdot \dfrac{MW_{acetone}}{MW_{air}} + (1 - C)} \tag{2.1h}$$

Inserting Equation 2.1h into the original definition of mixture fraction (Equation 2.1) results in Equation 2.2. This new equation defines the mixture fraction in terms of just

the concentration (measured experimentally), the molecular weight of air (known) and the molecular weight of the acetone jet (measured experimentally).

$$f = \frac{1}{1 + \frac{\frac{1-C}{C}}{C \cdot \frac{MW_{acetone}}{MW_{air}} + (1-C)}} \tag{2.2}$$

The reasons why the molecular weight of the acetone jet is not known a priori in these experiments are discussed in Chapter 3.

Liquid

A key to making quantitative PLIF measurements in multiphase flows can be distinguishing between the signal coming from different phases. For example, acetone vapor and acetone droplets will both fluoresce when excited by a laser. However, the spectra from both phases are very similar, so the phases cannot easily be distinguished spectrally.[49] In general, the photophysical properties of liquid acetone[69,70,71,] are less well understood than for vapor and have been less studied.[72,73,74] If the fluorescence is being imaged with a camera, and if the droplets are sufficiently larger than the size of a pixel, the droplets can be discriminated from the gas based on their spatial pattern (shape). Thus, phase discrimination is primarily an issue for subpixel-sized droplets. Acetone PLIF has been used in multiphase flows before, but not to provide quantitative measurements of the liquid phase.[49]

The large density difference between the phases, however, leads to a solution. The higher density of liquid acetone (~750× the vapor density at standard conditions) leads to much larger signals from droplets compared to vapor of the same volume. Thus, signal strength can be used to separate liquid from vapor acetone, but only for droplets larger than some minimum critical diameter. The reason is the very short optical depth (≈18 μm)[49] of liquid acetone for ultraviolet wavelengths. For particle diameters somewhat larger than the optical depth, the liquid in the droplet beyond the optical depth does not contribute to the fluorescence signal, as the laser energy is nearly depleted after being absorbed by the liquid.

The liquid absorption also impacts acetone PLIF measurements of the vapor phase. Behind droplets, which can be highly absorbing to the laser energy as noted above, the laser energy will be reduced. If a droplet is large enough (e.g., a significant fraction of the height of a pixel or the thickness of the laser sheet), making measurements of acetone vapor in the "shadow" of the droplet becomes more difficult as the local laser intensity will be unknown. This limits the usefulness of two-phase acetone imaging in dense spray regions. Since the strong absorption limits the maximum signal from large droplets, though, the dynamic range of the camera required to view both droplets and low vapor concentrations is reduced.

Droplet Model

In order to discriminate the signal produced by subpixel-sized droplets from the signal for vapor, a model of the droplet PLIF signal is needed. For example, it would be

helpful to calculate a "cutoff" diameter for distinguishing the two phases. For droplets above this cutoff size, the PLIF signal from the liquid would exceed the maximum possible signal from a volume of vapor. Thus droplets above this size could be discriminated from vapor regions based on signal strength, while smaller droplets could not be distinguished. Such information would be useful, for example, in comparing to computational fluid dynamics (CFD) codes for evaporating sprays. Such codes typically track droplets as they move and evaporate only down to some minimum diameter; beyond that point, the droplet is assumed to evaporate instantly. Tracking smaller droplets becomes too computationally expensive. Experiments that can only distinguish down to 100 μm droplet diameters would be of little help if the code tracks them down to 5 μm. However, if the experiments and computations have similar droplet thresholds, then the data can be meaningfully compared.

A simple model to account for droplet fluorescence has been given for a spherical droplet with an index of refraction that matches the vapor value.[49] This choice of refractive index eliminates reflection and refraction at the surface. The model was also derived for a top hat laser profile, with the droplet always entirely inside the sheet, and square camera pixels. In this case, the fluorescence is given by Equation 2.3:

$$S_d \equiv \frac{\eta}{2} I_0 \pi d^2 \left(1 - e^{-\frac{Kd}{3}} \right) \tag{2.3}$$

where d is the droplet diameter, K is the absorption coefficient, and η is the fluorescence efficiency.

This approximation shows that the fluorescence is proportional to volume for small droplets (Kd/3 << 1) while it scales like surface area for large droplets. Experimental results do not fit this model, however. Acetone has an index of refraction of 1.36, resulting in reflection and refraction at the droplet surface. A modified model, which reduces to the original for n = 1, was proposed[49] to account for this, and is given by:

$$S_d \equiv \frac{\eta}{2} I_0 \pi d^{(3-n)} \left(1 - e^{-\frac{Kd^n}{3}} \right) \tag{2.4}$$

It was found that an index of refraction (n) of 1.43 best fit the data. Potentially this could be a dispersion effect resulting from aspherical droplets. Building on this model, we consider a more realistic treatment of reflection and refraction effects, while maintaining the assumption of spherical droplets.

The current model calculates two basic parameters for each phase of acetone in a pixel, the fluorescence signal emitted and the extinction of laser light due to the acetone. Extinction combines two forms of loss, absorption by the acetone and scattering out of the plane by reflection or refraction.

The normalized fluorescence signal from the acetone vapor in the pixel, according to Beer's Law, [25] is given by Equation 2.5.

$$\frac{S_v}{I_0} = \sigma_v N_v t^3 \left(\frac{t}{t_{ref}} \right)^2 \tag{2.5}$$

In the case of acetone vapor, the scattering due to acetone molecules is ignored. This results in a pixel extinction coefficient due to vapor only (PEC_v), where extinction is only due to absorption, given by:

$$PEC_v = 1 - e^{-\sigma_v N_v t} \tag{2.6}$$

where σ_v is the absorption cross-section of acetone vapor, and N_v is the number density of acetone vapor. The droplet signal is calculated from the model given above. For practical purposes, it is easier to work with the normalized fluorescence signal given from a droplet rather than the absolute value. Thus, Equation 2.4 becomes Equation 2.7.

$$\frac{S_d}{I_0} = \frac{\pi}{2} d^{3-n} \left(1 - e^{-\frac{K_d d^n}{3}}\right) \left(\frac{t}{t_{ref}}\right)^2 \tag{2.7}$$

where t_{ref} is a reference sheet thickness used to maintain constant energy in the laser sheet instead of a constant intensity as the sheet thickness changes. The new model uses computations based on basic light scattering principles for spherical droplets to calculate the pixel extinction coefficient for a droplet (PEC_d). Tabulated data[75] for water droplets (n = 1.34 versus 1.36 for acetone) were used to calculate several numbers as a first order approximation. The droplets of interest (d > 10 μm) were calculated to be very large ($\pi d/\lambda >> 1$), so the tabulated results for very large water droplets were used. The tables presented the fraction of the incident energy that is externally reflected, refracted but

passes through, and is internally reflected before passing through for ranges of the final light ray angle.

First, the percentage of light reflected from the droplet surface was calculated to be 7.7% while the amount of light scattered out of the plane of the laser sheet was 12.2% (reflection + refraction). The average path length for a light ray through a droplet, allowing for internal reflections, was found to be 0.90 times the droplet diameter. Equation 2.8 gives the basic form of the pixel extinction coefficient.

$$PEC_d = 1 - (Scattering + Absorption) \tag{2.8}$$

In order to calculate the extinction from a droplet, first the area ratio of the droplet to the pixel area is calculated in Equation 2.8a.

$$\frac{A_d}{A_{pixel}} = \frac{\pi\left(\frac{d}{2}\right)^2}{t^2} = \pi\left(\frac{d}{2t}\right)^2 \tag{2.8a}$$

Next, the absorption is calculated for the liquid just as for the vapor in Equation 2.8b using the calculated mean path length for a light ray.

$$Absorption = e^{-0.90dK_d} \tag{2.8b}$$

where K_d is the absorption coefficient for liquid acetone. Since some of the light is

reflected from the droplet surface, the absorption is scaled by the fraction of incident light that actually enters the droplet in Equation 2.8c.

$$Absorption = 0.923e^{-0.90dK_d} \tag{2.8c}$$

Now all three forms of extinction are summed in Equation 2.8d.

$$Extinction = 0.122 + 0.923e^{-0.90dK_d} \tag{2.8d}$$

This leads directly to the pixel extinction in Equation 2.8e, which scales the droplet extinction by the area ratio.

$$Pixel\ extinction = \pi\left(\frac{d}{2t}\right)^2\left(0.122 + 0.923e^{-0.90dK_d}\right) \tag{2.8e}$$

Equation 2.9 converts this into the pixel extinction coefficient for a pixel containing a droplet.

$$PEC_d = 1 - \pi\left(\frac{d}{2t}\right)^2\left(0.122 + 0.923e^{-0.90dK_d}\right) \tag{2.9}$$

Combining Equations 2.6 and 2.9 gives the total pixel extinction coefficient as seen in Equation 2.10.

$$PEC = 1 - \pi\left(\frac{d}{2t}\right)^2 \left(0.122 + 0.923e^{-0.90dK_d}\right) - e^{-\sigma_v N_v t} \tag{2.10}$$

The pixel extinction coefficient only has two variables, droplet diameter and acetone vapor number density. K_d and σ_v are physical constants for an isobaric and isothermal system and a known wavelength, while t is determined by the optics creating the laser sheet. Similarly, Equations 2.5 and 2.7 can be combined into Equation 2.11 for the total normalized fluorescence signal from a pixel, given by:

$$\frac{S}{I_0} = \frac{\pi}{2} d^{3-n} \left(1 - e^{-\frac{K_d d^n}{3}}\right)\left(\frac{t}{t_{ref}}\right)^2 + \sigma_v N_v t^3 \left(\frac{t}{t_{ref}}\right)^2 \tag{2.11}$$

which also has just droplet diameter and acetone vapor number density as variables. The model theoretically allows data analysis routines to use the signal and the extinction from a pixel to determine the combination of droplets and vapor based on two equations in two unknowns. Unfortunately, determining the PEC in experiments is too difficult to make this practical.

Using this model, we can compare the fluorescence signal from a droplet (Equation 2.7) to the fluorescence signal from vapor (Equation 2.5) though. The model calculates the length of one side of the pixel filled only with gas that is necessary to generate the same amount of fluorescence as a droplet of a given size using Equation 2.12.

$$Equivalent\ \ pixel\ size = \left[\frac{\rho_d / \rho_v}{K f_v} \frac{S_d}{I_0} \left(\frac{t}{t_0} \right)^2 \right]^{\frac{1}{3}} \tag{2.12}$$

The density ratio between liquid and pure vapor, ρ_d/ρ_v , is known for a given temperature. The mole fraction of acetone vapor, f_v, can be chosen as any attainable value for that temperature. S_d/I_0 is calculated with Equation 2.7 for a given droplet diameter.

CHAPTER 3

EXPERIMENTAL SETUP

The objectives of this research required quantitative mixing measurements in a variety of flow fields, including two-phase flows. In choosing a measurement approach, both accuracy and experimental simplicity were considered. The optical technique chosen as best suited to these goals was planar laser-induced fluorescence (PLIF) of acetone. The first set of experiments involved studying the control and enhancement of mixing by synthetic jets in gaseous flows. Experimentally, this called for developing a system for seeding acetone vapor into air flows of significant flow rate. Additionally, a versatile flow facility designed to match the dimensions of an existing system was constructed as well. Extending the measurement technique to multi-phase flows required adapting the gaseous flow facility to accommodate a spray nozzle. In addition, a proprietary spray system designed to create a lower flow rate spray with smaller droplets was put in place and tested over a range of operating conditions. This chapter begins with a description of the optical equipment used to acquire images in this study. This is followed by an explanation of the correction procedures used to convert the raw images into quantitative values. It concludes with descriptions of the facilities used to generate the various flow fields.

Imaging System

Laser Sheet

All the acetone imaging experiments employed a Continuum Powerlite 8000 frequency-quadrupled (266 nm) Nd:YAG laser beam. The 7 mm circular output beam of the laser was converted into a collimated sheet that was 80 mm tall. The sheet width, measured by traversing a razor blade across the width of the sheet to determine the full width at half of the maximum signal (FWHM), was 170 μm. As shown in Figure 3.1, the sheet was produced with one 1 m focal length (f_S) spherical lens to reduce the sheet thickness and a telescope consisting of two cylindrical lenses to provide the sheet height (f_{T1} = 0.040 m and f_{T2} = 0.75 m). The laser energy, measured by an Ophir L30A-EX laser power meter, was approximately 100 mJ per pulse. Based on the manufacturer's specifications, the temporal full-width at half-maximum value of the pulse was 7 ns. Converting the acquired images into quantitative images of local acetone concentration required correction for several error sources, and is discussed in detail below. To aid in making these corrections, additional data were acquired that involved using a second laser sheet. This secondary sheet was formed using the reflection off the front surface of the first lens (~ 4 mJ per pulse), which reflected off of a mirror (M) and was directed through a cylindrical lens (C) to create a thin sheet 7 mm tall. This sheet was directed near the exit of a small jet of acetone-seeded air taken from the inlet flow to the system

before hitting a stainless steel optical post. Both the small jet and post images were captured by the camera simultaneously with the data images, but were out of plane with the main laser sheet and offset to the left and right of the main flow field.

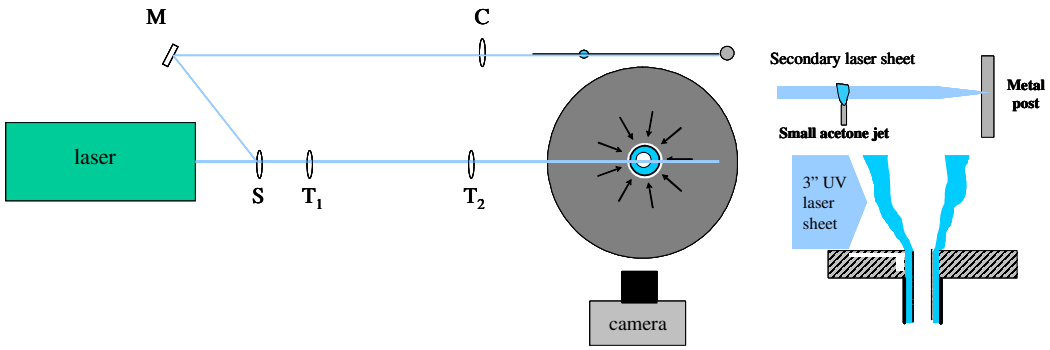

Figure 3.1. A top schematic view of the imaging setup along with a side view showing the field of view of the camera.

Camera

The images were acquired by a 1024×1024 pixel, Photometrics S300 CCD camera with ~70% quantum efficiency in the wavelength range of acetone fluorescence and a Nikkor 50 mm, f/1.8 glass photographic camera lens. The glass lens acted as an ultraviolet filter, preventing scattered laser light from generating signal on the camera. The camera employed a thinned, back-illuminated, UVAR coated, and Peltier-cooled CCD, which provided low light level sensitivity and a large signal dynamic range. The excellent spatial resolution of the system was also important since the acetone

concentration measurements could only be interpreted as mixing measurements down to the resolution of the camera. The magnification of the imaging system resulted in a camera pixel imaging 1/150th of an inch in the image plane, which makes the dimensions of each voxel 169 μm per side. However, the camera cannot actually resolve objects down to one pixel. Resolution studies of the camera were performed using a standard resolution target (USAF 1951, which follows MIL-STD-150A), which features black rectangles (aspect ratio = 5) of decreasing width on a white background. Using 50% of the maximum contrast value as the cutoff for resolution, the smallest rectangle the camera could resolve in this optical setup was 315 μm (~2 pixels) wide. The smallest distinguishable rectangles when examining the images by eye were 198 μm wide, and had a contrast ratio of 17%. A rectangle 177 μm (~ 1 pixel) wide yielded a signal contrast of less than 2% compared to large regions of black and white. In general, the sharp edge of a rectangle was blurred across approximately five pixels, with it taking two pixels to reach half of the maximum value. The net result is that the measurement resolution is approximately 1.5 times the pixel size (~250 μm). In order to measure molecular mixing, the flow must be resolved down to 2-6 times the size of the smallest scales.[76,77] Based on the dissipation measured in similar flow fields in a companion effort,[13] the Kolmogorov microscale was approximately 13 μm for the 9 on single jet, 23 μm for the 0 on single jet, 28 μm for the 9 on coaxial jets and 50 μm for the 0 on coaxial jets. Since the Schmidt number is almost one for acetone in air (Sc = 0.933), the Batchelor scales similarly ranged from 14-52 μm. Based on the camera resolution and the factor of 2-6 times the scale size needed for resolution, the mixing in the 0 on coaxial jets (100 - 300 μm) may be resolved in the images. While the mixing scales are not

resolved for the other cases (26 – 168 μm), the imaging system is measuring down to at most 10 times this scale. The fluid in a voxel will mix by diffusion to the average value with a diffusion time scale ($\frac{L^2}{D}$, D = diffusivity) of ~360 μs, so using the velocity profiles shown above the flow will only travel 1-3 mm before the mixing occurs. For the purposes of this investigation, the choice was made to have a larger field of view than to resolve smaller scales. When discussing mixing in this work, it is understood that the measurements are really average values of mixture fraction for a small volume of fluid and not necessarily molecularly mixed fluid.

Most images were acquired with the camera perpendicular to a vertical laser sheet traveling horizontally through the vertically-directed flow field. However, jet cross-section images were also acquired by rotating the laser sheet 90° and moving the camera to 31.8° off vertical to prevent acetone-seeded air from hitting the camera (Figure 3.2). The camera and laser were both triggered by a Stanford Research Systems DG-535 pulse generator, with the delay between the pulses to each piece of equipment adjusted so the camera captured a laser pulse.

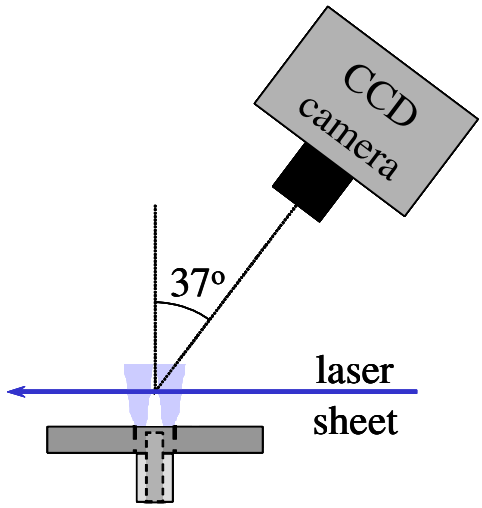

Figure 3.2. A schematic view of the imaging setup for cross-sectional image acquisition.

Gas-Gas Mixing

Flow Generation System

A schematic of the entire flow system is shown in Figure 3.3. The air flow control panel was fed by 120 psig building air that was regulated in two stages down to 5 psig. The air was then split into two separate paths, A and B. Path A went through a rotameter and a valve to control the volumetric flow rate, and then went directly to the flow facility. Path B was split again, with both parts going through individual rotameters and valves to

control the volumetric flow rate through each sub-path. One sub-path (B_1) connected to the acetone bubbler that seeded acetone vapor into the air, which is described in more detail below. The second sub-path (B_2) was recombined with B_1 downstream of the bubbler to allow dilution of the amount of acetone in the flow. This recombined flow then proceeded to the mixing facility. Due to the length of 0.5 inch diameter tubing from the flow control panel to the mixing facility, all the flows were fully developed. Teflon tubing was used for its resistance to acetone.

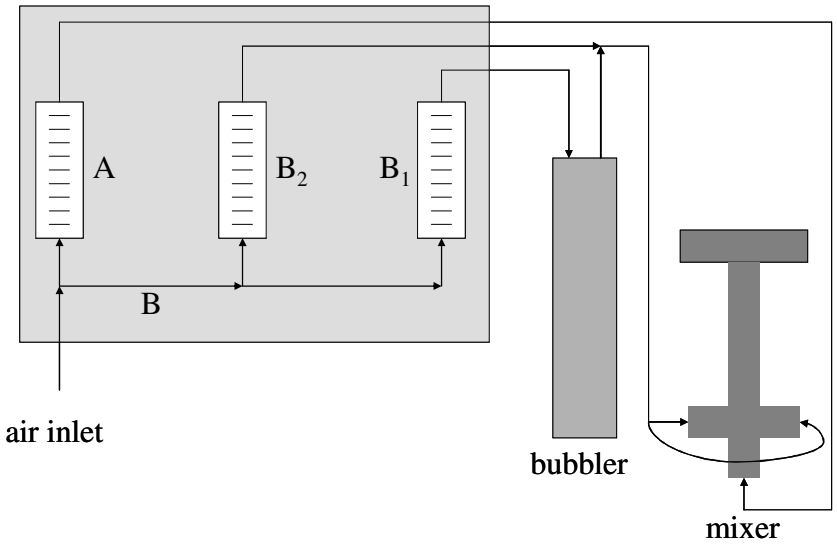

Figure 3.3. A schematic of the flow system used to create the jet flows.

Acetone Seeding System

In order to seed acetone vapor into an air flow, a bubbler system was developed. The bubbler (Figure 3.4) has air forced to the bottom of a container of liquid then lets it bubble up through the liquid before exiting the container. If the container is large

enough to allow sufficient residence time and the air is well distributed throughout the liquid, then the exiting air can become saturated with the vapor of the liquid. The bubbler used in this work was a 35 inch long piece of 3 inch diameter pipe closed at both ends and was designed to handle up to 120 psi safely. The top had a six inch flange welded on, while the bottom had a flat plate with one ¼ inch NPT tapped hole and four short, adjustable legs. For seeding acetone vapor into air, the bottom hole was plugged and only opened to drain the bubbler. A piece of ¼ inch steel bolted on to the top flange with a one inch NPT tapped hole in the center and a ¼ inch NPT tapped hole offset towards the edge. The smaller hole was used for refilling the bubbler and checking the liquid acetone level. A pipe nipple screwed into the larger hole, with a pipe tee upstream of the nipple. A bored-through fitting on top of the tee allowed a concentric, ½ inch outer diameter tube to pass through the pipe nipple to the bottom of the bubbler. The tube ended just above the bottom and had a plate with many holes attached to it to force the air flow to spread out before bubbling up through the liquid acetone. The air came into the bubbler through this inner tube and exited up through the annular region between the inner tube and the pipe nipple and out the side of the tee after being seeded with acetone.

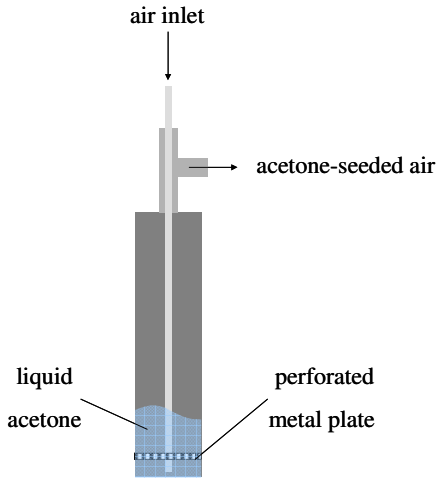

Figure 3.4. A schematic cross-section of the bubbler system used to seed acetone into the air.

The flow rates required for these experiments mandated a couple of precautionary measures to prevent liquid acetone from being blown through the tubing to the flow facility. The first was to have a maximum liquid acetone depth of approximately 12 inches. The other was to use a simple liquid trap on the seeded flow after it left the bubbler. The trap had a horizontal inlet flow into another pipe tee. The seeded air flow went up while a 24 inch long pipe went down to collect any liquid acetone. A valve at the bottom of the pipe was used to drain off any liquid acetone between runs of the bubbler. One reason for working with acetone is its high vapor pressure ($\chi_{acetone} \approx 0.25$) at room temperature (Equation 3.1), allowing for high seeding concentrations. With P_v denoting the vapor pressure of acetone in atmospheres and T being the temperature in Kelvin, the vapor pressure of acetone can be approximated by Equation 3.1.[68]

$$P_v(atm) = \frac{1}{760} e^{\left(16.6513 - \frac{2940.46}{T - 35.93}\right)} \tag{3.1}$$

For convenience, the bubbler was converted to a pressurized vessel of liquid acetone for the spray experiments. A pressure-regulated air line was connected to the top of the bubbler to provide back pressure for the liquid while the acetone-seeded air outlet was blocked with a valve. A 0.25 inch outer diameter copper tube was connected to the drain hole on the bottom of the bubbler and connected to the spray nozzle to provide the liquid acetone.

Jet Flow Facility

The gaseous mixing research was performed with a single, versatile facility. Figure 3.5 shows the main body of the facility used to produce the various jet flows. The two flow paths from the flow control panel both connected to a one inch pipe cross attached to the bottom of a twelve inch long pipe nipple. A 20 inch stainless steel tube with an outside diameter (D_i) of 0.625 inch and a wall thickness (t) of 0.035 inch was inserted concentrically from the bottom of the cross and up through the pipe to create coaxial flows. The flow for the annulus was split in two and input equally on both sides of the cross to create a more radially-symmetric flow field, while the inner jet flow connected to the bottom of the tube. The experimental flow fields were formed by an aluminum body mounted on top of the pipe nipple with a standard pipe coupling and directed vertically.

The flow path through the metal body was 3.00 inches long and was machined to 1.00 inch in diameter (D_o). The inner tube shared the same exit plane as the metal body and created coaxial jets with an area ratio (A_i/A_o) of 0.5. The inner tube was kept coaxial and concentric with two sets of three centering screws that passed through the middle and lower end of the pipe nipple. When only a 1.00 inch (D) round jet was wanted, the inner tube was lowered until its exit was more than twelve inches below the exit of the flow facility.

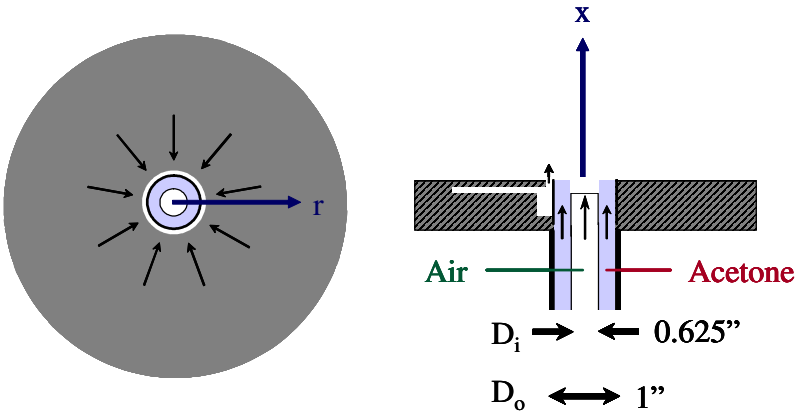

Figure 3.5. A schematic of the mixing facility.

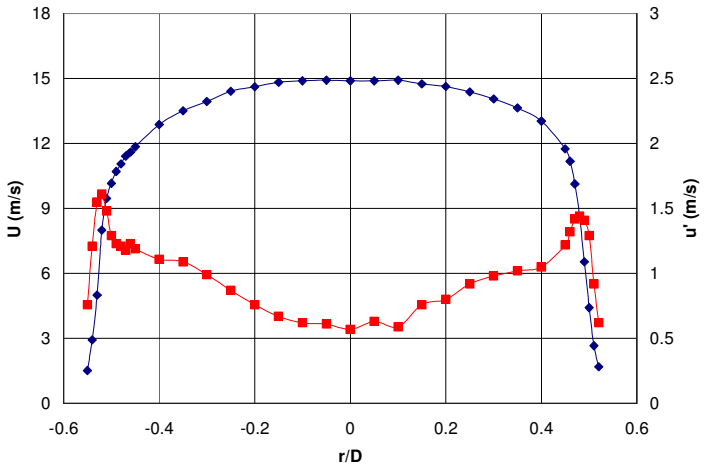

Figure 3.6. U(♦) and u'(■) profiles in the single jet at x/D = 0.25.

For the coaxial jet studies, acetone-seeded air generally flowed through annular jet to measure the mixing both into the quiescent environment and into the inner air jet, although some measurements were made with acetone-seeded air in the inner jet instead. In the single jet studies, the jet was entirely acetone-seeded air. This entire facility was mounted on a vertical traverse that allowed it to be lowered so that measurements could be taken up to 10 inches downstream of the jet exit.

The single jet was operated at a flow rate of 734 scfh of air, the correct volumetric flow rate to provide an average exit plane velocity of 11.4 m/s if no acetone was seeded into the flow. The actual exit plane velocity was as much as 25% greater due to the acetone seeding from the bubbler. Figure 3.6 shows the velocity (U) profile of the single jet as well as the velocity fluctuations (u') profile at x/D = 0.25. The coaxial jets were nominally fed with the correct volumetric flow rate of air to provide an average (overall) exit plane velocity of 10.8 m/s taking into account the amount of acetone seeded into the air in one of the jets. Three different ratios of the central jet velocity (U_i) to the annular jet velocity (U_o) were used: U_i/U_o = 0.30, 0.62 and 1.50. The velocity profiles (U and u') for all three ratios at x/D_o = 0.25 are shown in Figure 3.7. All velocity data presented here were acquired using a hot-film anemometer connected to a computer-controlled traverse.[13]

Table 3. 1. Mean axial velocities for each jet as well as the associated Reynolds number based on diameter or hydraulic diameter.

Flow	$U_{i,ave}$ (m/s)	$U_{o,ave}$ (m/s)	$U_{SJ\ max}$ (m/s)	Re_D	Re_{DH}
Single jet	14		11	24,000	
U_i/U_o = 0.30	14	4.1	10		7600
U_i/U_o = 0.62	13	7.4	10		7600
U_i/U_o = 1.4	10	15	10		7600

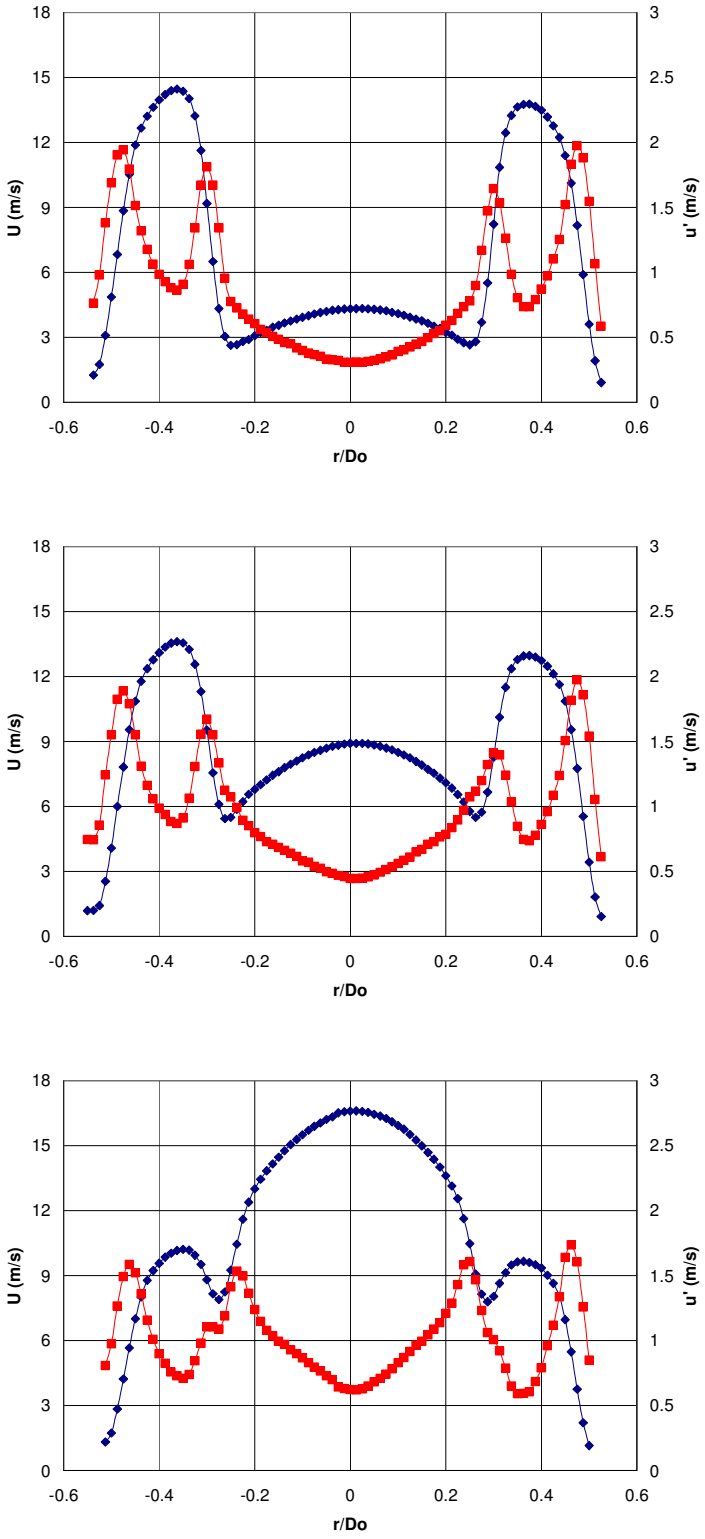

Figure 3.7. U(♦) and u'(■) profiles in the co-axial jets at x/D = 0.25 for U_i/U_o = 0.30 (top), 0.62 (middle) and 1.4 (bottom).

Jet Actuation

The metal body mentioned previously, and shown in Figure 3.5, housed nine synthetic jet actuators equally spaced around the circumference of the coaxial jets. The metal body actually consisted of five parts (Figure 3.8). The 0.125 inch thick cover plate and 0.050 inch wall thickness inner sleeve came in matched pairs that directed the actuator jets either axially (parallel to the main flow) or radially (perpendicular to the main flow). This was accomplished by adjusting the inner diameter of the cover plate and the height of the inner sleeve. The axial jets use a cover plate with an inner diameter of 1.14 inches and a sleeve height of 0.75 inch, leaving an opening at the inside of the cover plate and the full height sleeve turns the flow to be parallel to the main flow. Each axial jet orifice was an arc 0.5 mm in width (h) and 9 mm in length (l). Radial jets were formed by a cover plate with a 1.00 inch inner diameter and a sleeve only 0.72 inch in height, creating a gap above the top of the sleeve which lets the jets travel directly into the flow. Each radial jet orifice was an arc 0.76 mm in height (h) and 9 mm in length (l). The actuators were located near the jet exit to enhance mixing of the central flows and the surrounding air.

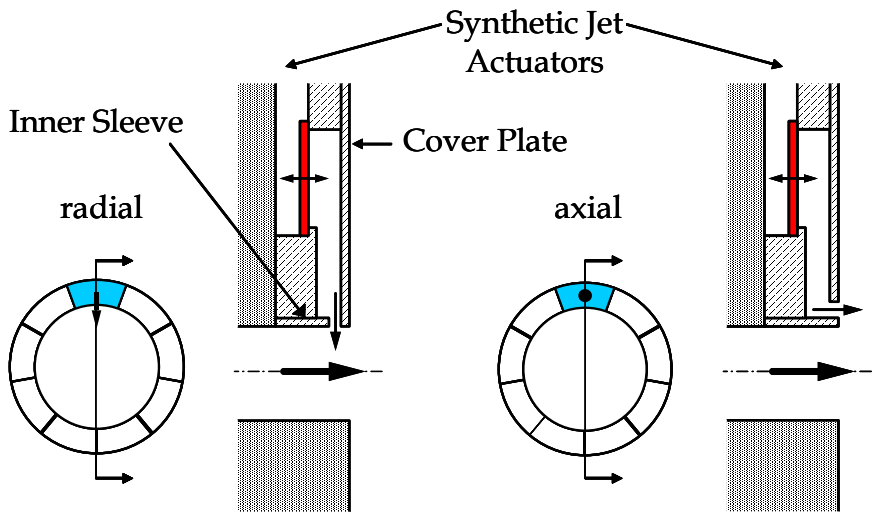

Figure 3.8. Schematic cross-section of the actuator housing body in both radial and axial configurations.

The actuators used piezoelectric membranes in plastic bodies and were driven at the resonant frequency of the membrane (1.18 kHz) by a common signal source. However, each actuator was driven by a dedicated amplifier set so that every actuator provides a 10 m/s synthetic jet at x/h = 12.5 (x/D_o = 0.25) in the axial orientation. A computer-generated, low frequency (10-60 Hz) amplitude modulation (a tapered square wave with an effective duty cycle of 60%) was imposed on the high frequency signal in some cases (Figure 3.9). This provided a Strouhal number range of 0.022-0.134, well below the preferred value for the flows of interest (0.24-0.51), assuring the effects were not due to amplification of inherent instabilities.[13] The actuation system and frequencies were chosen to match those used in a companion effort.[13] Evaluating a range of frequencies showed that the low frequency needed to be at least a factor of 10 lower than the high frequency in order for the individual pulses of the actuators to coalesce into a synthetic jet.[13]

For the cases with amplitude modulation applied to the jet actuators, the trigger of the laser/camera system was phase-locked to the modulation signal. An output signal from the computer was used to trigger the pulse generator that triggered the PLIF system. Equally-spaced, phase-specific measurements were taken by varying the delay between the input to the pulse generator and its output. The phase delay between the start of an amplitude modulation cycle and the first phase acquired was 30.125 ms.

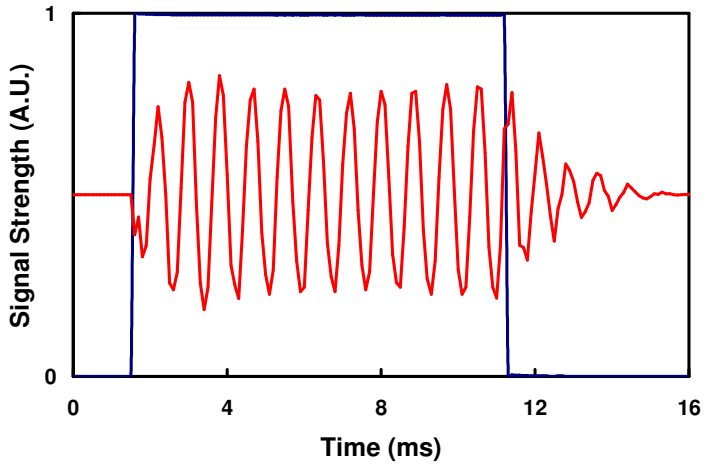

Figure 3.9. The duty cycle (blue) and synthetic jet strength (red) during low frequency amplitude modulation signal in the single jet.

Because each actuator can be controlled individually, several different patterns of actuation were studied (Figure 3.10). The base case of no actuation is referred to as "0 on." "9 on" is the case of all 9 actuators running at the high frequency. The "6 on" case used 6 contiguous actuators running at the high frequency with the other three actuators turned off. The final geometric pattern used was the "2 on, 1 off" case in which 2 adjacent actuators were running at high frequency with the next actuator being off, and the pattern repeated to provide three-fold symmetry. When synchronous amplitude

modulation was added, the "9 on" case became "9 pulsing" in which all 9 actuators went through the duty cycle together. Phase-shifted amplitude modulation was applied to the "6 on" case to yield the "6 spinning" case in which the six on pattern spun clockwise when viewed from above (1-6 were on, then 2-7, etc.).

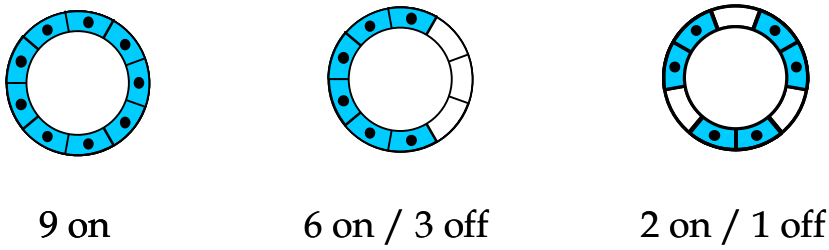

Figure 3.10. Diagrams of the three actuation patterns used in this investigation.

The other experimental consideration was that the nine actuators provided asymmetric flow. All planar measurements acquired from a side view of the flow were taken on a plane that passed directly between two actuators before reaching the jet exit and passed directly over the middle of an actuator after crossing through the center of the jet. The actuators were controlled such that the laser sheet bisected the static actuation patterns into two mirror images of each other, splitting between the active actuators and directly over an inactive one for the 6 on and 2 on, 1 off cases. This asymmetry between the left and right sides helped examine the physics behind synthetic jet mixing enhancement.

Liquid Facilities

Spray Facility

For spray measurements, a Hago M5 fine atomizing water spray nozzle, with an outer diameter of 7/16 inch and 2½ inch in length, was attached to a coaxial, concentric tube 3/8 inch in diameter inserted inside the inner tube in the mixing facility (Figure 3.11). This allowed for a narrow annular air co-flow around the nozzle in addition to the same annular air flow used in gaseous experiments. The acetone bubbler was modified by attaching a ¼ inch copper tube to the drain hole to act as a pressurized liquid tank. The liquid acetone was provided from the converted bubbler with 40 psi of back pressure. Under these conditions, the M5 nozzle would have provided a 40° half-angle solid cone spray with a 3.16 gph flow rate and 45.2 μm Sauter mean diameter (SMD) *for water* according to the manufacturer.

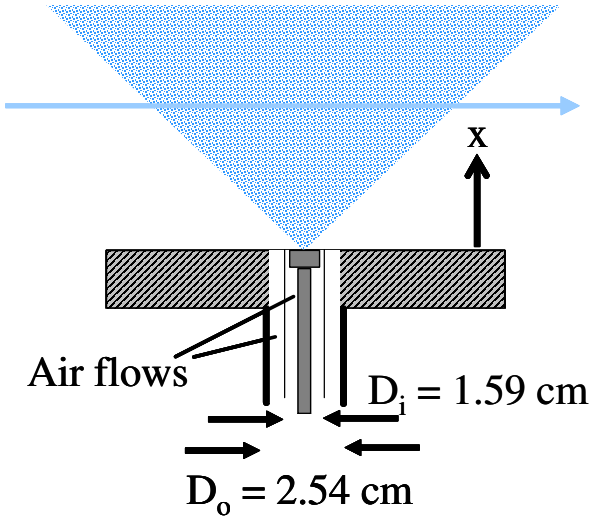

Figure 3.11. Schematic cross-section of the spray facility using the water nozzle.

In anticipation of taking spray measurements, an approximation of the expected SMD was calculated following the derivation by LeFebvre.[78] The appropriate equation is

$$SMD = 2.25\left(\frac{\sigma\mu\dot{m}}{\rho_{air}}\right)^{0.25}\Delta p^{-0.5} \tag{3.2}$$

Using the physical properties of acetone, this converted to an approximate expected SMD of 22.3 μm for acetone. This value was checked by measuring the SMD with a phase Doppler particle anemometer (PDPA), measured at 1 mm intervals along a line perpendicular to the spray one inch downstream of the nozzle exit and passing through the centerline of the spray. The average SMD along this line was 84 μm (Figure 3.12), much bigger than the calculated value. The result was checked by rotating the spray 90° and acquiring more data, and the values were virtually identical. A noticeable difference between the left and right sides of the spray is shown in the SMD profiles, but this is

believed to be a systematic error based on the similarity of the results after rotating the spray.

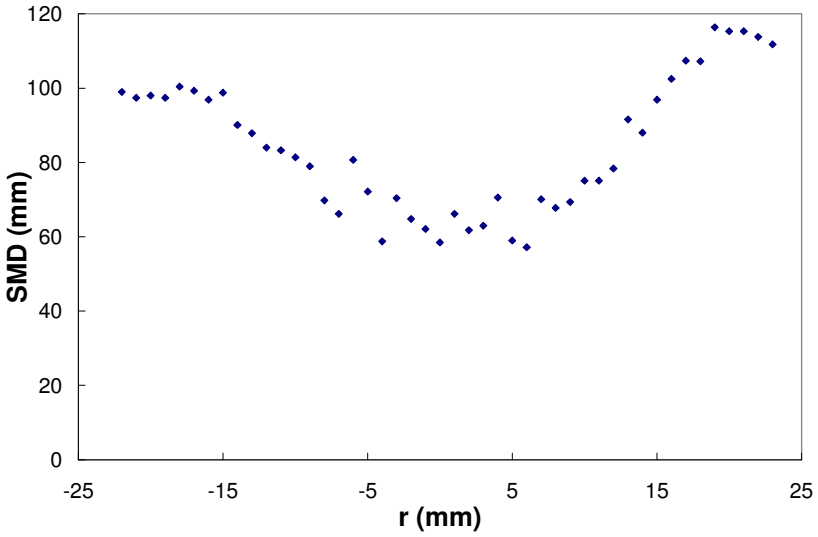

Figure 3.12. SMD distribution one inch downstream of nozzle.

Some additional liquid acetone spray research was performed using a Nanomiser® Device from MicroCoating Technologies, Inc. The experimental flow field was formed by one central hole emitting acetone and four surrounding holes providing air (Figure 3.13). The Nanomiser® system consisted of a small liquid pump that provided precise flows of low volumetric flow rates, a small air control panel and a spray body. Both the liquid acetone and the air passed through the spray body, and the spray body was electrically heated to a controlled temperature. The temperature, the liquid flow rate and the air flow rate were all adjustable. The proposed advantages of the Nanomiser® were that it used less acetone and provided very small droplet sizes (<10 μm for water). Further details of the Nanomiser® system are omitted as they are proprietary.

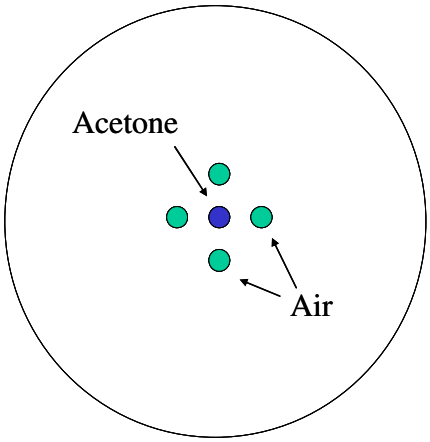

Figure 3.13. A rough schematic of the exit of the Nanomiser® Device.

Quantitative Gaseous PLIF

Fundamental Equations

As with any optical experiments, there were several issues that had to be considered when examining the acquired images for quantitative information. As seen in Equation 3.3, the signal from the camera, S(x,t,r), is a combination of light from various sources and varies with downstream location (x), radial position (r) and time (t). There is ambient background light from the room, $B_{room}(x,t,r)$, background light generated by the laser pulse, $B_{laser}(x,t,r)$, and the fluorescence signal from the acetone, F(x,t,r).

$$S(x,r,t) = B_{room}(x,r,t) + B_{laser}(x,r,t) + F(x,r,t) \tag{3.3}$$

The ambient background light and the laser-generated background light can be combined into a total background signal, B(x,r,t), allowing S(x,r,t) to be redefined using Equation 3.3a.

$$S(x,r,t) = B(x,r,t) + F(x,r,t) \tag{3.3a}$$

Subtracting the background signal from the total signal gives the fluorescence signal, as shown in equation 3.4.

$$F(x,r,t) = S(x,r,t) - B_{average}(x,r,t) \tag{3.4}$$

Equation 3.5 shows the details of the fluorescence signal. C is a constant based on the efficiency of the generation and collection of the fluorescence. E_0 is the nominal initial laser energy. E'(x) is the correction factor for the relative strength of the laser sheet at distance x downstream from the jet exit. E'(t) is the correction factor for the relative strength of the given laser shot based on the shot-to-shot fluctuation in the laser energy. E'(r) is the correction factor for the relative strength of the laser sheet due to losses from laser absorption by acetone at the given radial location in the flow. These four factors combine to produce the correct local incoming energy for the voxel, (volume being imaged onto the pixel in question). The local mole fraction of acetone, $\chi(x,r,t)$, is the final factor in determining the fluorescence signal and is the desired result from the measurements. It is easily solved for using Equation 3.5.

$$F(x,r,t) = CE_0 E'(x)E'(t)E'(r)\chi(x,r,t) \tag{3.5}$$

Correction Data

As just described, several pieces of data are needed to convert raw images into quantitative measurements of acetone concentration. Two sets of background images were acquired to help make this possible. One set was acquired with no acetone present and no laser running, while the other set had no acetone but the laser was running. The first set provided a measure of the light generated by other sources in the room, such as computer monitors, while the second set provided a measure of the visible light generated by the laser as well as the room. Luminescence caused by the laser sheet striking objects created some of the visible light, and some was emitted from the laser along with the UV laser beam. In practice, an average background image acquired with the laser running, $B_{average}(x,r,t)$, is subtracted from each of the acquired images (Equation 3.4) to reduce noise due to shot-to-shot fluctuations.

The variation in energy from one laser shot to the next (Figure 3.14) was specified as less than ±10% for the laser. The actual value was obtained from the images of the secondary laser sheet striking the optical post (Figure 3.1) minus the background with no laser running, and was in that range. An optical post was used so that slight movement of the laser beam would be noticeable due to the radius of curvature. Since the post was not in the focal plane, the signal was already blurred on the CCD. The data was binned so that four pixels were averaged into one (2 × 2 binning) to further reduce noise in the signal.

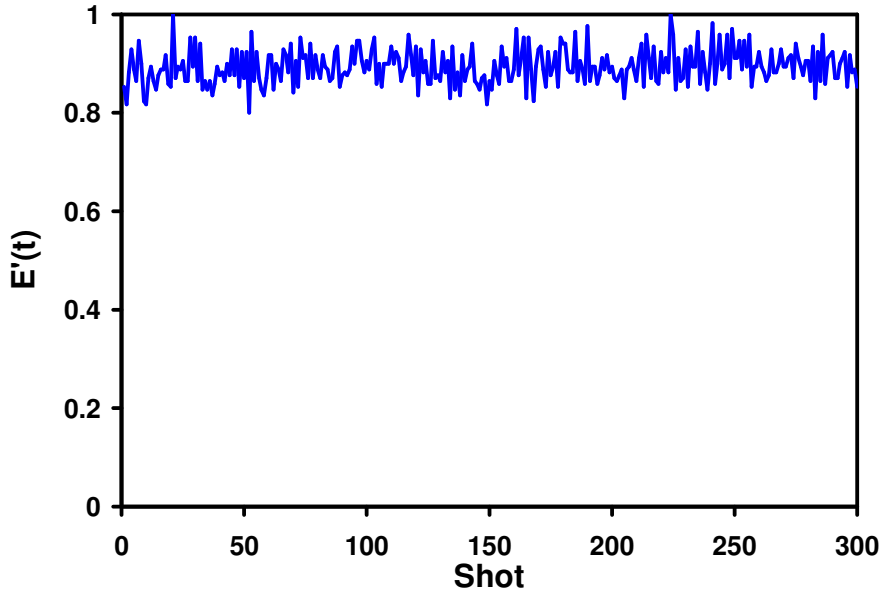

Figure 3.14. A typical sample of the normalized laser energy for 300 laser shots.

In order to measure the variation in laser energy across the height of the sheet, a very slow center jet with a low concentration of seeded acetone (to minimize absorption) was created. Due to the narrow width of the jet, the traverse was used to raise the mixing body upwards so that the sheet was always imaged in the potential core of the jet, where the concentration should be constant. This was done in three separate parts (low = first 1.25", middle = next 1", high = remaining 0.75") with overlap of the regions to keep the profile continuous. An average of 50 images was acquired and the intensity profile along the laser height was smoothed with a 5 point moving average. The profile was then normalized by the peak signal to provide the relative strength of the laser sheet at any height in the sheet. The profile data was acquired at the beginning and end of every data

acquisition session. An example of the laser sheet energy distribution is shown in Figure 3.15.

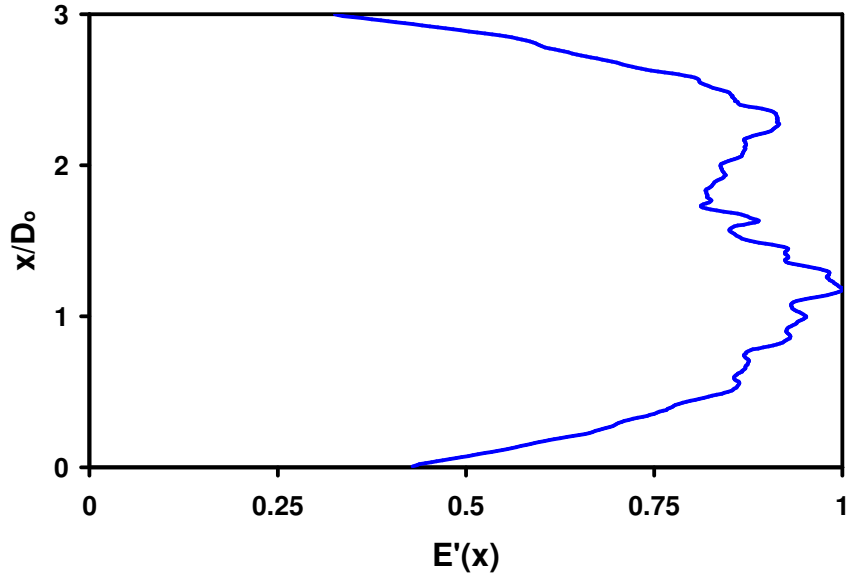

Figure 3.15. Sample laser sheet profile.

The technique was calibrated against a known acetone concentration in order to calculate the constant used to relate a given signal to an actual amount of acetone. This was done by creating another very slow center jet, this time with high acetone concentration. The constant was calculated from the exponential signal decay across a region of uniform concentration, averaged over 50 rows in height and 20 images, using the known absorption cross-section for acetone vapor. The effect of absorption can be modeled by Beer's Law[25] as shown in Equation 3.6.

$$I(r) = I_0 e^{-\alpha L} \tag{3.6}$$

I(r) is the laser intensity, I_0 is the original laser intensity at x = 0, α is the absorption coefficient of the medium and L is the length traveled through the medium. Using this equation, α is calculated from the signal decay. The coefficient is reduced to concentration by dividing α by acetone's absorption cross-section per molecule, yielding the number density of acetone molecules.

There was a downside to the high vapor pressure of acetone in this work. Coupled with the air flow rates for the jets, it consumed large amounts of acetone. The acetone seeding level decreased due to a combination of evaporative cooling in the bubbler, which reduces the acetone temperature and vapor pressure, and a decrease in the bubble residence time as the liquid level dropped. As seen in Figure 3.16, there was a gradual drop in the acetone seeding level during a given experiment. This value was tracked by imaging the small acetone jet (Figure 3.1) during data acquisition. The change in seeding lowered the molecular weight of the jet fluid over time (as mentioned previously). This effect was reduced by placing the bubbler in a heated water bath (25° C) to maintain a more constant temperature and by running the bubbler for short periods of time (less than 15 minutes) between refills. Although acetone fluorescence is temperature dependent,[41] the small temperature changes involved here (< 20°F) have a negligible effect on the photophysical properties of acetone. The seeding level of acetone ($\chi_{acetone}$ = 0.15-0.25) also created small changes in the gas density and diffusion that have minor effects on the flow in the near field.

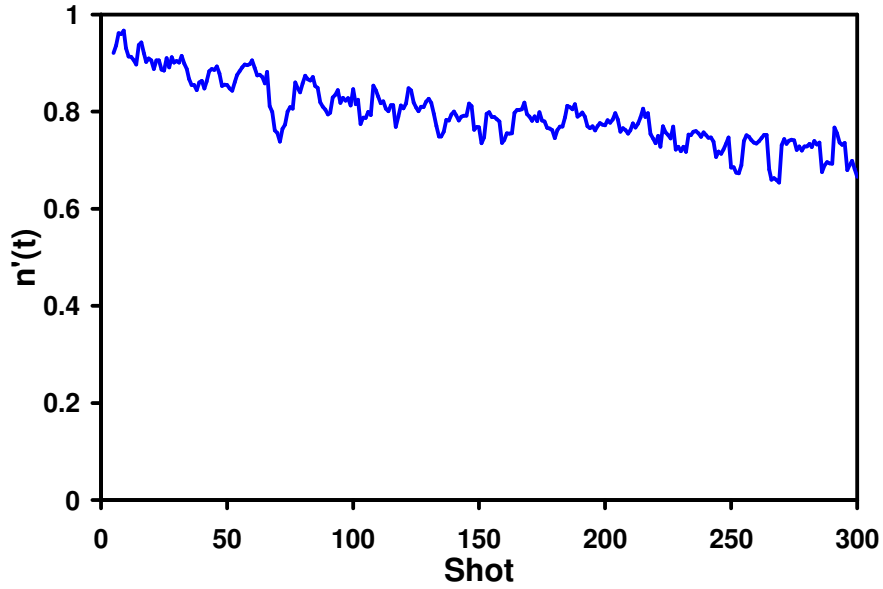

Figure 3.16. A typical record of the normalized acetone concentration in the air during a data acquisition run.

Laser Absorption

It is important to correct for absorption of laser energy across an image given that acetone is such a strong absorber. This was accomplished by correcting an image one column at a time and marching across the image in the direction of the laser sheet. Since the flow field is a non-uniform medium, the integral version of Equation 3.6 (Equation 3.7) is needed.

$$I(r) = I_0 e^{-\sigma \int n(r) dr} \tag{3.7}$$

In this equation, σ is the absorption cross-section per molecule of absorbing species and n(r) is the local number density of the absorbing species. Because the PLIF experiment has finite step sizes, based on the camera pixel size, in practice the integral becomes a summation as shown below in Equation 3.8, where Δ is the length of a voxel.

$$I(r) = I_0 e^{-\sigma\Delta\sum n(r_i)} \tag{3.8}$$

This summation will correct for the absorption from all the pixels before the current pixel. However, the current pixel also creates absorption, so the calculation needs to be iterated to adjust for the absorber in the voxel of interest as well. This was done by assuming that on average the laser sheet had passed through half the voxel before hitting the absorbing molecule, so the pixel was corrected for half of the acetone absorption indicated by the signal from the pixel.

Data Correction

Having described the corrections applied to the images, a step-by-step description of the correction procedure is in order. Before correcting images of the flow field, several steps were taken. First, the average background images were created from the acquired background images. Next, a laser sheet profile was created from the images of the low

concentration center jet. Finally, the constant that relates signal intensity to acetone concentration is calculated. Having these values, correction of the data images began.

Image correction started by subtracting off the average background signal. The shot-to-shot energy fluctuation of the laser power was calculated for each frame in the image set after background subtraction. The laser sheet profile correction was then applied to all the images in the set. Using the constant and the energy fluctuation data just calculated, each frame was then corrected for laser absorption by marching the exponential correction across the image, yielding a corrected image of the local mole fraction. Because the final results will be presented in mixture fraction, the images are converted using Equation 2.2.

Figure 3.17 presents a "before and after" example of the background and absorption corrections for a single data row from a corrected single jet image. The raw data is S(x,r,t) from Equation 3.1, so it starts above 0 due to the background light. Subtracting the background light yields the fluorescence signal (Equation 3.4). Applying the correction factors in Equation 3.3, the corrected signal begins and ends at 0 with a region of uniform, pure fluid in the center. Only the absorption correction is apparent in the figure since it is one row (no E(x)' effect) taken at one time (no E(t)' effect). The signals are normalized by the peak of the signal of each profile in the figure, so both maximize at 1. This normalization makes it easier to compare the result to the original signal for demonstrative purposes, but is not a normal part of the correction routine. The line indicates Beer's Law for the absorption from pure fluid.

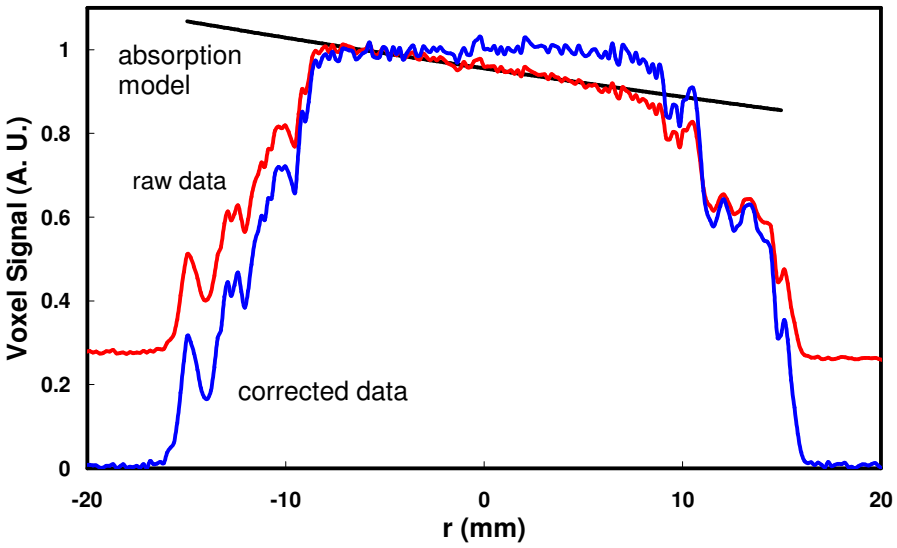

Figure 3.17. Example of laser absorption correction applied to one row of instantaneous acetone PLIF data (laser enters from the left side of the row).

More instructive, perhaps, is to show an image of the unforced coaxial jets at each stage of the correction procedure (Figure 3.18). All four images use the same colorbar, but over a different range of values. The maximum is always dark red and the zero value is dark blue. The original image begins in the brighter blue due to the background signal, as seen in comparison to the second image. The shot-to-shot variation in laser energy does not change the appearance of a single image, so the third image is after both the fluctuation correction and the laser sheet energy profile correction. The vertical distribution of values is much more appropriate at this stage, but the left to right differences are quite significant. Applying the absorption correction yields a corrected image of the local mole fraction that is well balanced from left to right and has a smooth vertical distribution.

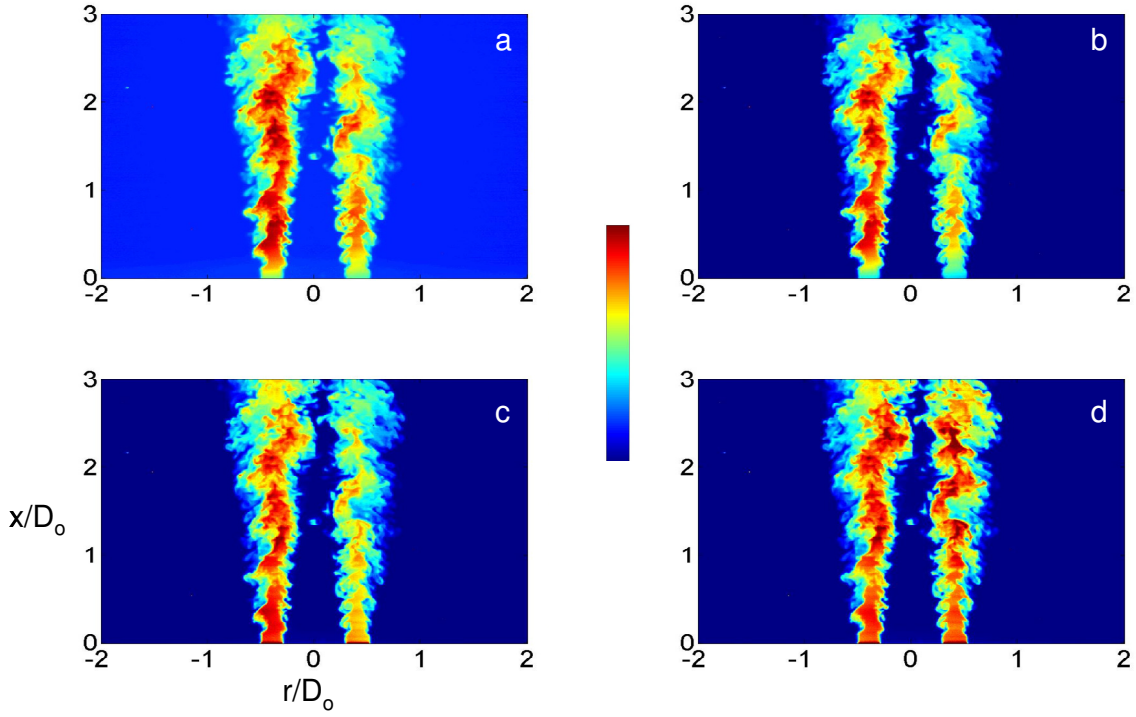

Figure 3.18. An image at four stages of the correction procedure: (a) the original image, (b) after background subtraction, (c) after laser energy fluctuation and sheet profile corrections, and (d) after absorption correction.

The final step in the procedure is to convert the data from mole fraction to mixture fraction, using Equation 2.2 as discussed in Chapter 2. Figure 3.19 uses the final image just shown, before and after conversion into mixture fraction. Both images use the same colorbar, with the mole fraction being lower by a factor of ~ 5.

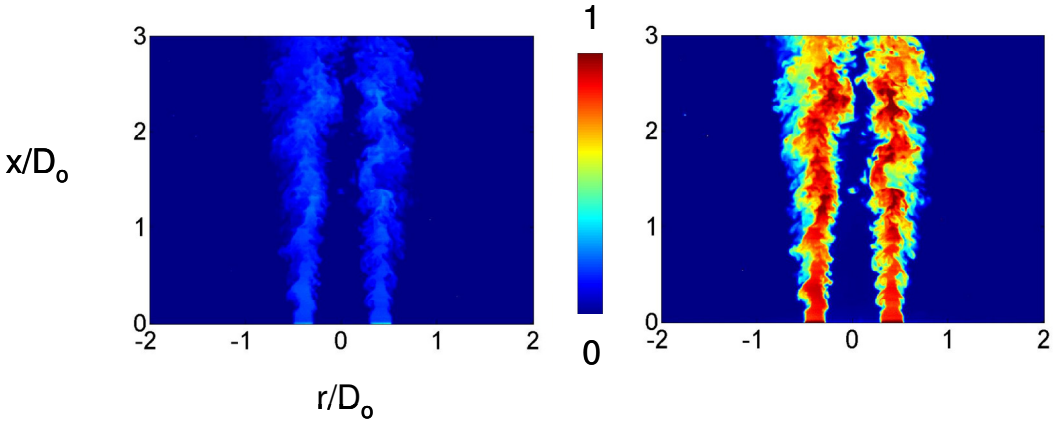

Figure 3.19. A comparison of an image in terms of mole fraction (left) and mixture fraction(right).

This series of corrections is unique to this investigation. Multiple studies have corrected for the laser energy effects in the same way, but none has coupled that with the marching absorption correction because it is computationally expensive. Instead, they have either approximated the result by normalizing with another image, designed the experiment to minimize absorption (narrow flows, low seeding levels), or ignored the absorption. The few that have used the marching absorption correction have not done all of the other laser energy corrections.

The qualitative images presented in Chapter 4 did not receive this full correction treatment. They received a laser sheet correction without using a moving average to smooth the curve. The side views also received an approximated absorption correction. The full correction was not possible since the small jet and scattering post were not present for these images. The images provided the desired information quickly for a variety of cases without the additional time and disk storage space the full correction procedure required. One consequence is that the unsmoothed laser energy profile

produced small striations (± 0.02) in the images (Figure 3.20). Due to the location of the change from red to yellow in the colorbar, these striations are very obvious to the eye. Another possible cause for these striations is index of refraction variations in the shear layer, but that is considered less likely since the smoothed sheet profile correction eliminated these striations. In addition, the striations were spatially stationary within a data acquisition session, indicating that the striations are in the sheet correction and not the data itself.

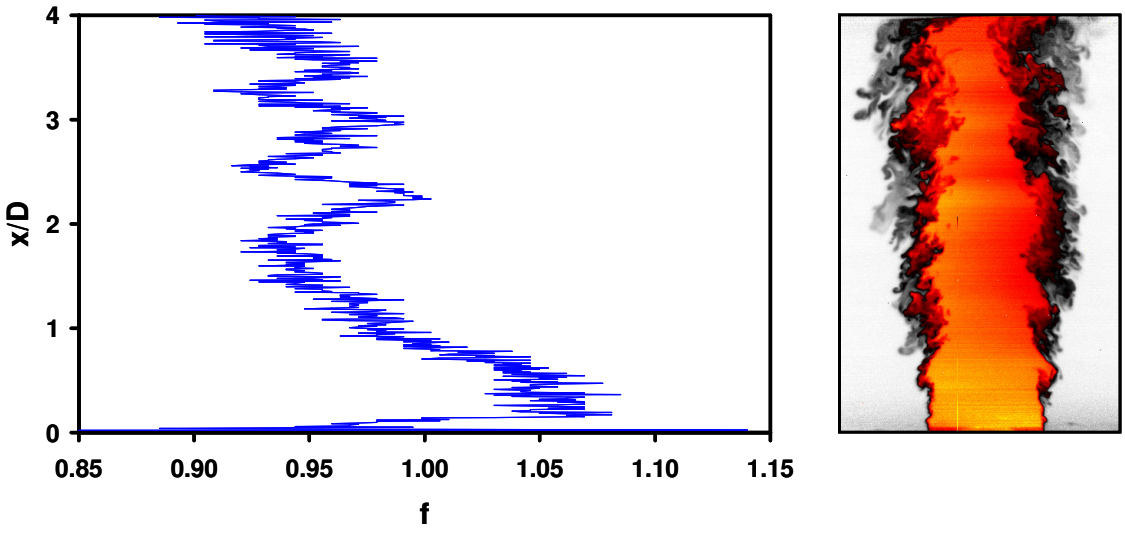

Figure 3.20. The central column of pixels in a qualitative single jet image with the image shown in comparison.

Error Estimation

There are multiple sources of error in the final quantitative results. The camera signal to noise ratio is approximately 200 for saturated acetone seeding, so the noise floor is f =

0.005. Based on all of the images acquired, the background correction error has a standard deviation of 0.016. The final error cannot be negative because the correction scheme forces negative values to zero, so the error is biased positive in the final results. The laser energy fluctuations have a standard deviation of 5.3%, so the error in the correction itself is ~ 0.4%. Estimating the error in the calculated sheet profiles is harder, since the best data to compare against is the data from which they were calculated. Based on other data, the correction has an error magnitude of ~ 3%. The calculated constant is accurate to ~ 2.3%. The absorption correction is the most susceptible to error since it is an exponential correction marched across hundreds of pixels. Based on an assumption of symmetry in various unforced flows, the correction has a standard deviation in an image of 3.8% of the local value. Error propagation calculations result in an approximate standard deviation of 5.6% in the local mixture fraction for the right side of the images. Computing a value based on the data gives a better result of 4.6% of the local value. The relative error is larger for very low mixture fractions as the signal approaches the noise level and possible background error, limiting the measurement to a minimum of $f \approx 0.03$. The system can measure as low as $f \approx 0.005$ but the potential background error is significantly larger, making the measurement inaccurate.

Another check performed on the data was to calculate the flow rate of acetone at a series of downstream locations (Figure 3.21). This value, the integral of the product of acetone level and axial velocity, should remain constant if acetone and velocity are not being lost by the imaging system or stored at some location. Velocity profiles were acquired in the mixing facility at three downstream locations for both the unforced and the 9 on actuated cases. The coaxial jets were measured in two locations for the

unforced, 9 on and 9 pulsing cases as well (x/D_o = 0.25, 1). In order to extend the measurement, two more velocity profiles (x/D_o = 2, 3) were taken from measurements in a companion effort using a very similar flow field.[13] The results are nearly flat for the single jet case and the near field of the coaxial jets where the velocity profiles were acquired in the mixing facility. The worst errors occur downstream in the coaxial jets where the velocity profiles were not taken in the same facility as the mixing measurements. The higher turbulence in the annulus of the mixing layer spread the acetone broader than the velocity profiles from the other facility, so the integrals are less accurate as they probably give higher velocities to the acetone closer to the center than is correct. The outermost acetone is underweighted due to this profile effect but represents a smaller portion of the acetone, resulting in an increased integral value above the correct value.

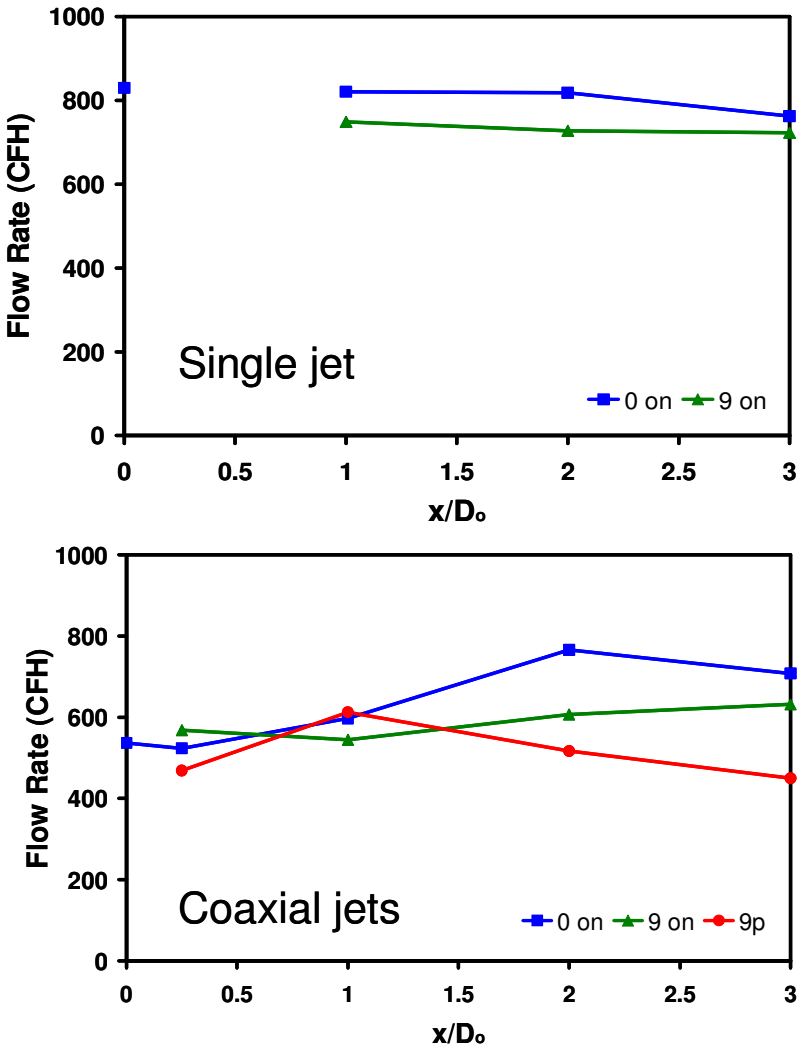

Figure 3.21. Integrated acetone flow rate in the single and coaxial jets.

CHAPTER 4

QUALITATIVE MIXING MEASUREMENTS

This chapter describes a preliminary experimental study of the actuators. The intent was to characterize their effects and to determine which actuation cases deserved to be studied in greater depth. Three different spatial patterns of actuation were tested, as described previously (all nine actuators on, six contiguous actuators on with the other three off, and a repeated pattern of two on and one off). Both axial and radial directions of actuation were tested as well. In addition, many of these combinations were tested with amplitude modulation, with several modulation frequencies evaluated for two cases. These experiments were conducted with a single jet as well as with coaxial jets. Side view images for this diverse set of cases were acquired along the jet axis, with cross-sectional images taken at several downstream locations.

Fundamental Actuation Effects

Results for the axisymmetric, single jet provide a demonstration of the basic effects synthetic jet actuation has on a jet flow. Full side-view images of the acetone distribution were obtained with a vertical laser sheet passing through the center of the flow. The camera viewed the acetone PLIF normal to the laser sheet as described in Chapter Three. Figure 4.1 compares single-shot, side view images of the single jet for two cases: no

actuation and the nine-on pattern. The unforced case (on the left) exhibits a lower jet spreading rate and a thinner mixing layer. The high frequency pulsing when the nine actuators are on (right image) produces an enhancement of the jet growth and a broadening of the mixing layer. The regularly spaced structures visible on the edge of the actuated jet correspond to the vortices produced by individual pulses of the synthetic jets, as the spacing of the structures matches the value one would predict using the actuation frequency (~ 1.2 kHz) and convective speed in the mixing layer (~ 8 m/s). As discussed in Chapter 3, the horizontal striations in the images are due to an approximate laser energy distribution correction, but they do not impact the qualitative results.

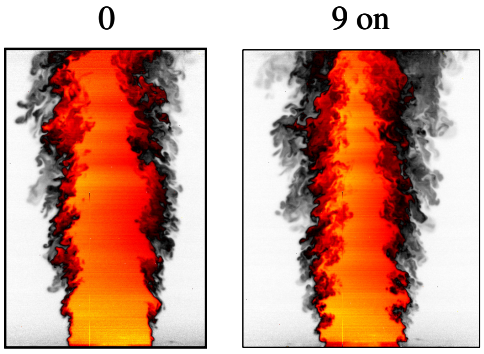

Figure 4.1. Side view images of the jet for the unforced (left) and 9-on (right) actuation cases. The jet exit is 1″ in diameter, and the images show x/D from 0 to 4.

Effects similar to those seen in the single jet cases can be seen in coaxial jets as well. The results shown in Figure 4.2 reveal the increase in jet spreading with all nine actuators running. The actuation significantly increases entrainment, compared to the unforced jet. This is seen in the lower peak acetone concentrations downstream, and the increased spreading of the jet.

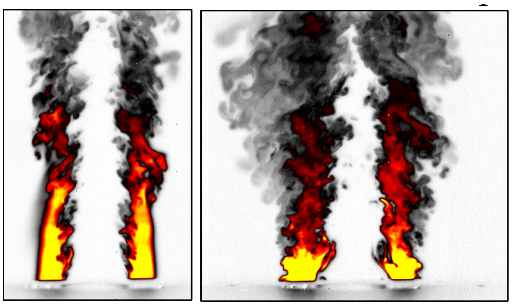

Figure 4.2. Side view images of coaxial jets for the unforced (left) and 9-on (right) actuation cases. The jet exit is 1″ in diameter, and the images show x/D_o from 0 to 3.

Spatial Control

In addition to changing mixing rates, the actuators have the capability to move where the jet fluid goes. This ability of the synthetic jets to alter the spatial distribution of the jet fluid is first illustrated in Figure 4.3, which compares instantaneous radial cross-sections (top views) taken at x/D = 3 in the single jet. These images compare the unforced jet with cases where the actuation is radial (synthetic jets pointed toward the jet axis) or axial (parallel to the jet axis). The strong pull of the axially oriented synthetic jets caused by momentum transfer draws the acetone towards the active actuators. The resulting triangular shape in the two-on/one-off case has vertices between each pair of active actuators and the flat sides are above the inactive synthetic jets. A comparison of the two-on/one-off case shows that radial actuation is less effective in creating outward motion of the jet fluid, as evidenced by the lack of the triangular points seen in the axial

case. Still, the jet is spread more widely than in the unforced case so the actuators are increasing the mixing.

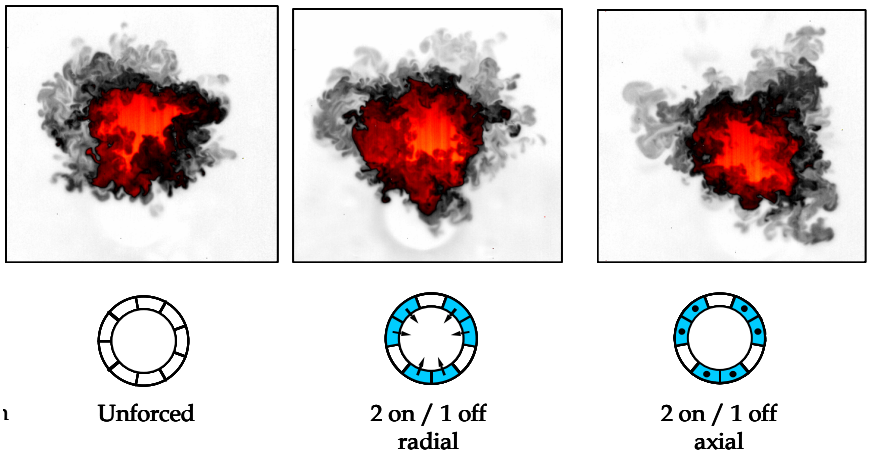

Figure 4.3. Cross-sectional views of the single jet at x/D = 3 for three actuation cases (L to R): unforced, 2-on/1-off radial, and 2-on/1-off axial.

The six-on actuation case works the same way, but the asymmetry of the pattern moves the jet off-center, i.e., vectoring the jet fluid, instead of just warping the jet shape from the original circle. Figure 4.4 shows the effects of asymmetric actuation at x/D_o = 0.5, with 6 actuators on and 3 off in the coaxial jet case. The active actuators are centered at the bottom of the image. The suction produced by the actuators pulls most of the acetone in the annular jet away from the non-actuated region. Additionally, the acetone concentration is lowered by mixing with the surrounding air. All of this can occur before fluid reaches the jet exit, as shown in Figure 4.5. Interestingly, the jet spreading is increased by actuation *even on the side without active actuators*.

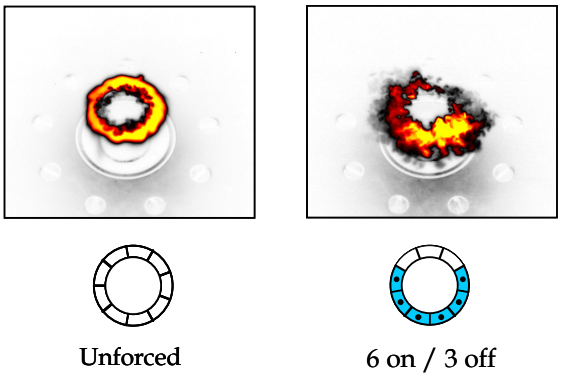

Figure 4.4. Cross-sectional views at $x/D_o = 0.5$ of the coaxial jets for unforced and 6-on/3-off actuation. The 6 active actuators are centered on the bottom of the image.

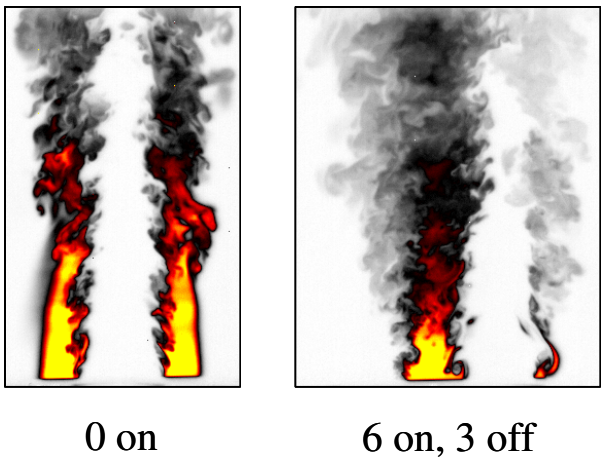

Figure 4.5. Side views of $x/D_o = 0$-3 for unforced and 6-on/3-off actuation. The 6 active actuators are centered on the left side of the image.

Amplitude Modulation Effects

While the synthetic jet cases shown above exhibit significant and potentially useful changes to the jet flow fields, all of the effects are driven by small scale structures created by the high frequency actuation. The creation of larger scale structures is also of interest. Such structures can be produced by applying amplitude modulation to the high frequency signal driving the actuators, e.g., imposing a low frequency (10-60 Hz) component in addition to the high frequency signal. Amplitude modulation was tested in two different forms. In the first mode, all nine actuators modulated in phase to generate a low frequency pulsing effect of the synthetic jets. The second mode modulated the actuators 40° out of phase, resulting in six contiguous actuators running at any given time with the pattern spinning around the perimeter of the coaxial jets.

9 Pulsing

Figure 4.6 compares results for a basic actuated case (9 on) with the results for amplitude modulation of the single jet. The case shown on the right has a 40 Hz amplitude modulation imposed on the 1.2 kHz synthetic jet driver signal. This low frequency modulation produces large scale structures as can be seen in this image as the significant pinching of the jet. The pinching precedes the actuators turning back on, which is indicated by the small structures starting to appear just above the exit again. It is the reactivation of the synthetic jets that leads to the large structure that pushes the jet fluid out wider as it propagates downstream (not shown here). Only one structure can be

found within these images from x/D = 0-4, since each structure moves out of field before the next one is produced due to the convective velocity of the structure and the frequency of the pulsing. Greater jet spreading is evident in the modulated case than the actuated case during some phases, indicating the potential for enhanced mixing with amplitude modulation.

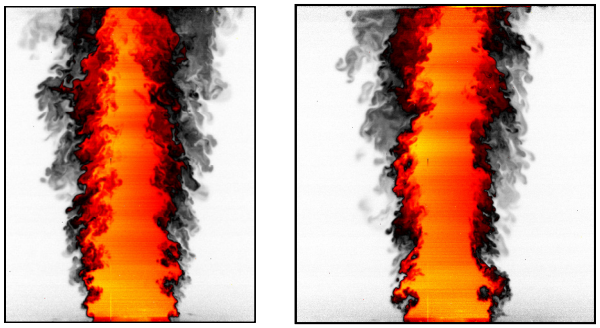

Figure 4.6. Side views of the single jet showing x/D = 0-4 for both 9-on and one phase of 40 Hz amplitude modulated 9-on (9-pulsing).

Figure 4.7 presents a similar comparison for the coaxial jet case. Pulsing the nine actuators again enhances the mixing rate even more than standard actuation. The acetone concentrations are reduced by a factor of two as quickly as x/D_o = ½. The phase-locked image of the pulsed case was obtained for a modulation frequency of 50 Hz. This frequency and the phase shown correspond to the maximum increase in mixing. For the least favorable phase and frequency studied, there was still a slight increase in jet spreading compared to the non-actuated case.

The periodic effect of pulsing actuation on the coaxial jets is illustrated in Figure 4.8. The images, at four equally spaced phases with respect to the pulsing frequency, show a cycle of expansion and contraction of the annulus at x/D_o = ½, with 50 Hz pulsing. Even

in the phase of minimum jet spreading, the maximum acetone concentration is lower than in the non-actuated case. The two phases with medium jet spreading (ϕ_2 and ϕ_3) roughly correspond to the continuous actuation case in terms of maximum acetone concentration.

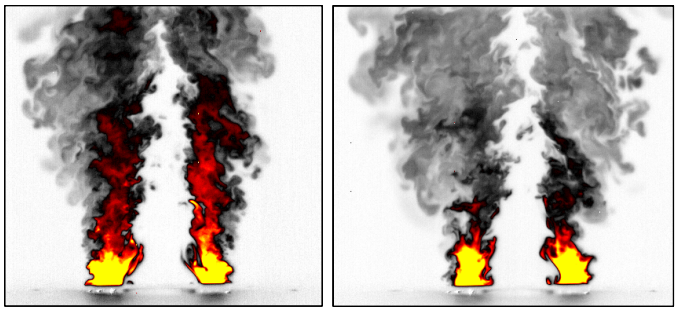

Figure 4.7. Side views of the coaxial jets showing x/D_o = 0-3 for both 9-on and one phase of 40 Hz amplitude modulated 9-on (9-pulsing).

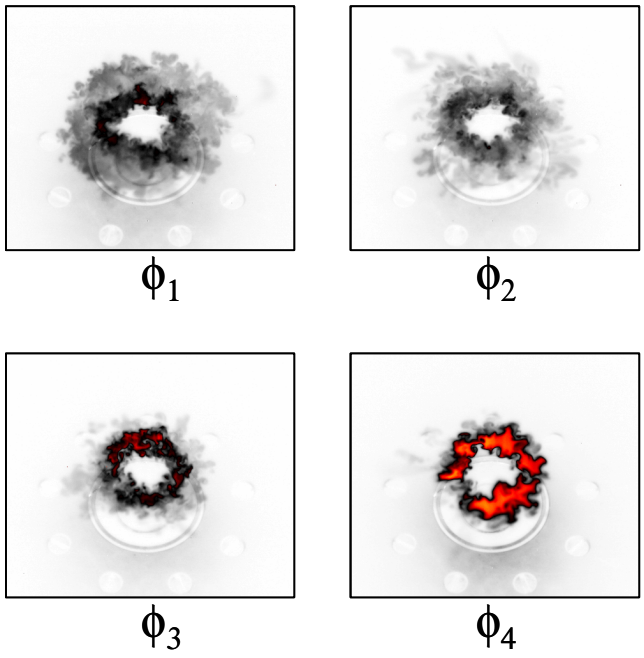

Figure 4.8. Equally-spaced phases of 50 Hz amplitude modulated 9-on actuation (9 pulsing) at x/D_o = 0.5 in the coaxial jets.

Figure 4.9 shows images of the pulsing case at three downstream locations. The phase of each image with respect to the forcing was chosen to track the largest jet diameter. The maximum concentration at x/D_o = ½ is significantly less than the maximum in the non-actuated case at the same height. Higher up, the maximum concentration of acetone drops as the acetone becomes more uniformly spread over a larger area. By x/D_o = 3, the acetone has mixed almost to the center of the faster jet of pure air.

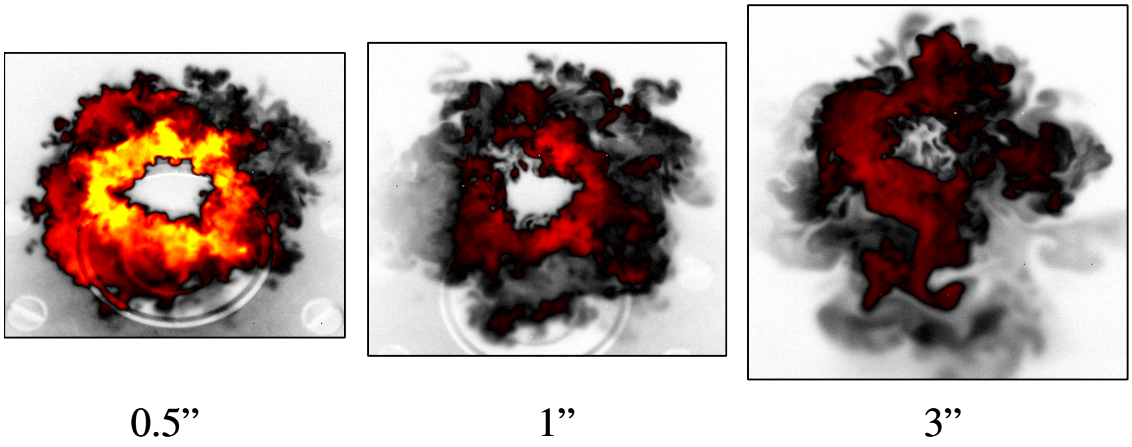

Figure 4.9. Cross-section images of the coaxial jets at x/D_o = 0.5, 1 and 3 for the individual phases of the amplitude modulated actuation with maximum jet diameter at that downstream location.

The influence of pulsing frequency is illustrated in Figure 4.10. The acetone image at the phase of maximum jet width is shown for each frequency. The maximum concentration for these actuated jets is again less than that of the non-actuated jet at x/D_o = ½. The largest jet spread is found for 50 Hz modulation, with diminishing jet spreading as the modulation frequency is reduced. At higher frequencies, the actuators also gave diminishing returns as the number of synthetic jet pulses in the amplitude modulation got smaller, with an upper limit of 100 Hz.

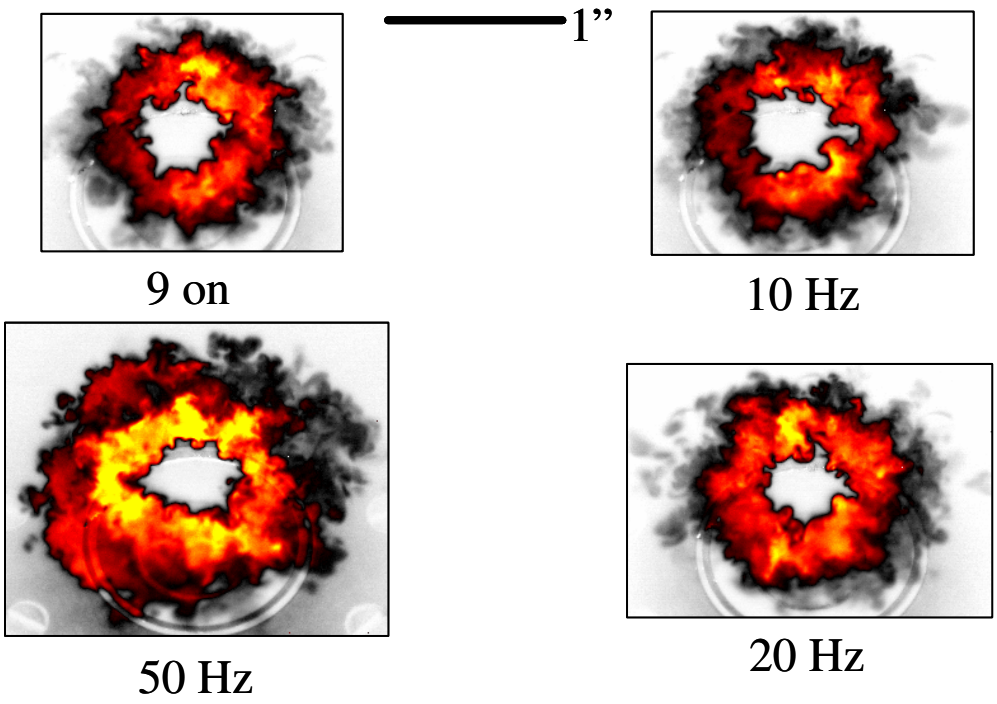

Figure 4.10. Jet cross-sections at $x/D_o = 0.5$ for three frequencies of amplitude modulation (10, 20 and 50 Hz) and 9-on as a comparison. The phase with the maximum jet width for each frequency is shown. The colorbar is different for each image to better show the variation of acetone mixture fraction in each cross-section.

6 Spinning

When the six-on configuration is coupled with amplitude modulation in such a way that the location of the six actuators that are “on” rotates around the jet axis, the jet begins to corkscrew. This can be seen in side views of the single jet case (Figure 4.11) where 40 Hz modulation is employed. This pattern indicates the ability of the actuators to control

the acetone distribution both spatially and temporally, a useful feature for responding to undesirable conditions in an engine.

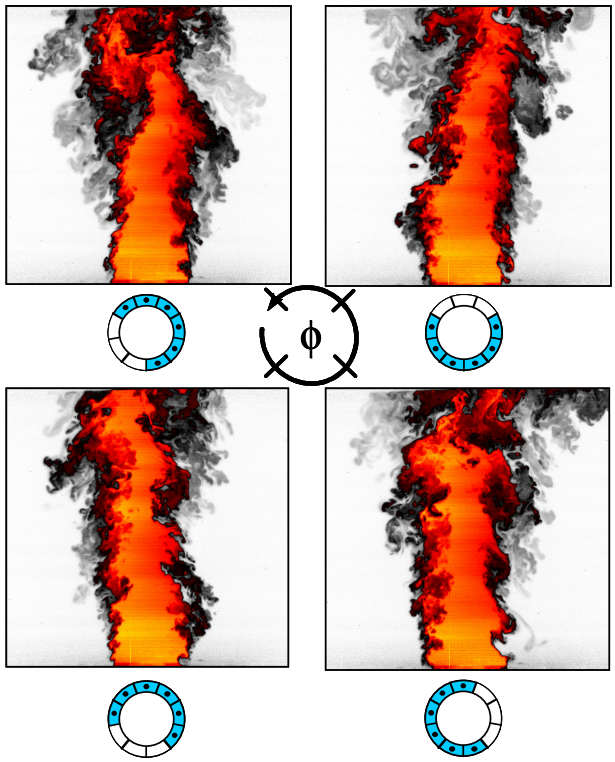

Figure 4.11. Side views from x/D = 0-4 of four equally spaced phases of 40 Hz spinning of the 6-on actuation configuration for the single jet.

Figure 4.12 compares the effects of asymmetric actuation at x/D_o = ½, with 6 actuators on and 3 off for the coaxial jets. The active actuators are centered at the left side of the image for both the 6-on case and the selected phase of 6-spinning actuation. With the low modulation frequency (10 Hz), the spinning mode produces results very similar to those of the steady 6-on case with the added benefit of moving the asymmetric effect around the annulus. Hot-wire velocity measurements taken in a similar facility[13] show that a mean tangential velocity is induced by the spinning actuation. This spinning

motion further increases the mixing, seen by the reduction in near field acetone levels on both sides of the annulus and the greater jet width farther downstream.

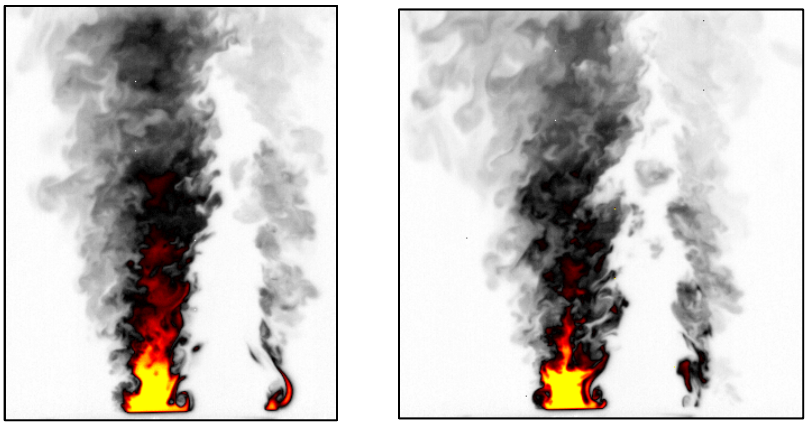

Figure 4.12. Side views from x/D_o = 0-3 of 6-on and one phase of 6-on spinning at 10 Hz in the coaxial jets.

Four equally spaced phases of the spinning actuation at x/D_o = ½ are shown in Figure 4.13 for 10 Hz spinning. The asymmetric actuation creates a concentrated region that progresses tangentially as the phase changes. The pattern is essentially identical to that of the non-spinning asymmetric actuation case, except that it rotates now. The maximum acetone concentration in the strongest region is again significantly less than that of the non-actuated case, showing the increase in mixing due to entrainment of air.

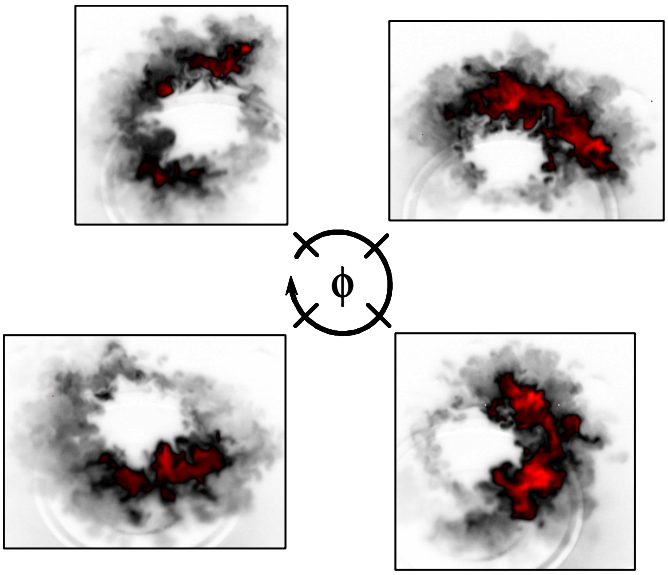

Figure 4.13. Cross-sectional views at $x/D_o = 0.5$ of four equally spaced phases of 6-spinning actuation.

The effects of different spinning frequencies are shown in Figure 4.14. The 10 Hz case is very similar to the non-spinning case, but the acetone is not as completely removed from the non-actuated portion of the annulus. Still, the entrainment greatly reduces the maximum acetone concentration compared to the non-actuated case just as the 6-on case did. As the frequency increases, however, the annulus gets more uniform in concentration. At 50 Hz, there is only a small region of minimum concentration remaining. This is because the clockwise spinning of the actuation pattern imparts a clockwise swirl. The actuators get less time to pull the acetone towards any one direction before the pattern rotates to the next location as the frequency increases, resulting in smearing of the acetone around the annulus.

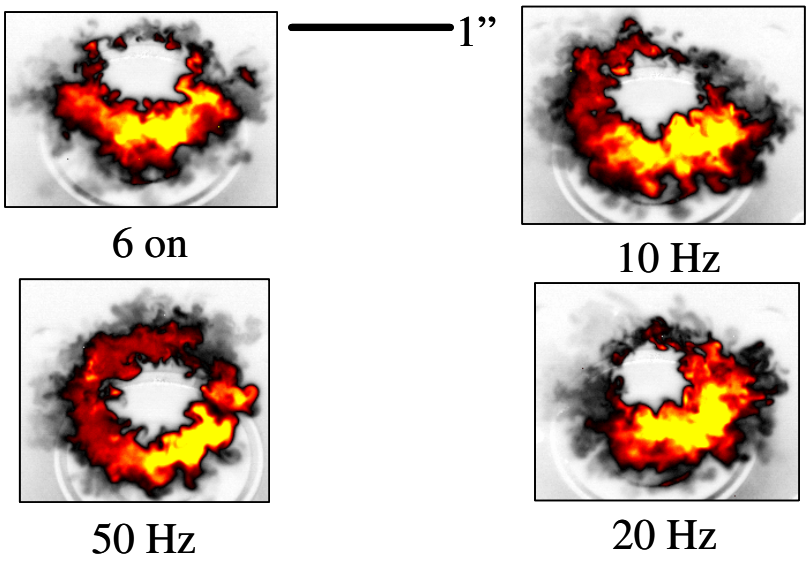

Figure 4.14. Cross-sectional images of the coaxial jets at $x/D_o = 0.5$ for 6-on and three frequencies (10, 20 and 50 Hz) of 6-spinning actuation.

Figure 4.15 shows the change in jet cross-section with height for the same phase. Farther downstream, the acetone profile becomes more uniform, with a shrinking region of high acetone (annular jet fluid) concentration. The maximum acetone concentration decreases with height as more air is entrained and the acetone is spread over a greater area. By $x/D_o = 3$, the actuated jet has roughly doubled its outside diameter and has filled in the center hole.

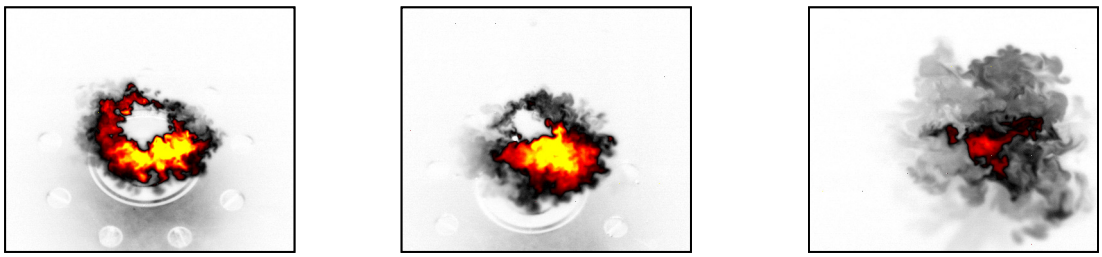

Figure 4.15. Cross-sectional images of the coaxial jets at $x/D_o = 0.5$, 1 and 3 for one phase of 10 Hz 6-spinning actuation.

This chapter evaluated synthetic jets over a wide range of actuation cases and in two different flow fields. The actuators proved their effectiveness at enhancing mixing by creating small scale structures on the periphery of both a single jet and coaxial jets. Applying different spatial patterns of actuation showed that the synthetic jets could significantly alter the spatial distribution of acetone in a controlled way. Comparison of two different directions of actuation on the single jet indicated that axial forcing parallel to the jet was more effective than radial forcing into the center of the jet. The results may be different for coaxial jets, since they have an inner air flow that the radial forcing could help mix into the annulus as well as the entrained ambient air. The addition of amplitude modulation to the actuation demonstrated the ability for temporal control of the acetone distribution as well as spatial distribution. Low frequencies were found to be best for spinning the actuation pattern around the flow, but higher frequencies worked better for pulsing all the actuators. The end result of these findings was to define a smaller set of conditions for further examination: axial actuation in 9-on and 6-on configurations, both with and without amplitude modulation (one frequency), applied to single and coaxial jets. The next chapter examines quantitative measures of the mixing for the various cases and how the synthetic jet actuators cause these effects.

CHAPTER 5

QUANTITATIVE MIXING MEASUREMENTS

Results in the previous chapter qualitatively demonstrated that the synthetic jet actuators have the capability to create the desired mixing and control effects on the jet flow fields. This chapter focuses on quantifying the mixing control and enhancement. Because the mixing system uses nine actuators equally-spaced around the jet exit, there is a built-in asymmetry to measurements made on a diametrical line through the flow. This will be used to demonstrate the maximum and minimum effects of the actuators azimuthally. The mixing effects at other azimuthal locations should be between these two extremes, thus reducing the number of measurements needed to characterize the effects of the actuators. As a reminder, the measurements are not resolved down to the molecular mixing scales (56 - 84 μm), so the term mixing is used to refer to mixing down to the resolution of the imaging system (170 μm). As a reminder, error estimates for the measurements (<6% of the local value) are in Chapter 3. The chapter begins with measurements in the single jet before moving to the coaxial jet results. In both cases, global measures of mixing are presented first, laying a foundation for the radial profile results that follow.

Single Jet

Global Results

One consequence of this measurement technique is to have a quick way to represent the results in a summary form. By defining the jet edges as f = 0.01 to limit the domain, global measurements are possible for each cross-section location. These present a quick representation of the local results without providing any radial information. The first flow field presented is the one-inch diameter round jet with a mean axial velocity of approximately 14 m/s.* As a reminder of the overall flow field structure, Figure 5.1 shows the mixture fraction for the unforced jet, the jet with 9 on actuation, and the 9 pulsing case for the phase with maximum jet spreading. The most important features to notice are the regular small-scale structures due to the high frequency actuation and the broadening on each side, as discussed in Chapter 4. The greater width in the 9 pulsing phase, compared to the unforced and 9 on cases, is also apparent.

*The velocity changes over time due to the changing acetone seeding as discussed in Chapter 3.

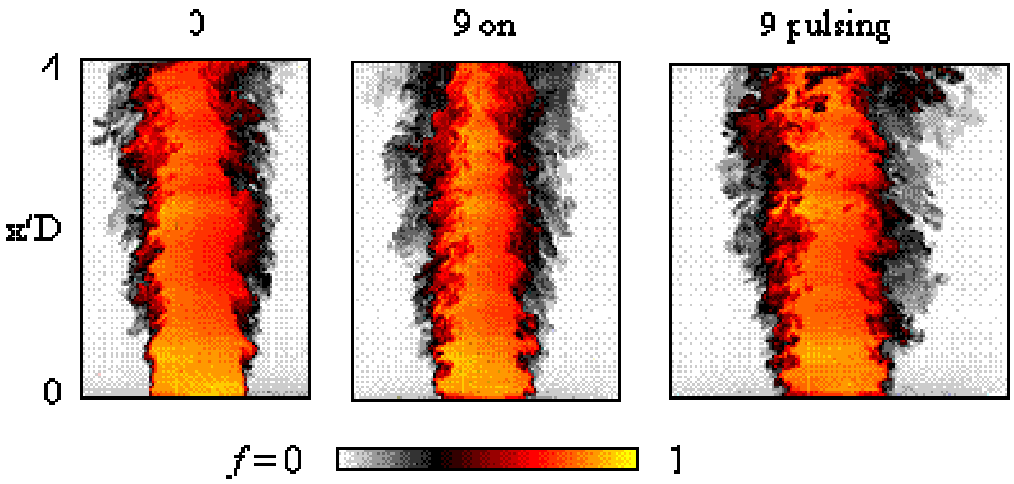

Figure 5.1. Instantaneous side view images of the single jet for the unforced, 9 on and 9 pulsing cases (one phase).

Sets of 1000 images were obtained at each condition to provide statistically significant, quantitative measurements of the single jet. In order to reduce data storage requirements, these large data sets were obtained for horizontal strips five pixels high (~0.85 mm) with a downstream spacing between strips of $\Delta x/D = 1$. The five rows were averaged for each image to reduce the noise, providing one radial profile at each downstream location. The numerical results are all obtained from these data strips and not from full images of the flow field like those shown above in Figure 5.1. The numerical results presented here are based on the average mixture fraction profile at each location. Statistics were also calculated by averaging the instantaneous values, yielding similar results but with greater noise. For clarity of presentation, the values from the average profiles were chosen for presentation.

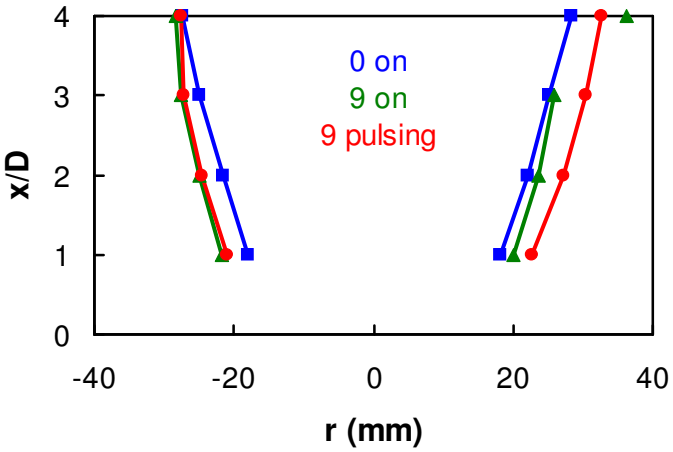

Figure 5.2. The single jet edges ($\bar{f}$ = 0.05) for the three actuation cases versus downstream location. The jet exit edges are at ± 12.7 mm.

Figure 5.2 provides one measure of quantitative jet mixing based on the amount of jet spreading downstream. The figure shows the locations (contour) where the *mean* mixture fraction ($\bar{f}$) reaches 0.05, which can be used to define the edges of the jet. If one considers 0.05 as the stoichiometric mixture fraction of a fuel, then this can also be thought of us defining the average location where combustion might occur in the flow (ignoring the changes heat release would make in the flow field). The results show how the jet width increases downstream and how it varies between the cases. Both actuated cases result in wider jets than the unforced jet. While the unforced jet is nominally symmetric, the forced cases exhibit differences between the left and right sides of the jets. These are due to the laser sheet passing between two actuators on the left and crossing directly over the center of one actuator on the right. The right side of the jet shows enhanced jet growth with amplitude modulation, while the left side seems unaffected by

the modulation compared to constant (9 on) actuation. By four diameters downstream, the forced jets are becoming similar to the unforced jet, especially on the left side. The sudden growth of the right side of the 9-on case at x/D=4 is an artifact of noise in the data creating a false value far downstream. Because this data point is at the very edge of the laser sheet, it receives the strongest signal correction, so a low level artifact gets scaled into something large enough to reach the 0.05 limit.

Figure 5.3 presents another quasi-global measure of mixing improvement, the change in the width of the mixing layers for the different cases. This is indicative of how large an area the mixing could effect for pattern factor control, for example. Here, the mixing layer is defined as the region where $\bar{f}$ is between 0.05 and 0.95. The results are quite different due to the asymmetry of the actuation between the right and left sides of the given cross-section, so each side is listed separately. The large structure generated by the amplitude modulation on the right side creates the widest mixing layer. However, modulation has a downside. The left side of the continuously actuated jet had a wider mixing layer than the pulsing case. A likely reason is the reduced actuation time associated with the less than 100% duty cycle for amplitude modulation. It is interesting to note that the small scale mixing case (9-on) produces better mixing (a wider mixing layer) on the side between two actuators (left) while the pulsed case has better mixing directly over an actuator (right side). Note that these results qualitatively agree with the side view images of the jet shown above in Figure 5.1.

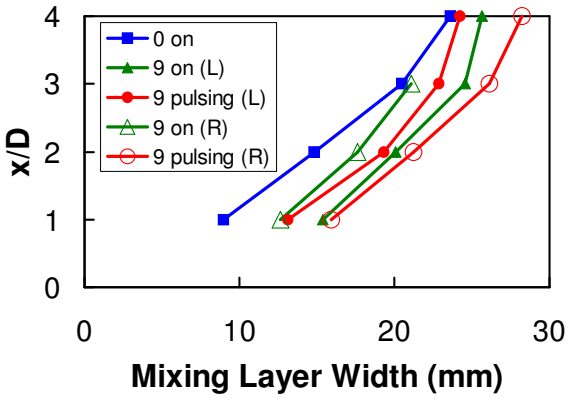

Figure 5.3. Mixing layer widths ($0.05 < \bar{f} < 0.95$) for each side of the actuated jets versus the average for the unforced jet.

A third measure of mixing efficiency is the total unmixed fluid fraction at each downstream plane (Figure 5.4). The unmixed fluid fraction is the ratio of the amount of pure fluid ($\bar{f} > 0.95$) at the given downstream location normalized by the amount at the jet exit. This is a useful measure for nonpremixed combustors, where the amount of pure fuel is an important concern. The pure acetone is integrated with the appropriate area weighting based on each pixel's radial location. As expected, the amount of pure fluid decreases quickly downstream for all cases. The increase in small scale mixing from the high frequency excitation causes more areas to be well mixed. The nine-pulsing case actually has more pure jet fluid than the nine-on case although significantly less than the zero-on case. The small increase stems from the large scale entrainment structures generated by the low frequency modulation. These structures move large amounts of jet fluid around but do not necessarily mix it at the small scales. The amplitude modulation also necessitates a duty cycle for the actuators, reducing the amount of energy being added to the flow.

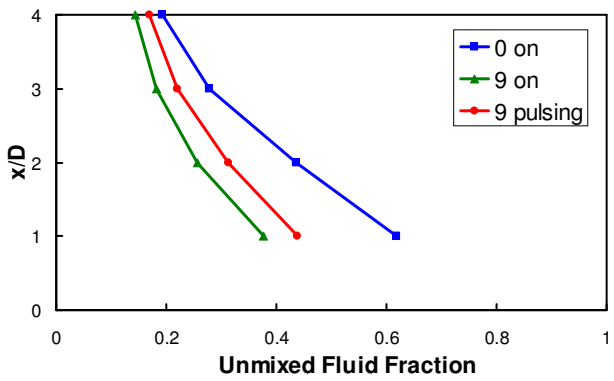

Figure 5.4. Unmixed fluid fraction ($\bar{f} > 0.95$) versus downstream location for each actuation case in the single jet.

Local Results

More detailed analysis results come from examining the spatially resolved, radial profile of mixture fraction. Figure 5.5 shows the $\bar{f}$ profiles for the three modes of actuation (no forcing, 9 on, and 9 pulsing) at four locations downstream. There are two main things to notice from the profiles. Most obvious is that initially the unforced jet has a thinner mixing layer with a steeper gradient and a wider area of pure jet fluid in the center. The difference decreases downstream, though. It is also clear that all three cases are more similar on the left side than the right. As noted previously, the laser sheet, which comes from the left, passes between two actuators on the left side and directly over an actuator on the right side. Apparently the structures generated by the actuators do not quickly coalesce azimuthally. Note that this causes the 9 pulsing case to stay significantly broader than the 9 on case on the right side of the jet for this cross-section. Also note that inner core of pure jet fluid is wider for 9 pulsing than in the 9 on case, as seen in the jet images in Figure 5.1. Since this is a nominally symmetric jet, the

difference between cases should vary azimuthally between the two extremes these profiles show.

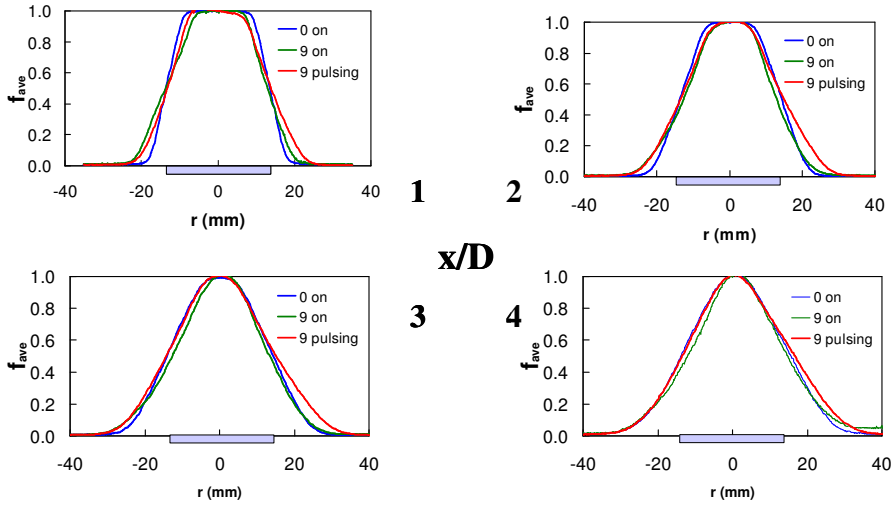

Figure 5.5. Mean mixture fraction profiles for all three actuation cases at four downstream locations.

The profile of the root-mean-squared (RMS) deviation of the local mixture fraction from the mean (f') is shown in Figure 5.6 for the same cases. As expected, the highest RMS values occur in the mixing layer (the region in the mean profiles, Figure 5.5, where the mixture fraction varies between 0 and 1). In the mixing layer, large scale structures of fairly pure air or jet fluid can sometimes be present, as well as better mixed small scale structures. The increase in the width of the region of high RMS fluctuations shows that the mixing layer is broader in the actuated cases, consistent with the *mean* mixing layer results presented above. For the actuated cases, the decrease in *peak fluctuation magnitude* in the mixing layer for the first two diameters downstream indicates an improvement in mixing caused by the synthetic jets. Lower peak fluctuations at a given location suggest less chance of seeing pure jet fluid or air. The closer similarity of the

RMS profiles further downstream shows that the natural jet mixing process can achieve the same mixing as the forcing, but need longer to do it.

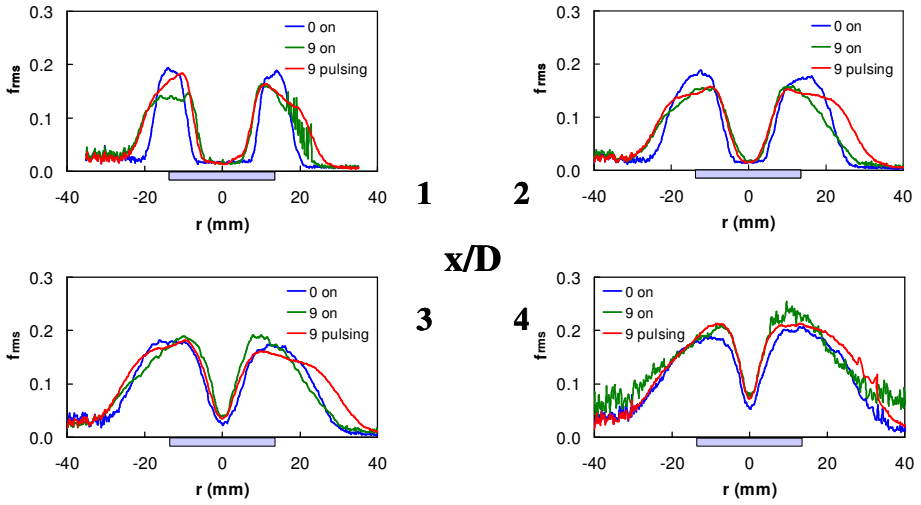

Figure 5.6. RMS mixture fraction fluctuation profiles for all three actuation cases at four downstream locations.

The mean and RMS profiles represent the zeroth and first moments of the mixture fraction distribution. A more complete statistical representation of the data is given by the probability density function (pdf). The value of the pdf for a given location, P(f,x,r), represents the probability of mixture fraction f occurring there. For a given downstream location, we have a two-dimensional function, P(f, r), which is presented here as a pdf image. An example is shown in Figure 5.7, along with three one-dimensional pdf plots at specific radial locations used to demonstrate interpretation of the image. The horizontal axis in the image is the radial location, while the vertical axis is mixture fraction. The probability is represented by the intensity of the image for each mixture fraction and location. Thus, vertical cuts through a pdf image provide the pdf for the corresponding

points in space. A horizontal cut (not shown here) gives the spatial distribution of points having a specific mixture fraction.

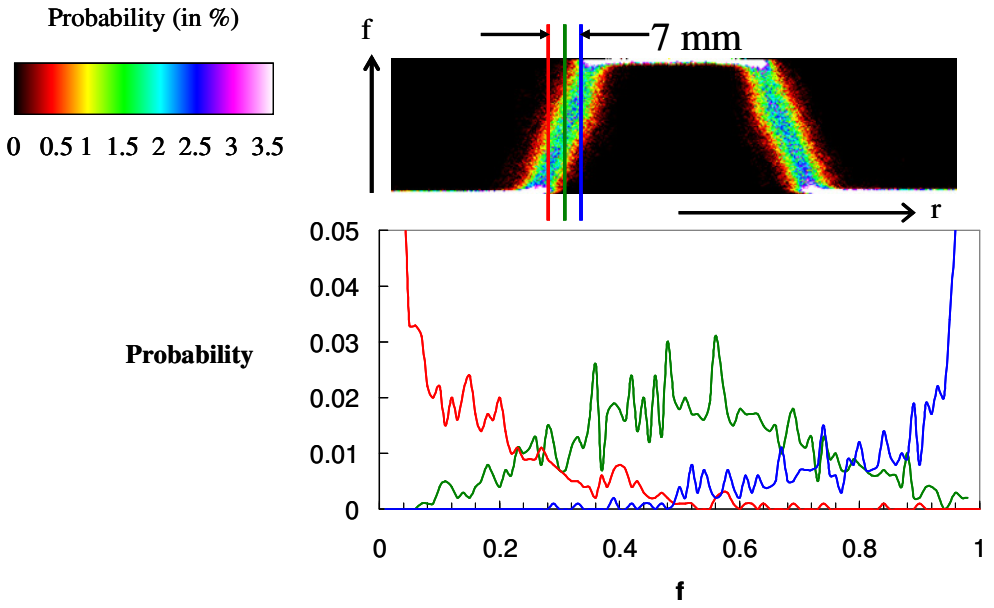

Figure 5.7. Explanation of a PDF image, including three one-dimensional pdf profiles.

Figure 5.8 presents pdf images at x/D of 1 for the unforced (0-on) and 9-on cases, as well as eight phase-locked pdfs and the overall phase-averaged pdf image (i.e., statistics for all the phases) for the 9-pulsing case. Since a pdf image provides a complete statistical representation of the results, many things can be seen from the pdf images for the three cases at x/D = 1. The increased jet width due to actuation is again obvious from the wings of the pdf images, but the phase-locked images tell an even more interesting story. These eight equally spaced phases show the change in jet fluid distribution over the modulation cycle. The 30° phase shows plateaus at f ~ 0.5. These indicate regions of uniformly mixed fluid spread radially. The distribution then relaxes towards the 9-on case as a steady-state is reached over the next four phases (75° – 210°). The similarities

between the 9-on pdf image and the 120° – 210° 9-pulsing phases are striking. In the remaining three phases (255° – 345°), when the actuators are stopped by the modulation signal, the distribution approaches that of the 0-on case. The phase-averaged 9-pulsing pdf image is similar to many of the phases. The 0-on image and the 345° image are quite similar for f > 0.5 but the low-level acetone is spread wider. Note that the probability of any given mixture fraction is fairly low throughout the mixing layer, but that the pure regions have very high probabilities. These results were expected based on the mixture fraction profiles and fluctuation profiles shown previously (Figure 5.5 - 6).

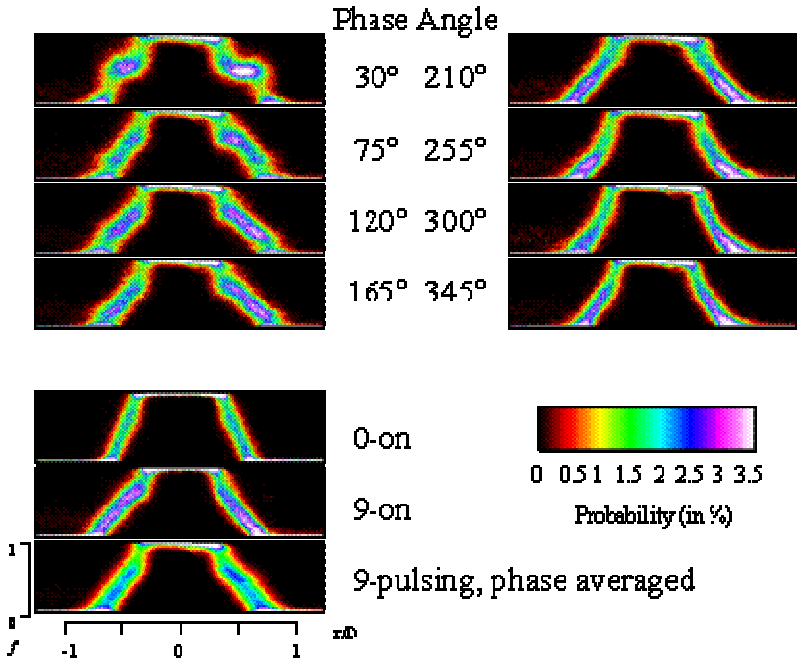

Figure 5.8. Phase-locked pdf images at x/D = 1, as well as 0-on, 9-on and phase-averaged 9-pulsing for comparison.

The beginning of the modulation cycle (0°) generates a sudden pulse of actuation from the synthetic jets, which generates these plateaus at x/D = 1 by 30°. The interaction of the actuator jets with the flow field creates a large-scale structure (the plateaus) and is evidence of the large scale effects of the low frequency modulation. Figure 5.9 follows this flow feature as it propagates downstream. For each inch downstream, the phase of the system increases 45°. This yields a propagation velocity of approximately 8 m/s for 40 Hz modulation, which is roughly the mean axial velocity at this radial location in the flow field (Figure 3.6).

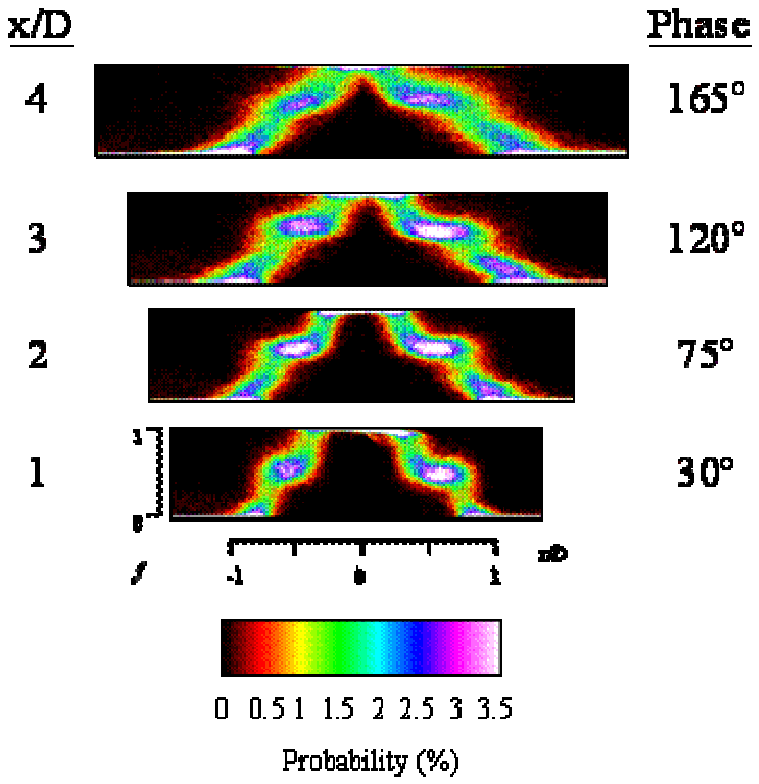

Figure 5.9. Large-scale feature tracked in pdf images in both time (phase angle) and distance (x/D).

As evidenced by several different results, the synthetic jet actuators have a significant impact on mixing in this jet flow field. Unfortunately, they do not seem to be reaching their full potential to enhance mixing since the large scale structures created by amplitude modulation can only mix with the quiescent ambient air on the outside of the jet. This could lead to entrainment limiting the amount of mixing enhancement these large structures cause. If the structures have the size and strength to reach the middle of the flow, synthetic jets applied to a coaxial jet flow field might allow the actuators to maximize their effect by having an inner air flow to mix into the annular fluid as well as entraining ambient air.

Coaxial Jets

The coaxial jet flow field was discussed previously, but deserves a brief overview at this point. A 0.625 inch diameter inner tube is inserted concentrically in the one inch round jet used previously. The acetone-seeded air generally flows in the annulus with pure air flowing in the center jet. The majority of the data is acquired with a velocity ratio (inner jet mean exit velocity / outer jet mean exit velocity) of $U_i/U_o = 0.62$ and a total flow rate designed to match the momentum of a one-inch diameter jet moving at 10.8 m/s. For the numerical results, again 5 pixel (~ 0.85 mm) tall strips of data of data are acquired for the flow fields but with a vertical spacing of only $\Delta x/D_o = 0.25$. Since many more conditions are tested in the coaxial jet configuration, data sets consist of 300 strips with each row used as a separate measurement to yield 1500 results.

Flow Field

As a visual reference for the results, images of the flow field with and without actuation are presented in Figure 5.10. It is plain to see that the actuators are affecting both the inner and outer mixing layers, leading to acetone spreading faster in both directions. As a result, the regions of pure acetone are much narrower. The small scale structures created by the actuators are evident beginning right at the jet exit.

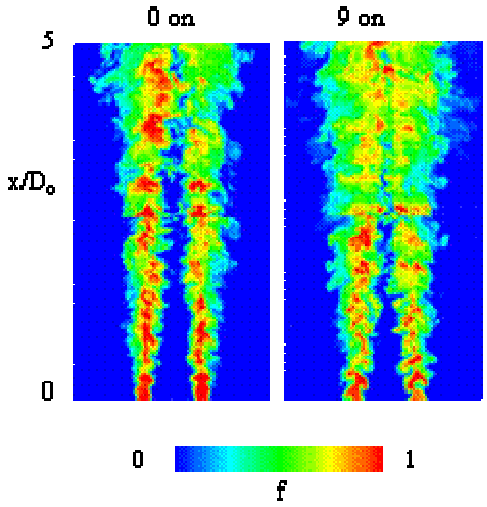

Figure 5.10. Composite instantaneous images of the coaxial jet flow field with and without actuation.

Figure 5.11 shows mixture fraction images at nine equally-spaced phases for 60 Hz amplitude modulation of the ~1200 Hz synthetic jets at $x/D_o = 0–3$. Readily apparent are the large-scale structures created by the low-frequency modulation that persist downstream, unlike the small-scale structures that rapidly dissipate (just as seen in

velocity measurements in a very similar flow field[13]), and allow mixing enhancement by stirring the flows together. More ambient air is entrained, and the surface area of the outer mixing layer is greatly increased. The duty cycle of the modulation is apparent from these images, as the small-scale structures created by the high frequency forcing are again visible near the exit in the phases when the modulation cycle is on (10° – 210°). The large structures do not become visible until farther downstream ($x/D_o > 1$), needing time to form. Note that the flow starts to resemble the case with continuous forcing before the cycle ends except for the remnants of the large-scale structure at the top of the image. In the phases when the modulation cycle is off (250° -330°), there are no small-scale structures but the large structures from the previous cycle are still propagating downstream.

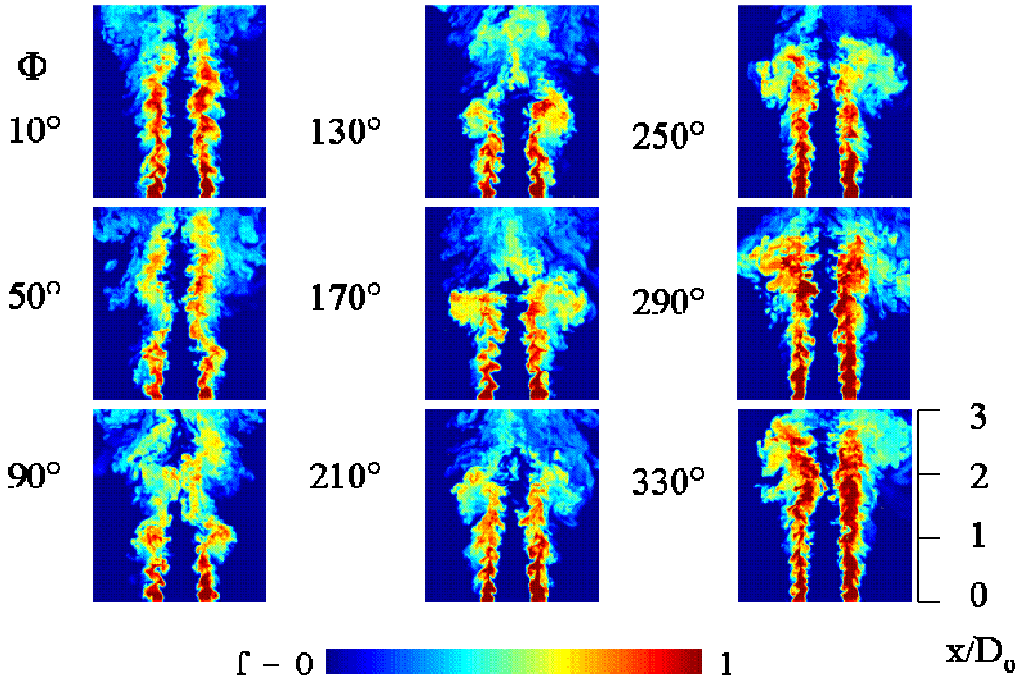

Figure 5.11. Representative images for the nine phases of 9-pulsing actuation in the coaxial jets for x/D_o = 0-3.

Figure 5.12 shows a comparison of the measured mixture fraction to both the normalized streamwise and normalized radial velocities for the beginning of the modulation cycle (10° – 130°). The velocity measurements were made in a very similar facility in a companion effort,[13] and the differences in the facilities are not important for the comparison being made here. The radial velocity (middle) is colored blue for velocity to the right and red for velocity to the left. Comparing the radial velocity to the mixture fraction, it is easily observed that the large-scale structures correspond directly to the radial motion shown in the velocity plots. The start of the duty cycle, when the actuators first begin to suck in fluid, starts to generate outward radial velocity. It also reduces the streamwise velocity. As the flow reaches $x/D_o = 1$, the large-scale structures begin to roll outward. The combination of the reduced streamwise velocity and the outward radial velocity results in a region of low acetone concentration that almost spears as a break in the flow. It also causes the flow to pinch acetone into the middle as the radial velocity is inward in this region. Based on these images, the large structures are created by the beginning of the duty cycle when the synthetic jets pull the annulus outward and then that annular fluid runs into the actuator jets and is pushed outward. The large structures also clearly impact the inner mixing layers as well as the outer mixing layers, lending credence to the hypothesis that amplitude modulation can be more effective at mixing enhancement in coaxial jets than in the single jet.

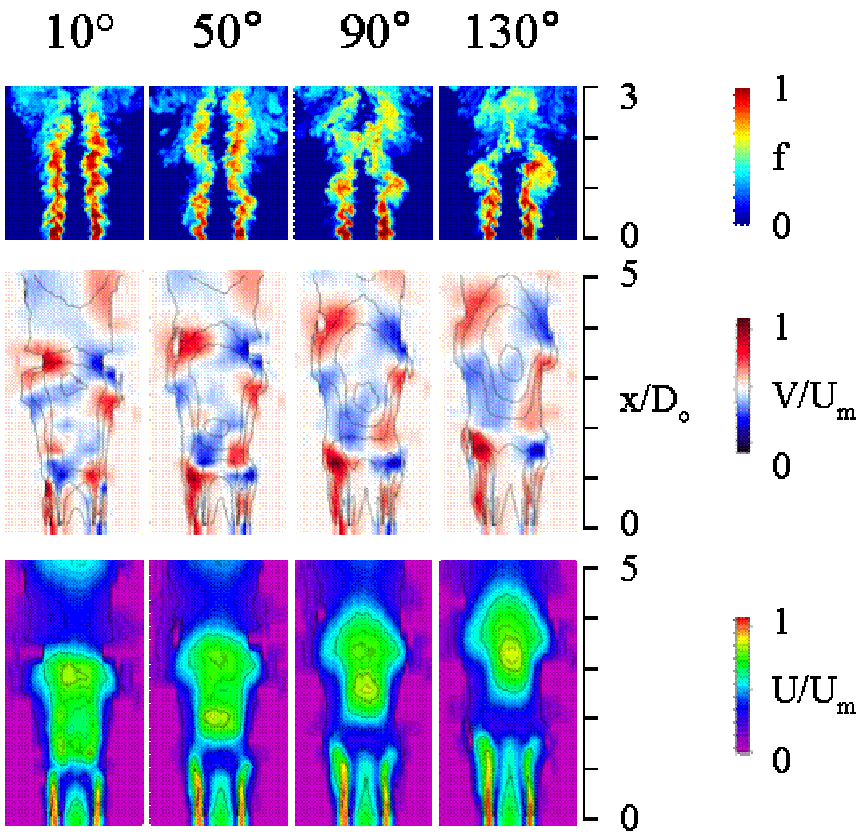

Figure 5.12. Comparison of mixture fraction (top) to normalized radial (middle) and axial (bottom) velocity for four phases of 9-pulsing actuation in the coaxial jets.

Global Results

As a reminder, the jet edges are defined as f = 0.01 in each instantaneous slice to limit the domain for making global measurements. These present a quick representation of the local results without providing any radial information. Figure 5.13 shows the global average mixture fraction ($\bar{f}_{global}$) at each downstream location for each actuation case. This value is the area-weighted average of the mixture fraction throughout the jet,

averaged over all the slices at that height. The 9 pulsing case (phase averaged) has the lowest value everywhere while the unforced jet always has the largest mixture fraction, showing that the actuation is effective at mixing the air and acetone. This result comes from the width of the annulus increasing with the actuation cases, spreading the same amount of acetone over a larger region. The outlying data point at $x/D_o = 1.75$ for the unforced jet appears to be an artifact and not a real deviation from the neighboring values. The most important, and expected, result is the trend of the average f to decrease downstream for all cases as the flow widens.

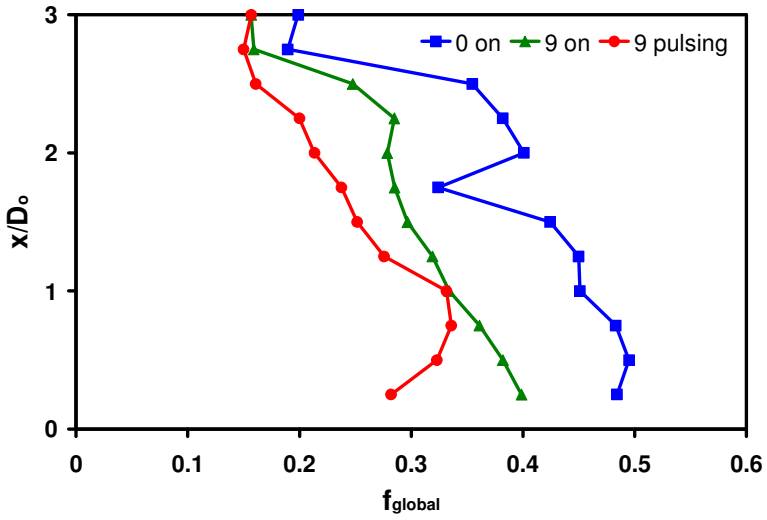

Figure 5.13. Global average mixture fraction versus downstream location.

In addition, the global average RMS fluctuations of f (f'_{global}) at each downstream location can be calculated (Figure 5.14). These are the fluctuations of the global mixture fraction from each slice compared to the average value discussed above. One would expect the RMS fluctuations to decrease downstream in all cases as the amount of pure

fluid (air or jet fluid) in the flow field is reduced by mixing, and this is clearly seen in Figure 5.14. From the single jet data, it is also expected that the actuation will decrease the magnitude of the fluctuations. The large scale structures created by amplitude modulation further reduce the fluctuations after $x/D_o = 1.25$, when the structures become readily visible in images. However, these results do not indicate if the lowered values are due to increased mixing from the actuation or are more influenced by the width of the jet which should be increasing with downstream distance and actuation.

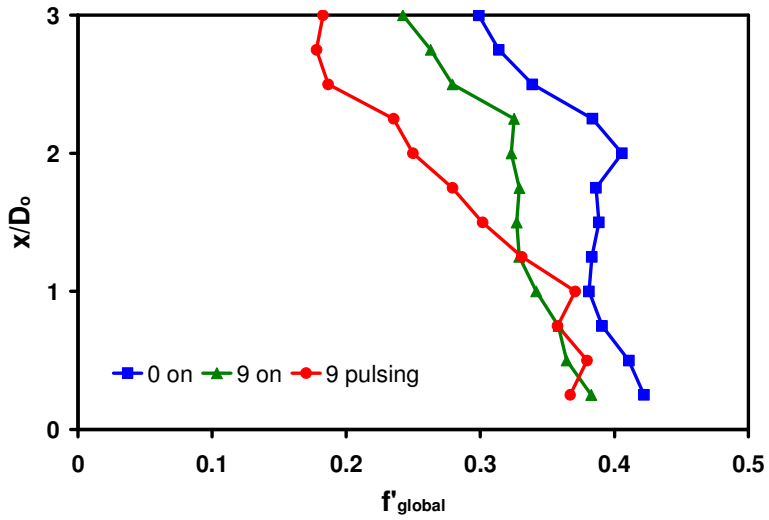

Figure 5.14. Global RMS mixture fraction fluctuations versus downstream location.

To evaluate the effect of jet width or spreading, it is helpful to look at the edges of the jet. As the statistics to be evaluated now require knowing the radial distribution of f, all the following results will be based upon the mean profile of the average mixture fraction distribution at each downstream location. Using that data, the edges are defined as the location where $\bar{f} = 0.05$ to eliminate noise from influencing the values. As seen in Figure

5.15, the unforced jet is the narrowest. The 9 on and 9 pulsing cases both start out (at x/D_o = 0.25) wider than the unforced case by an amount equal to the spacing of the synthetic jets from the annular jet exit. From that starting point, the 9 on case parallels the growth of the unforced case with both having a spread half-angle of 9.2°. The 9 pulsing case starts out with slightly faster growth (12.3°) up until approximately x/D_o = 1.25, then once the large scale structures take hold the growth doubles to 24.5°.

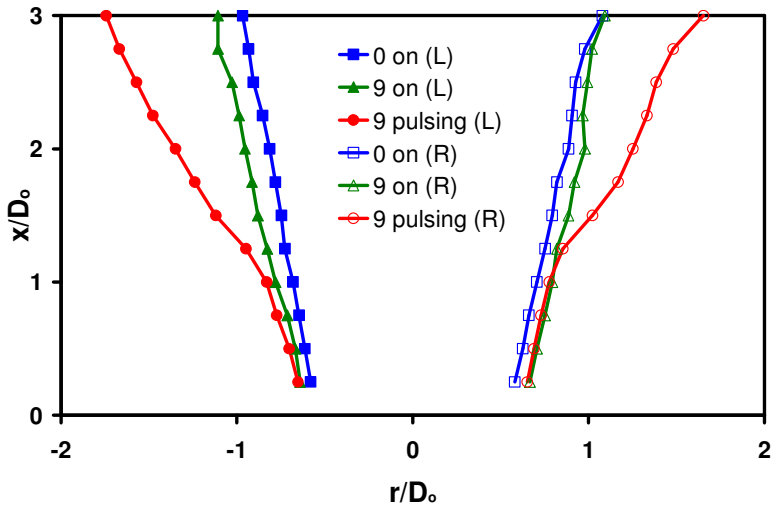

Figure 5.15. Comparison of the jet edges for all three actuation cases in the coaxial jets.

Even a casual glance at the jet edges shows an asymmetry between the left and right sides of the flow for the 9 pulsing case. As has been mentioned previously, the left side of the flow is between two actuators while the right side is directly over one. Figure 5.16 shows the same jet edges plotted in radial distance to simplify comparison of the two sides. The unforced edges are similar, but not quite equal, indicating a slight angle to the right of vertical for the flow. Note that the actuators in the 9 on case pull the flow to the

left, having the effect of straightening the flow since the data were acquired immediately after the unforced data without any adjustment of the system. This is similar to the result seen in the single jet, which was symmetric in the unforced case resulting in the 9 on case being wider on the left than on the right. The asymmetry of the 9 pulsing case is readily apparent, with the left side significantly farther out than the right side from the very beginning. In the single jet, this was reversed with the right side farther out. The flow in the annulus is approximately the same speed as the single jet, so there is no reason to expect a significant difference in the response to actuation. However, the coaxial jets present a wake-like flow with a lower velocity in the center. This will reduce the outward jet spreading that moves more jet fluid above the actuators, changing the effects of the actuators on the jet edges from the single jet case.

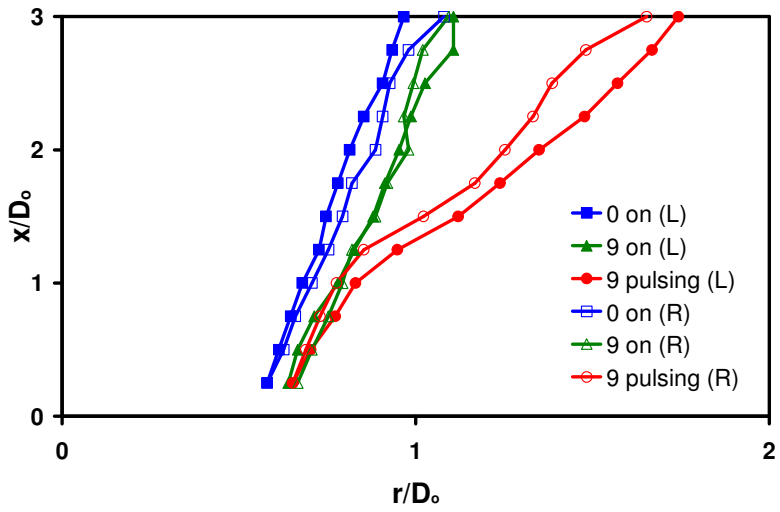

Figure 5.16. Comparison of the left and right jet edges for all three actuation cases in the coaxial jets.

In terms of evaluating the effects of the actuators on mixing, an important measure to look at is the mixing layer width on the outside of the flow field. This is where the actuators are located, so their effects should be strongest here. The mixing layer width is defined here as the region between the jet edge ($\bar{f} = 0.05$) and the beginning of the nearly pure fluid ($\bar{f} = 0.95\ \bar{f}_{max}$, where $\bar{f}_{max}$ is the peak mixture fraction at the given downstream location). A rigid cutoff of $\bar{f} = 0.95$ was not used here because the annulus is too small to allow pure fluid to persist downstream, unlike the single jet. In fact, it only persists to $x/D_o = 0.5$ for the two actuated cases. Figure 5.17 compares the left and right side mixing layer widths for all three cases. As with the jet edges, the unforced jet has the narrowest mixing layers and shows linear growth downstream. The two sides are virtually identical, as should be expected for an axisymmetric flow. The 9 on case again parallels the unforced case with an initial offset due to the actuators. The left and right sides are very similar with the left side being slightly larger (~1 mm) most of the time. The single jet showed a different effect since the left side was larger than the right side the entire time. The 9 pulsing case begins much like the 9 on case, with a sudden change in the growth rate starting at $x/D_o = 1.25$. The left side is always larger than the right side, generally by 2 mm or more. This is in contrast to the single jet result, but can be explained by the nature of the large scale structures. In the single jet (Figure 5.1), the large scale structures are not as clearly defined as those seen in the coaxial jets (Figure 5.11). The right side is a larger structure in both cases, but in the coaxial jets it moves the entire fluid stream out to the right, resulting in a smaller mixing layer width than on the left where the geometry keeps the pure fluid farther in towards the center. This leads to

the difference in statistical results because there is always a pure inner core in the single jet that does not get moved out with the structure.

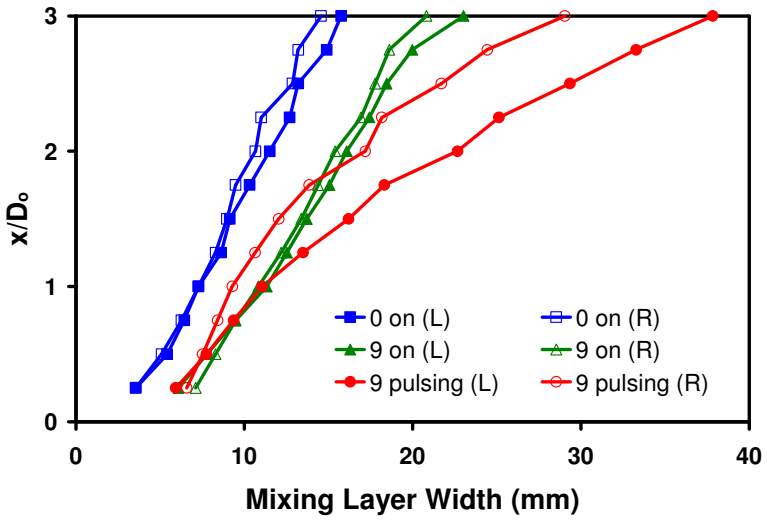

Figure 5.17. Comparison of the left and right outer mixing layer widths for all three actuation cases in the coaxial jets.

In the coaxial cases, it is also important to consider the inner mixing layer width (Figure 5.18). This has the same defined cutoff values as for the outer mixing layer width ($\bar{f}$ = 0.05 and 0.95 $\bar{f}_{max}$), but by x/D_o = 1 the center region begins filling with acetone, i.e., the two inner mixing layers are merged. The mixing layers are narrower than on the outside of the flow, which makes sense with a smaller shear between the two jets than with the ambient air. The distance from the actuators also makes it harder to influence since the synthetic jets do not exit directly into the inner mixing layer. The unforced case has the smallest mixing layer as is expected. The asymmetry in the 9 on case is quite large with the right side inner mixing layer being much wider than the left side. The actuators clearly have a strong effect even on the inner jet mixing layer, and it takes about

one inch for the two neighboring actuators on the left side to merge their effects to match the pull of the actuator on the right side. The right side was slightly larger for the outer mixing layer over these downstream locations, and the outer edge is much closer to the actuators making it easier for the neighboring synthetic jets to merge their effects. Because the 9 pulsing results are phase averaged over the duty cycle, it is not surprising to see that the 9 pulsing case has wider mixing layers than the unforced case but less than the 9 on case near the exit. The strongest effects of the amplitude modulation generally are not seen until further downstream. It appears that the pulsing case is mostly showing an average of the effects of the two sides in 9 on, perhaps due to the duty cycle of the modulation allowing the sides to remain more similar. The right is still larger than the left side, but not by such a large margin.

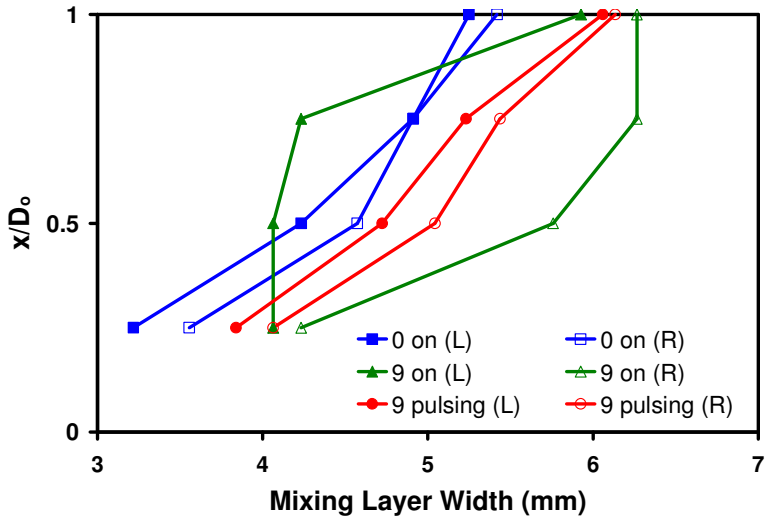

Figure 5.18. Comparison of the left and right inner mixing layer widths for the three actuation cases in the coaxial jets.

The effectiveness of the large-scale structures produced by amplitude modulation is even more evident in a comparison of the rate at which pure annular fluid becomes mixed. Figure 5.19 shows the axial dependence of the radially and azimuthally integrated pure ($\bar{f} \geq 0.95$) mixture fraction value for all three actuation cases, assuming near symmetry in the azimuthal direction in an average sense. The radial integration gives proper weighting to the greater azimuthal area represented by each pixel as the radial distance increases ($A = 2\pi r\Delta$, where Δ = pixel size). The integrated value is thus the integral (or sum) of $2\pi r\Delta\bar{f}$ over all r conditioned on $\bar{f} \geq 0.95$. Continuous forcing, relative to the unforced case, greatly increases the rate at which pure fluid becomes at least partially mixed. Pulsing has an even more dramatic effect. Virtually all the pure fluid is gone as early as $x/D_o = 0.5$, while the forced case does not achieve the same result until $x/D_o = 1.0$, and the unforced flow needs a couple of diameters.

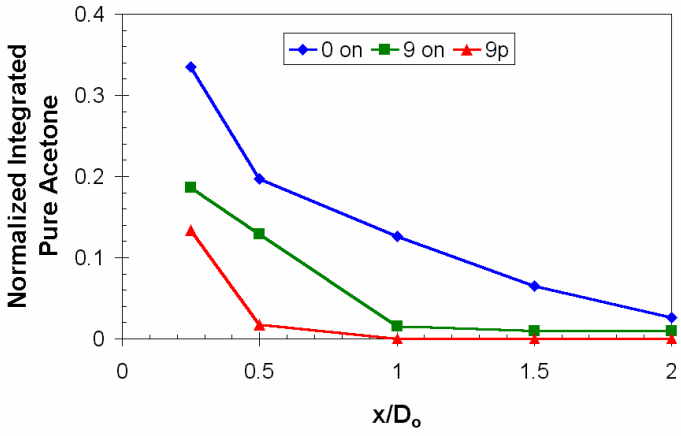

Figure 5.19. Integrated total pure acetone normalized by the exit value for all three actuation cases in the coaxial jets.

Another potential measure of the mixing in the three flows is the average mixture fraction on the centerline of the flow, $\bar{f}(r=0)$ (Figure 5.20). As expected, the unforced case begins with pure air in the center. Then after x/D_o~1, the mixture fraction (of annular jet fluid) increases slightly with downstream distance, and the decay becomes large and essentially linear after x/D_o=2. The 9 on case has a very similar trend, but the rapid decay starts around x/D_o=1 with an increasing slope downstream. The 9 pulsing case is interesting in that it matches the 9 on case until x/D_o = 1.5, when it begins to mix more slowly until it has only matched the unforced case by x/D_o = 3. This shows that while the large scale structures are very effective at moving the fluid out much wider, the small scales more directly impact the mixing.

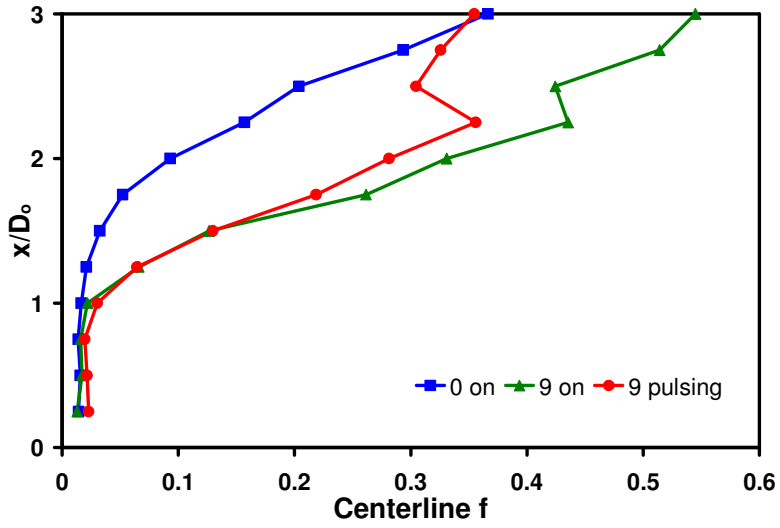

Figure 5.20. Average mixture fraction on the centerline for the three actuation cases in the coaxial jets.

A final statistical measure to consider is the average maximum mixture fraction ($\bar{f}_{max}$) as a function of downstream location (Figure 5.21), which is an important

parameter for mixing down fluid for pattern factor control, for example. The value is steady at $\bar{f}_{max} = 1$ for the unforced case until air begins to mix all the way into the annular flow at $x/D_o = 2$, when it begins a linear decay. The 9 on actuation immediately lowers the value, but it holds steady at f = 0.86 until it begins to decay at $x/D_o = 2$ just like the 0 on case. The 9 pulsing case starts with pure fluid as the maximum, but immediately begins to decay. Farther downstream, as the large scale structures begin to have their full impact, the rate of decay increases. By $x/D_o = 3$, the 9 pulsing has reduced the maximum to f = 0.53, compared to 0.72 and 0.83 for the unforced and 9 on cases respectively. This shows that the primary effect of the high frequency actuation is in the very near field, after which the flow is dominated by the natural, shear-induced mixing processes. The amplitude modulation continues to work downstream, achieving a greater total result despite starting more slowly.

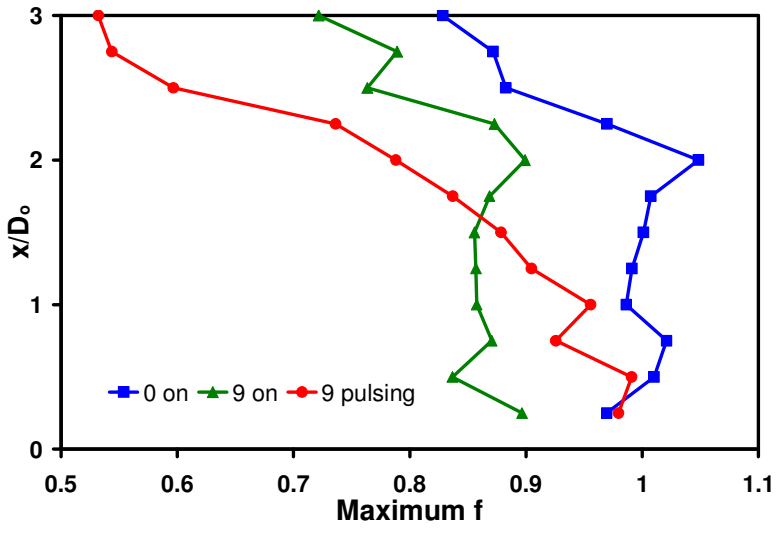

Figure 5.21. The average maximum mixture fraction ($\bar{f}_{max}$) for the three actuation cases in the coaxial jets.

Using the full images, another measure of mixing enhancement can be calculated. Instantaneous mixture fraction contours can be calculated by thresholding images (Figure 5.22). These images show the pixels where f = 0.10±0.025. The changes in the jet edges due to actuation described above are apparent, as is the enhanced mixing into the center flow (especially for 9 on). The contours are more convoluted with actuation as well. Using this as a stoichiometric contour for a hypothetical fuel, this creates a greater surface for combustion. One way to measure this is to calculate the number of pixels in each contour, and normalize by the 0 on case to measure the enhancement. The 9 on case nearly doubles, to 1.93 times the 0 on case, while the modulated case grows to 2.08 times the unforced for the given phase. Averaging over the nine phases, the modulation contour is 2.05 times as large as the unforced contour. This factor would increase more if the surface area was computed by assuming axisymmetry and integrating, but that is not a reasonable assumption based on the small number of instantaneous images. While there are not enough images to draw truly quantitative conclusions, it is clear that the actuation significantly increases the surface area of the flow at a given mixture fraction level.

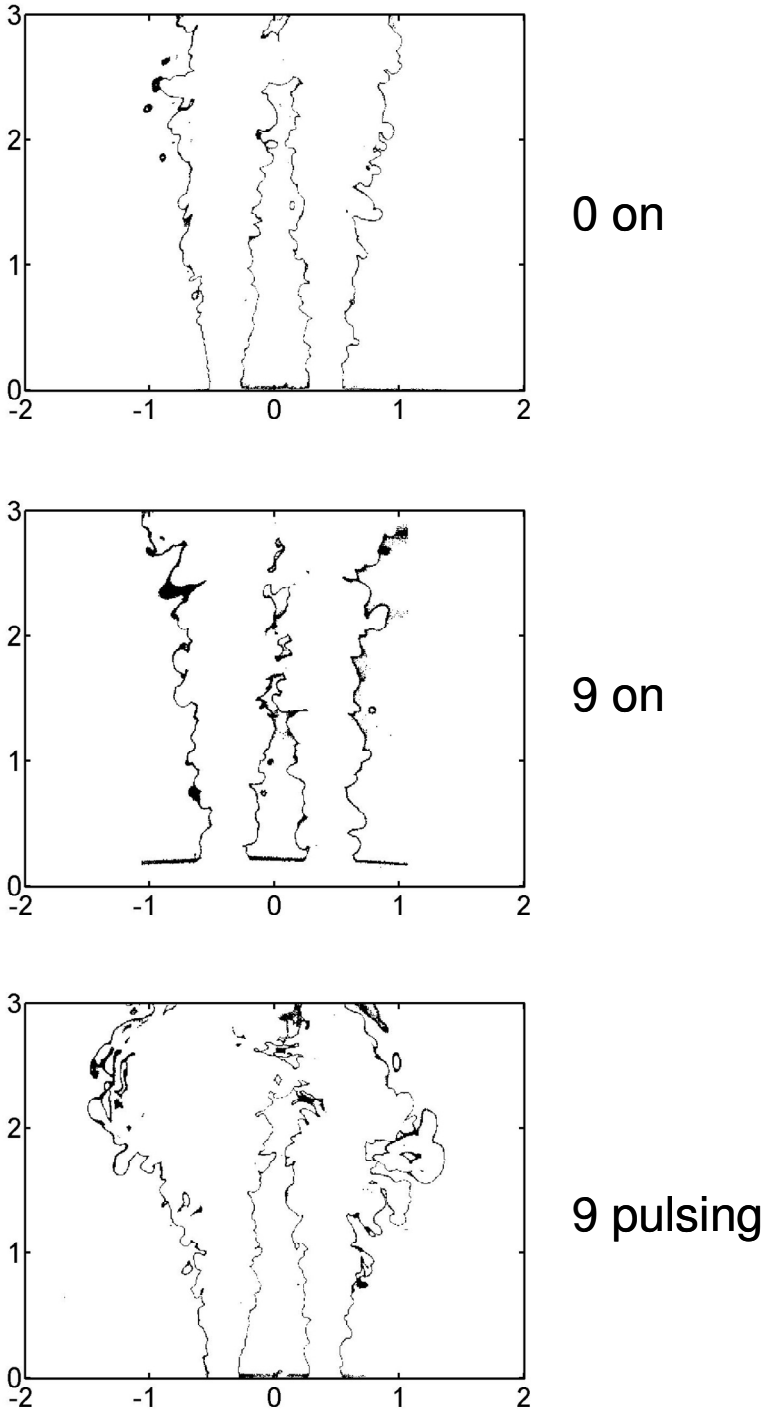

Figure 5.22. Instantaneous mixture fraction contours for f = 0.10 ± 0.025 in the 0 on, 9 on and one phase of 9 pulsing.

Local Results

More detail of the mixing is provided by examining radially resolved mixture fractions. The mixing results for all three cases can be compared by examining the mean and RMS mixture fraction profiles ($\bar{f}$ and f'). Figure 5.23 shows $\bar{f}$ and f' profiles for the three modes of actuation at $x/D_o = 0.25$, with the pulsing case averaged over all the collected phases. The mean mixture fraction profile shows broadening of the flow for both continuous and amplitude modulated forcing. On the right side, where the profile crosses directly over an actuator, the effect is greater than on the left side where the profile splits between two actuators. The peaks in the annulus are slightly lower for the forced cases due to the small-scale structures created by the synthetic jets that force mixed fluid into the annulus. The RMS mixture fraction fluctuations show peaks on both edges of the annulus (the mixing layers) as expected. The mixing of air into the center of the annulus is shown by the increase in the fluctuations there for both kinds of forcing. This is a small-scale effect, so there is little difference between the two forcing cases. Unlike the mean profiles, however, a difference between the two forms of forcing can be seen in the outer mixing layer. Amplitude modulation has already increased the width of the mixing layer on both sides more than the continuous case. Note again the asymmetry due to the right side being directly above an actuator. The continuous forcing has much more effect above an actuator at this downstream location.

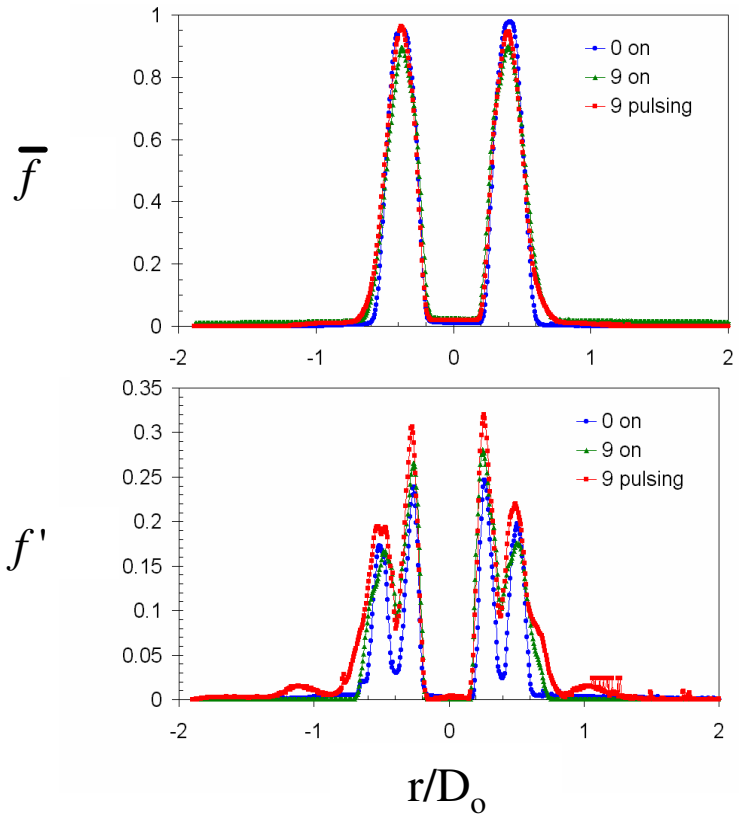

Figure 5.23. Mean and RMS mixture fraction profiles for the three actuation cases at $x/D_o = 0.25$ for the coaxial jets.

Farther downstream, at $x/D_o = 2$, the effects of actuation are more evident (Figure 5.24). The modulated forcing spreads the annular jet fluid much wider than the continuous forcing. Pulsing also mixes more air into the annulus than high frequency actuation alone, as shown by the lower peak mixture fractions in the annulus. Both methods of forcing have similar effects in the center of the flow, suggesting that small-scale structures are mostly responsible for mixing enhancement in the inner shear layer. Note that the asymmetry now favors the left side for both cases of forcing, showing that interaction between adjacent synthetic jets is an important aspect in the outer mixing

layer. The RMS mixture fraction fluctuations also show the increased width of the mixing layer caused by amplitude modulation. The right side exhibits some increase in the outer mixing layer width due to the high frequency forcing as well. Again, both cases have increased the fluctuations in the center of the annulus. Also of interest is that the 9 pulsing case has developed three peaks on each side in the RMS profile. The third peak is a direct result of the large scale structure created by the amplitude modulation. It creates a region on the outside of the structure with high fluctuations. It takes some distance downstream for this structure to develop, which explains the lack of the third peak in the previous figure. For all three cases, the location of the RMS peaks track fairly well together. The innermost peaks move to the center as mixing occurs until they blend into one central peak farther downstream. The outermost peak for 0 on moves out slightly as the jet spreads while the next peak for the actuated cases (outermost for 9 on, middle one for 9 pulsing) remains directly over the actuators as the flow travels downstream. The outer peak for the 9 pulsing case moves outward with the large structure that causes it. It is should be noted that the peaks coincide with the inflection points in the average mixture fraction profile in each mixing layer or region.

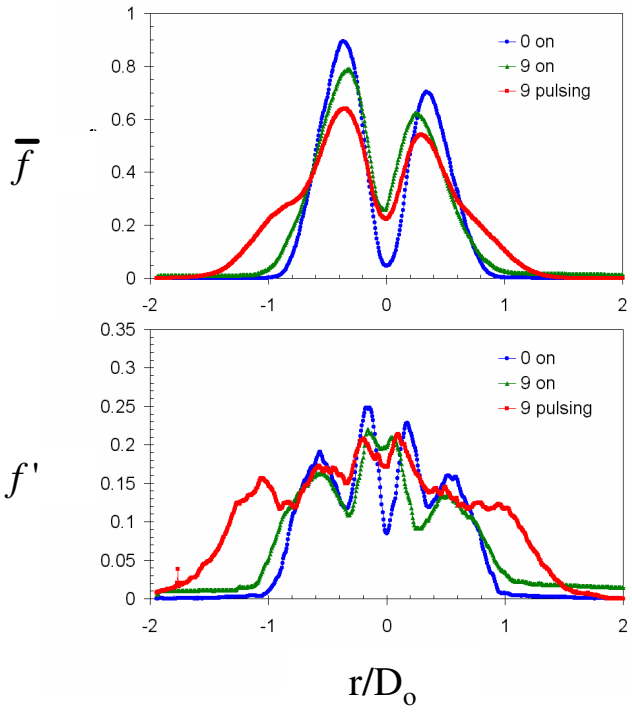

Figure 5.24. Mean and RMS mixture fraction profiles for the three actuation cases at x/D$_o$ = 2 for the coaxial jets.

Because the asymmetry of the actuation is so important to the understanding of the results, it is necessary to examine the symmetry of the average mixture fraction profiles. Figure 5.25 shows the profiles from four downstream locations for the unforced flow (the profiles are adjusted for the slight angle to the right in the flow to maintain the center at r = 0), the 9 on case and the 9 pulsing case. While there are minor differences in magnitude between the two sides for 0 on, it is clear that the profiles match almost exactly in radial location as is expected for the unforced jet. The 9 on case also shows remarkable symmetry. The right side is slightly larger in the near field, but mostly there are just small magnitude differences as with the 0 on case. The profiles are not adjusted for any possible flow angle (relative to the camera axis) since there is no way to separate

flow effects from the actuation effects. The 9 pulsing case is different from these first two cases. The flow is quite symmetric in the near field, but shows significant asymmetry downstream. The center of the profiles slowly moves to the right, but the left side extends out significantly farther than the right in the intermediate locations.

Figure 5.26 compares the pdf images for the unforced and forced cases at $x/D_o = 0.25$. The spreading of the jet is apparent even this close to the jet exit, with most of the effect in the outer mixing layer above the actuators. Still, there is a visible change in the inner mixing layer where the small-scale structures cause the mixture fraction to oscillate between very low and very high with less mixed fluid than in the unforced case (i.e., there is nearly a bimodal distribution of mixture fraction). The lower f' peaks seen in Figure 5.23 for the 9 on case in comparison to the 0 on case appear here as the outer edges of the annulus having a shallower slope for the most probable f. A vertical cut through the pdf images gives the pdf of f at the given radial position, and the shallower slope results in a slightly narrower distribution of f and thus lower f'. The greater radial width of the distribution in the inner mixing layer results in larger f' peaks in the inner mixing layer for 9 on because while the full range of f is possible over a small radial region, the most probable value jumps from low to high rather than the smoother transition in the inner mixing layer for 0 on.

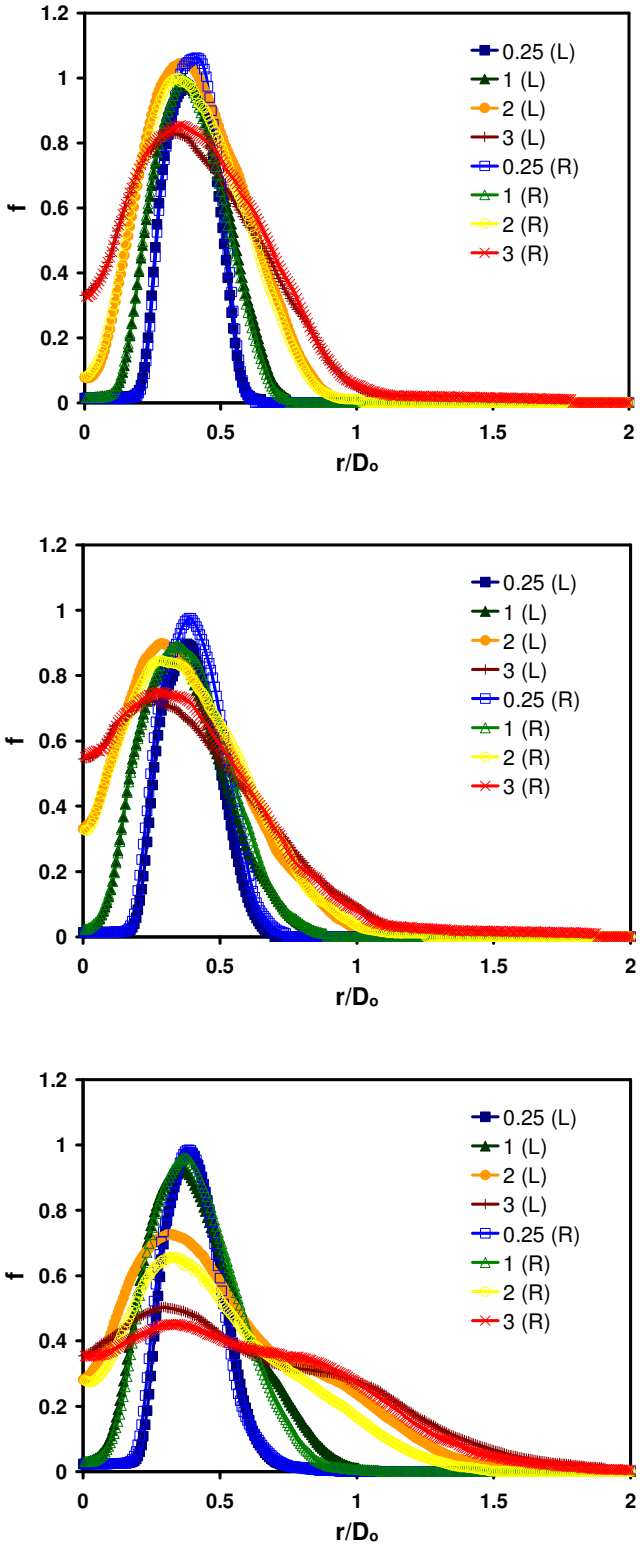

Figure 5.25. Symmetry of the mean mixture fraction profiles for the 0 on (top), 9 on (middle) and 9 pulsing (bottom) cases in coaxial jets at four downstream locations.

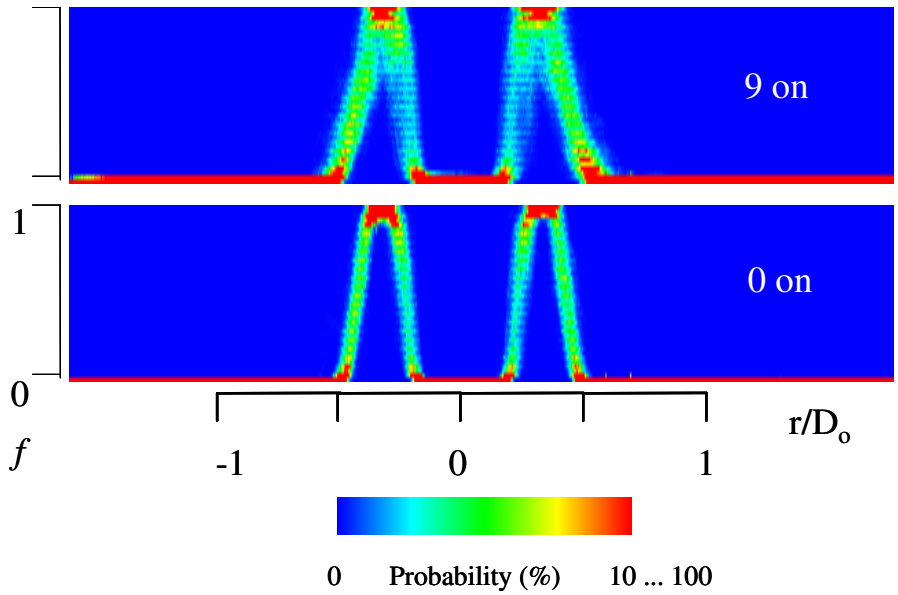

Figure 5.26. Unforced versus 9 on pdf images at $x/D_o = 0.25$ for coaxial jets.

At $x/D_o = 1.5$ (Figure 5.27), the mixing enhancement in the inner mixing layer is apparent as the forced case is starting to show acetone mixed to the center of the flow, while the unforced case still has a significant region of pure air in the center. The outer mixing layer is also broader, and the peak acetone concentrations are lower for the forced case. By $x/D_o = 2.5$ (Figure 5.27), the unforced case is finally starting to show some annular fluid mixed into the center of the flow. The forced case, in contrast, is approaching nearly uniform mixing throughout the inner region of the jet. The forced jet is still broader and has lower peak mixture fractions than the unforced case. This is clear evidence of the significant mixing enhancement generated by the actuators running at high frequency. Comparing the 9 on pdf image at $x/D_o = 1.5$ to the 0 on pdf image at $x/D_o = 2.5$, the similarities are striking. The actuators have reduced the downstream distance needed to reach the same state of mixing throughout the flow by $x/D_o = 1$. The same conclusion can be drawn from the previous results showing the jet edges and other

measures by comparing the data for the two cases. The synthetic jets have not fundamentally changed the mixing behavior of the flow, however.

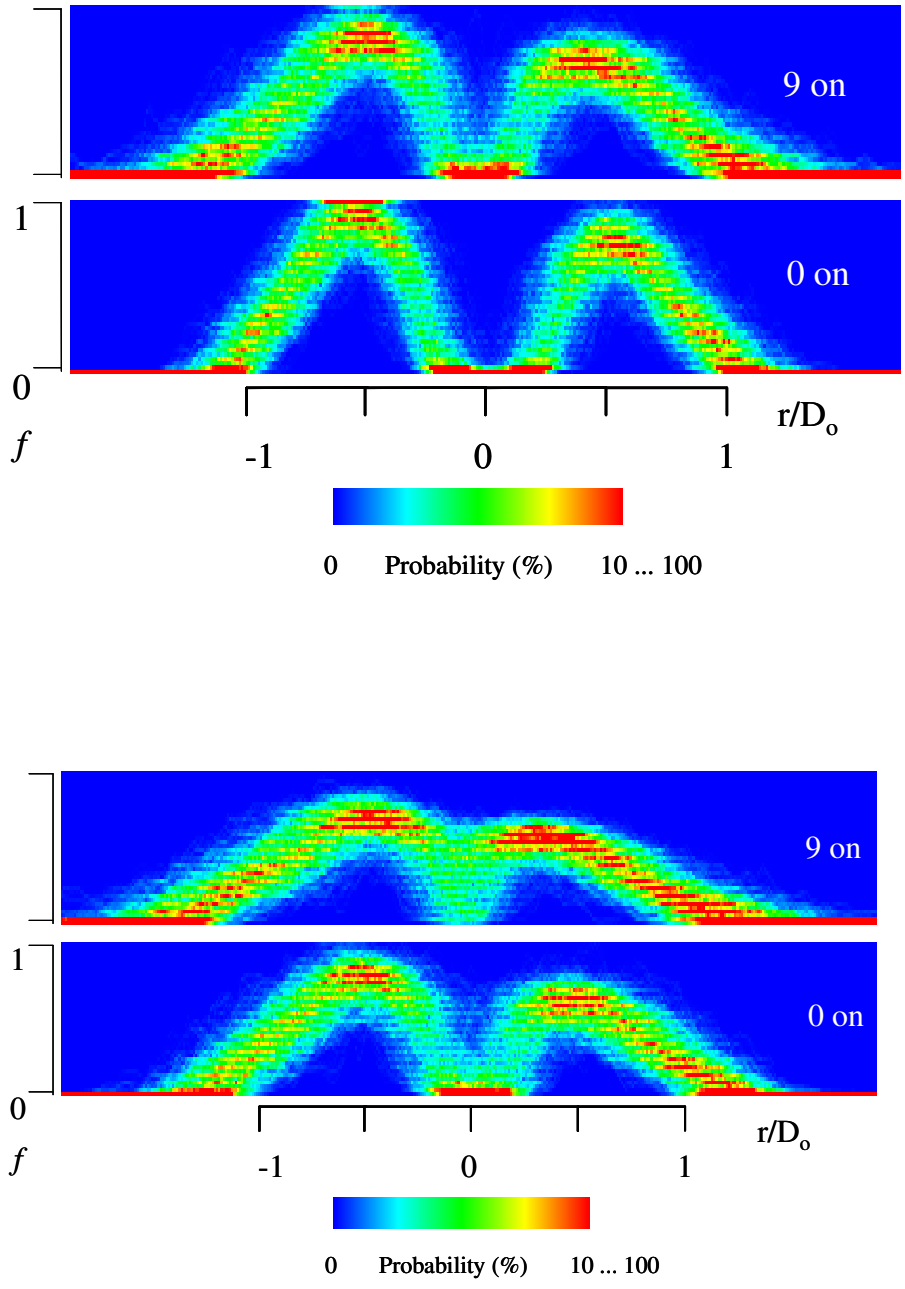

Figure 5.27. Unforced versus 9 on pdf images at x/D_o = 1.5 (top) and 2.5 (bottom) for coaxial jets.

Figure 5.12 showed how the large structures visible in the PLIF images correspond to the velocity structures measured in the companion effort. The large-scale structures are also evident in the PDF results (Figure 5.28). The large-scale structures create large regions of fairly uniformly mixed fluid that vastly increase the jet width and reduce variations in the spatial mixture fraction distribution. Comparing the phase before the cycle begins (330°) and the phase just after the actuation begins (10°) shows several things. At $x/D_o = 0.25$, the mixed regions and flow field broadening generated by the actuators are obvious. Slight differences exist in the shape of the acetone distributions at $x/D_o = 0.5$ as well, due to the synthetic jets pulling in fluid and making the outer mixing layer more quickly transition from 0 to 1. The remnants of the previous large-scale structure can be seen farther downstream with the broad regions of uniformly mixed fluid. At $x/D_o = 2.5$, the inner edge of the large structure is dipping to a lower f at 10° than at 330°. This matches well with the images of the phases shown previously (Figure 5.11), with the decrease caused by the large structure passing by so the bottom side is caught in this slice. This results in an area between the large structure and the rest of the jet that contains less acetone. Comparing various pdf images, a propagation velocity of 3.4 m/s was calculated for the large structure in the coaxial jets. This is roughly the velocity of the flow at $r/D_o = 0.5$ (Figure 3.7), just as was the case for the single jet.

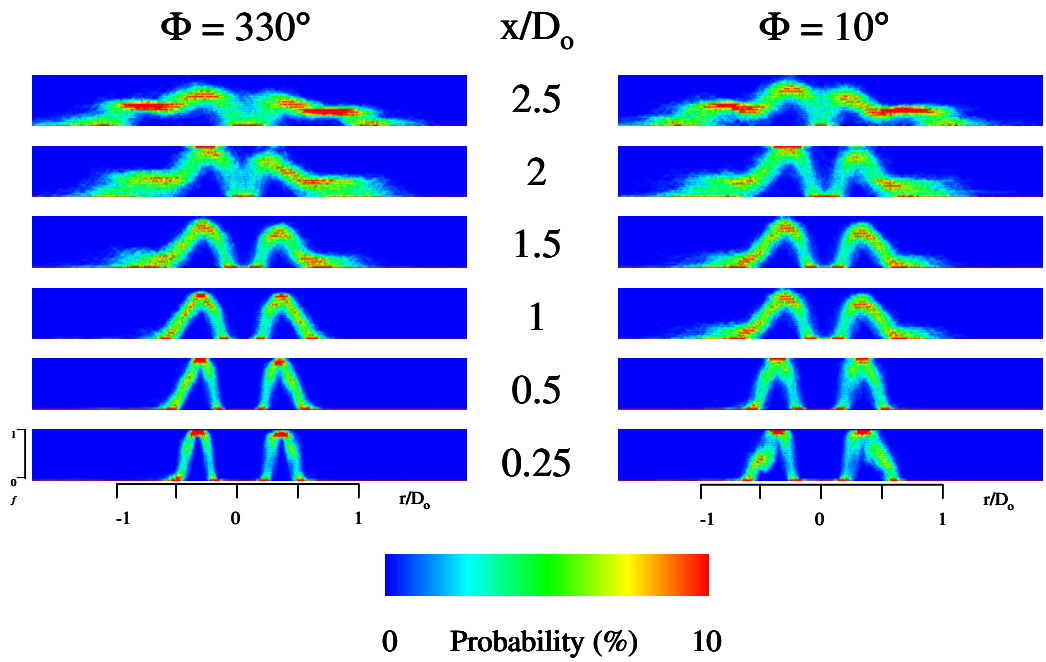

Figure 5.28. Two phases of pdf images at different downstream locations in the coaxial jets.

Another piece of information available from the pdf images is the radial distribution of probability of finding fluid mixed to a given mixture fraction, as mentioned previously. This provides information important for combustors such as the width of the stoichiometric mixture fraction distribution, where combustion will occur. Because the probability is calculated for f at a given r in the pdf images, the radial distributions do not sum to a total of 1. Figure 5.29 shows these distributions at x/D_o = 1.75 for three different mixture fractions (0.25, 0.50, 0.75) for all three actuation cases. It is clear that the high frequency forcing has significantly enhanced the mixing of air into the annulus from comparing the f = 0.75 distributions for 0 on and 9 on. The f = 0.50 distributions are very similar for the two cases, but the f = 0.25 distributions show the extra width of the partially mixed flow caused by the synthetic jets. In addition, the centerline value

never reaches zero on average in the 9 on case while it did in the 0 on case. The same result was seen in the centerline mixture fraction data (Figure 5.20). The much greater width of the mixed flow due to the large structure created by amplitude modulation is apparent in all three distributions for the pulsing case. The noise in the distributions is much lower due to the phase averaging over nine phases.

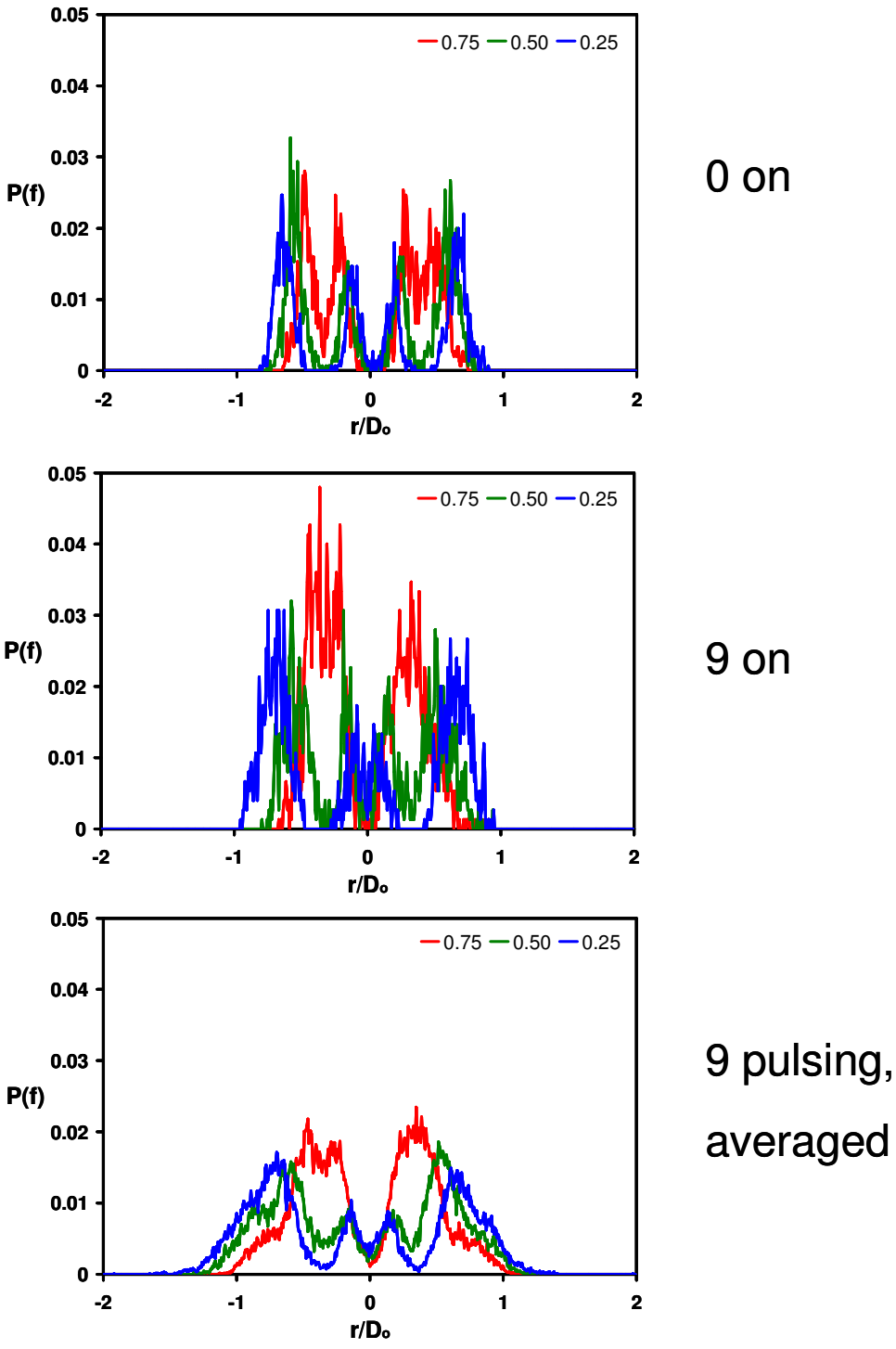

Figure 5.29. Radial distributions of the probability of finding fluid of the given mixture fraction at a given radial location for $x/D_o = 1.75$.

Velocity Ratios

All the results presented so far have been for a velocity ratio of $U_i/U_o = 0.62$, but two other velocity ratios were also studied (0.30 and 1.4) with total momentum of the coaxial jets held constant between the cases. The three velocity ratios represent two different flow regimes. When $U_i/U_o = 1.4$, the coaxial jets act much like a single jet flow. The inner shear layer is very weak and the center jet is quite strong. The case of $U_i/U_o = 0.30$ is the opposite extreme. This flow is quite similar to a wake flow due to the strong annular flow and the weak center jet. The previously presented case, $U_i/U_o = 0.62$, is a balance between the two and received the most study.

The unforced flow fields can be seen in Figure 5.30. Each figure contains two qualitative, instantaneous images (taken at different times) combined to show the flow field from $x/D_o = 0$ to 5 for both the unforced and the forced flow. The images were acquired from two vertical locations, or "windows." In the first window, the bottom of the sheet grazed the top of the metal body. The flow facility was lowered to produce a second window with the bottom of the sheet at $x/D_o = 2$. This allowed imaging up to $x/D_o = 5$ with significant overlap between the two windows. Although the two sets of images were not taken simultaneously and cannot be compared on an instantaneous basis, the overlap allowed for the images to be combined on an averaged or statistical basis. The rapid mixing of acetone to the centerline is clear evidence of the wake-like flow for the 0.30 ratio. The other two cases look more similar, although the pure acetone disappears sooner for the jet flow of the 1.4 ratio.

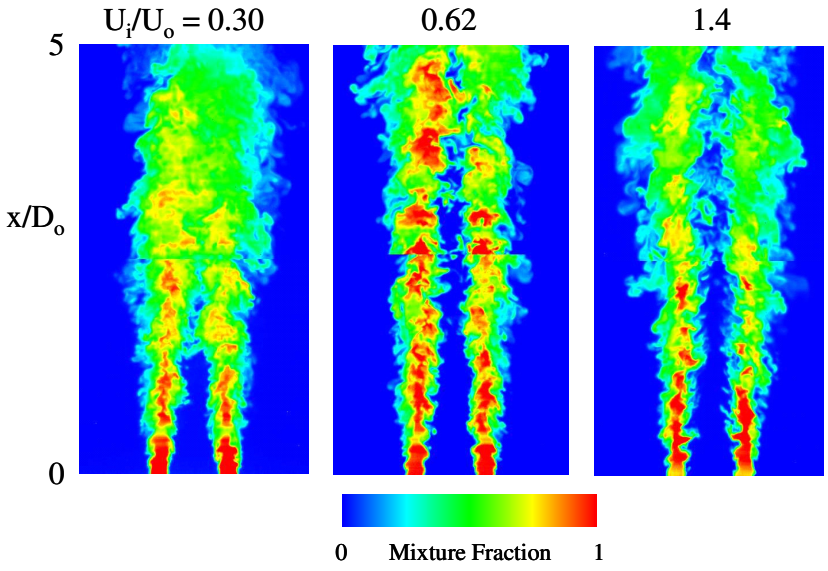

Figure 5.30. Side views of unforced coaxial jets with three different velocity ratios (0.30, 0.62, 1.4) for x/D_o = 0-5.

The effects of high frequency forcing on different velocity ratios between coaxial jets can be seen qualitatively in Figure 5.31. In all three cases, small-scale structures can be seen starting at the jet exit when the synthetic jets are running. These structures decay with downstream distance. Annular fluid is mixed into the central jet more quickly by the actuators, significantly reducing the downstream distance before no pure air is left in the center. There are also more structures in the outer mixing layer when the actuators are running. When U_i/U_o = 1.4, the high frequency forcing creates only limited enhancement of the mixing. The actuators do force the annulus to pinch off the center jet quicker, though. The actuators again hasten the mixing of annular fluid into the center jet for the case of U_i/U_o = 0.30, even though the natural mixing due to the wake-like flow is quite strong already. The third case, U_i/U_o = 0.62, is the most interesting. The synthetic jets cause a significant increase in the mixing of annular fluid into the center of the flow. They also enhance the mixing in the outer mixing layer, increasing the jet spreading. By

virtue of the balance between inner shear layer strength and annular velocity, this case allows for greater mixing enhancement in both mixing layers.

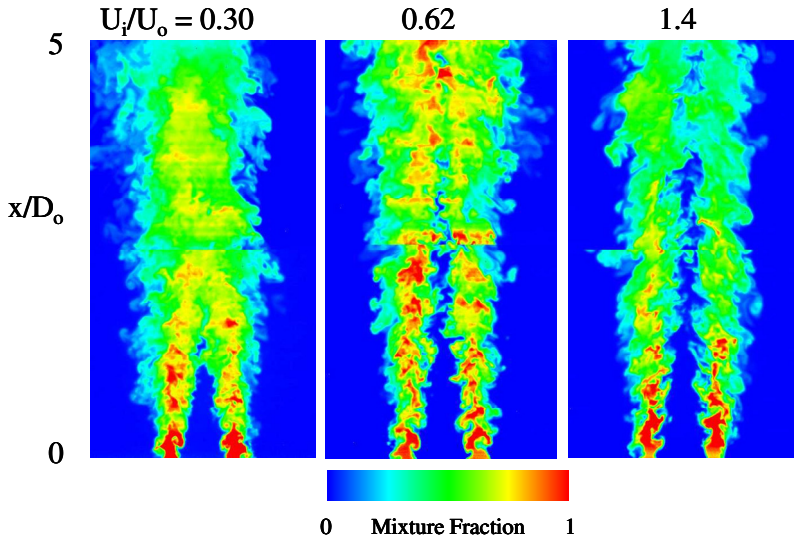

Figure 5.31. Side views of 9 on actuation in coaxial jets with three different velocity ratios (0.30, 0.62, 1.4) for x/D_o = 0-5.

While the 0.62 case may be the most interesting for high frequency actuation, the amplitude modulation is effective for all three velocity ratios. Nine equally spaced phases of amplitude modulation for U_i/U_o = 0.30 and 1.4 are seen in Figure 5.32 and Figure 5.33 respectively. Figure 5.32 shows that the higher velocity in the annulus reduces the effectiveness of the synthetic jets in creating large scale structures that enhance mixing by spreading the jet. The structures still have a large effect on the center flow, though.

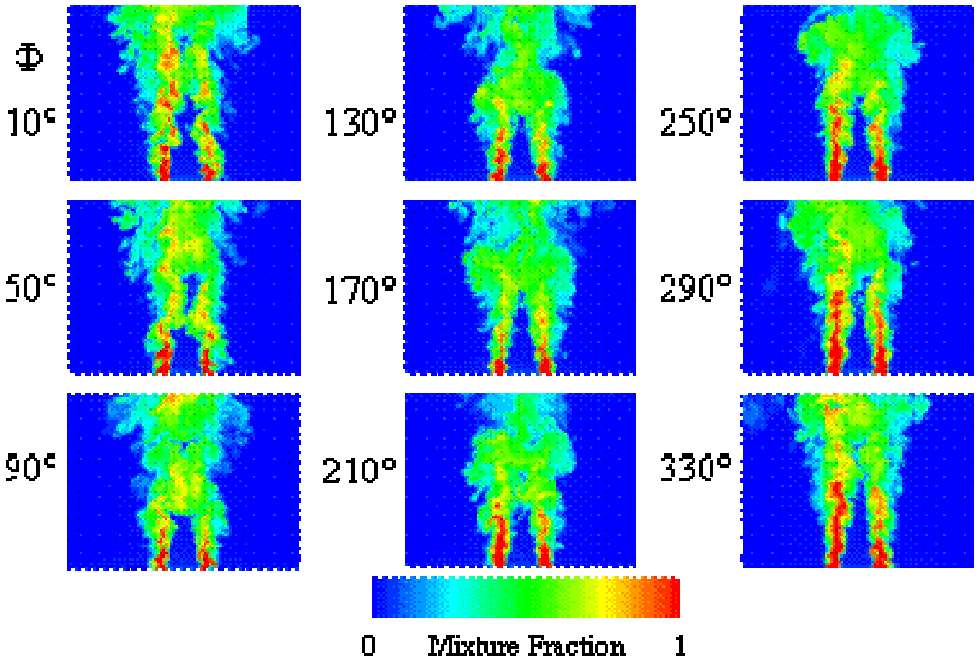

Figure 5.32. Representative images for the nine phases of 9-pulsing actuation in the coaxial jets with $U_i/U_o = 0.30$.

The reverse is true for the jet flow case (Figure 5.33). The high velocity in the center jet and the weakness of the inner shear layer cause the large structures to mostly effect the outer mixing layer. Note that the structures are not as prominent in this case as for the wake flows because the flow naturally wants to spread instead of the synthetic jets opposing the natural radial motion of the annular fluid. The net result of comparing these cases is to determine that the synthetic jet actuators work best with the wake flow of the 0.30 velocity ratio. There are two strong shear layers for actuators to affect. Clearly these conditions are necessary for the synthetic jets to maximize their effects on the flow.

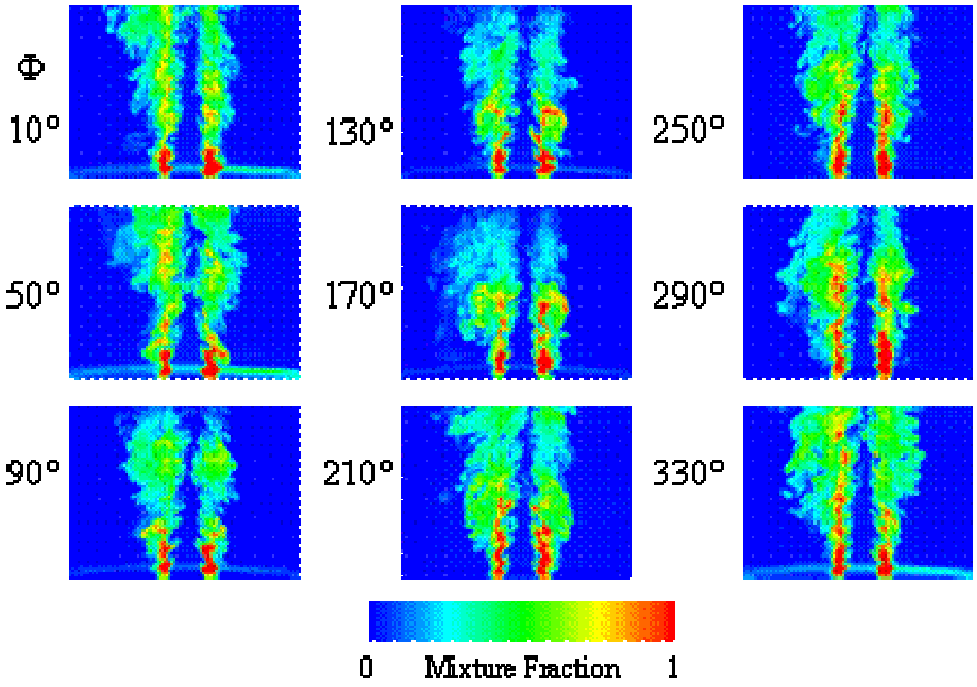

Figure 5.33. Representative images for the nine phases of 9-pulsing actuation in the coaxial jets with U_i/U_o = 1.4.

It is helpful to use some of the same statistics shown previously to compare the three velocity ratios. Figure 5.34 shows a comparison of the outer mixing layer widths on each side of the unforced jet for all three velocity ratios. Despite differences in the annular jet velocity (14, 13 and 10 m/s for U_i/U_o = 0.30, 0.62 and 1.4 respectively), and thus in the outer shear layer, the outer mixing layer widths are virtually identical for all three cases. Switching to 9 on actuation (Figure 5.35), the flows become distinct. The outer mixing layer width scales inversely with the velocity ratio. This is due to the middle of the annulus being moved towards the middle in the wake-like flows as seen in the images. The synthetic jets keep the outer edge of the jet more constrained, resulting in a net increase in outer mixing layer width as the center flow becomes weaker. In addition, the left side is wider than the right side for all three ratios showing that the asymmetrical

actuation has similar effects for a variety of cases. The difference is greatest for the jet-like flow which has the slowest annular jet, increasing the power of the actuators relative to the annular flow. The pulsing cases (Figure 5.36) show different trends. The width is dependent on the strength of the annulus, with the relatively weak annulus in the jet-like flow having the greatest mixing layer width while the most wake-like of the flows has the thinnest layer. Farther downstream, though, the large-scale structures in the jet-like flow lose their effectiveness while the most wake-like flow grows in effectiveness. The asymmetry is very pronounced in all of the 9 pulsing cases, but especially in the jet-like flow. Both of the results stem from the natural width of the flows. Since the jet-like flow is already wide, the 9 pulsing is less effective at driving the acetone even farther out while the other extreme starts with a very narrow flow that is much more readily moved farther out.

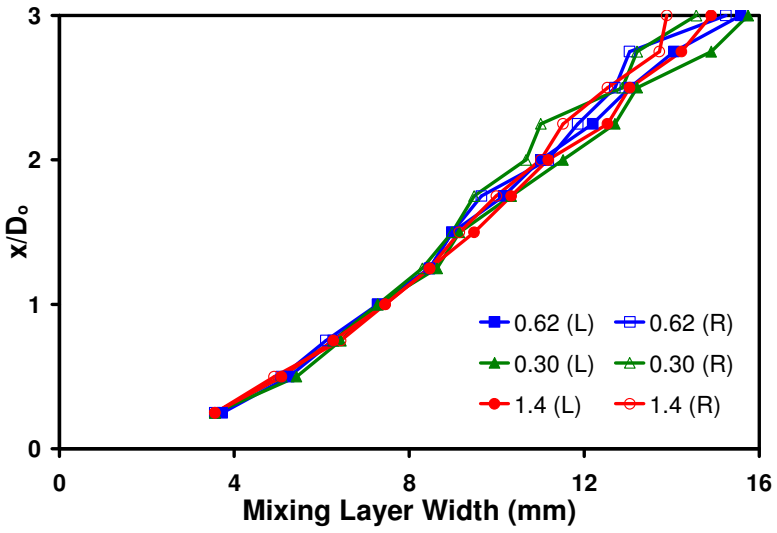

Figure 5.34. Outer mixing layer widths on the right and left sides of the unforced coaxial jets for each velocity ratio (U_i/U_o = 0.30, 0.62, 1.4).

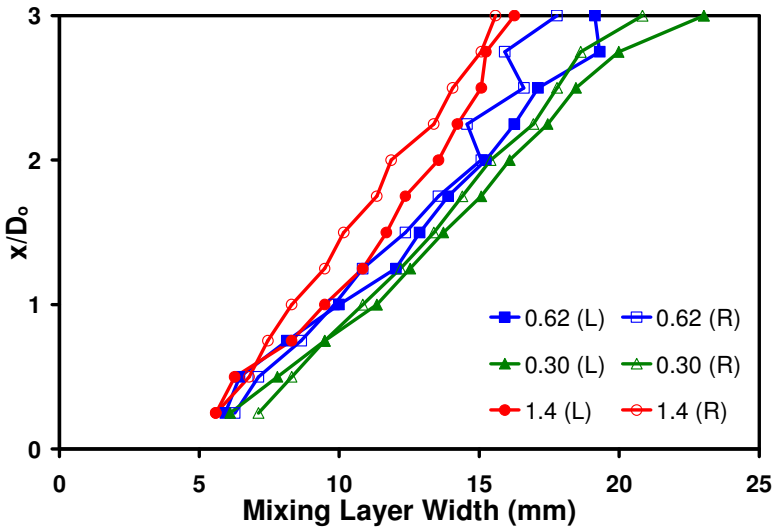

Figure 5.35. Outer mixing layer widths on the right and left sides of the coaxial jets with 9 on actuation for each velocity ratio (U_i/U_o = 0.30, 0.62, 1.4).

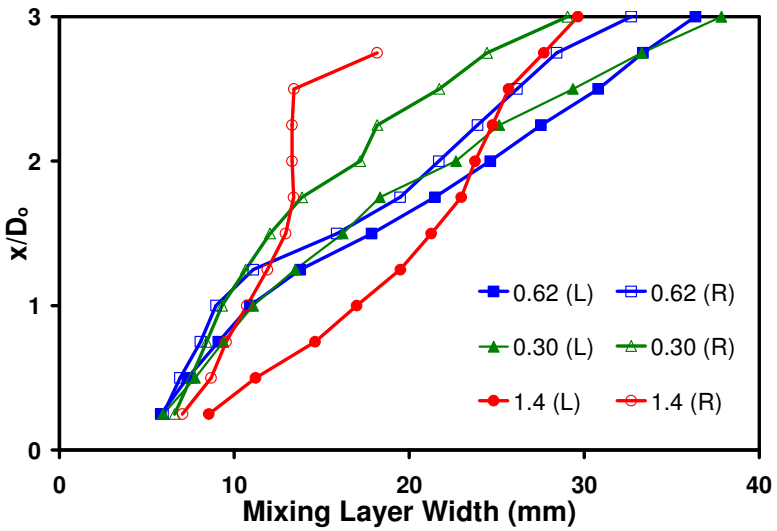

Figure 5.36. Outer mixing layer widths on the right and left sides of the coaxial jets with 9 pulsing actuation (phase averaged) for each velocity ratio (U_i/U_o = 0.30, 0.62, 1.4).

In general, the statistics follow similar trends for the other ratios as they did for U_i/U_o = 0.62 allowing for the inherent differences in the flows. Rather than repeat a series of

similar results, only one significant difference needs to be discussed. Figure 5.37 shows the inner mixing layer widths for the three actuation cases in the jet-like flow. The 9 pulsing case sharing the same average inner mixing layer width with 9 on is the same result seen before. Unlike the previous case presented, however, there is very little difference between the left and right sides for the 9 on actuation. The extreme wake-like flow also showed little difference between the sides with both actuation cases having similar values. The clear conclusion is that the small-scales created by the high frequency actuation are responsible for the enhanced mixing in the inner mixing layers, not the large-scale structures. Clearly the large-scale structures influence the inner flow and move acetone around, but they only significantly enhance the mixing on the outside of the flows.

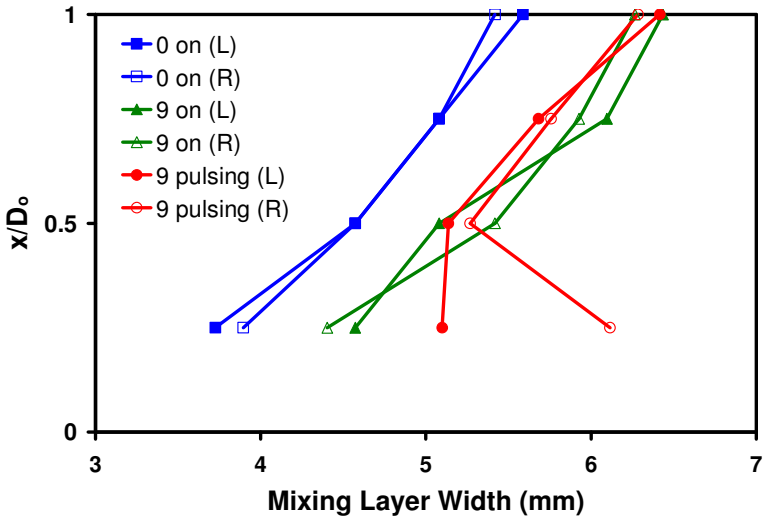

Figure 5.37. Inner mixing layer widths for the three actuation cases in the coaxial jets with $U_i/U_o = 1.4$.

CHAPTER 6

LIQUID MEASUREMENTS

Acetone PLIF has proven to be a useful tool for mixing measurements in gaseous flows. However, liquid fuels are of great interest and simultaneous droplet sizing and mixing measurements in two-phase flows are needed. Based on the previous quantitative results, it was decided to determine what additional knowledge is needed to extend quantitative acetone PLIF into two-phase flows. While acetone PLIF has been used for visualization and threshold sizing (Is it bigger than a certain size?) of acetone droplets before, it was never made truly quantitative. The previous results for acetone vapor concentration in two-phase flows[49] were not able to handle regions in the laser shadow of a droplet. This chapter presents preliminary results in a two-phase flow produced by a novel atomizer. To enable further development of the technique, a model of acetone droplet fluorescence was developed (and presented in Chapter 2). Results and implications of this model for quantitative acetone measurements in two-phase flows are presented here. Finally, experimental results of acetone vapor and droplet measurements in a simple spray are presented and discussed in terms of the remaining unknown values necessary for this technique to work in two-phase flows.

Preliminary Spray Measurements

Acetone fluorescence images were acquired in an evaporating, two-phase flowfield to investigate the utility of the technique and the ability to distinguish vapor and liquid phases. For these preliminary tests, a flowfield with a dilute spray and without a large number of big droplets was advantageous. An excellent opportunity to investigate such a flowfield occurred when MicroCoating Technologies asked for some qualitative measurements of the flowfield generated by their Nanomiser® spray system for a range of air and liquid flow rates. This system is proprietary, so the results and operating conditions presented have been normalized. The atomizer is supposed to be able to control droplet size by adjusting the block temperature of the atomizer. The first goal was simply to acquire images of a two-phase flowfield to prove that liquid acetone fluorescence does occur and is of a reasonable strength to be imaged. If the signal is much stronger than expected, the dynamic range limitations of cameras would result in an inability to also measure low concentrations of acetone vapor. If the signal was much weaker than anticipated, the droplets would have to be very large to register which would defeat the practical application of this technique for many flowfields.

Figure 6.1 shows three flow field images acquired for the same air and acetone flow rates but three different atomizer temperatures. The images cover a three inch tall region, are uncorrected except for background subtraction, and begin one inch downstream of the atomizer exit due to physical constraints. Because the amount of acetone in each image is so small, absorption corrections are not needed. A sheet correction would be necessary to make quantitative comparisons at different heights, but qualitative visualization was

the primary goal of this investigation. At temperature T, individual droplets can be distinguished from the vapor as distinct points in the image; these droplets are seen throughout the flow. A small increase in temperature greatly reduces the number of droplets, but a few still exist at T + 20°. A further increase of just 10° eliminates the obvious droplets, yielding a flow that could either be vapor only or vapor and very small droplets. This transition temperature is important for spray coating applications, where it is desirable to minimize the energy used to heat the system but droplets cannot be allowed to touch the object being coated.

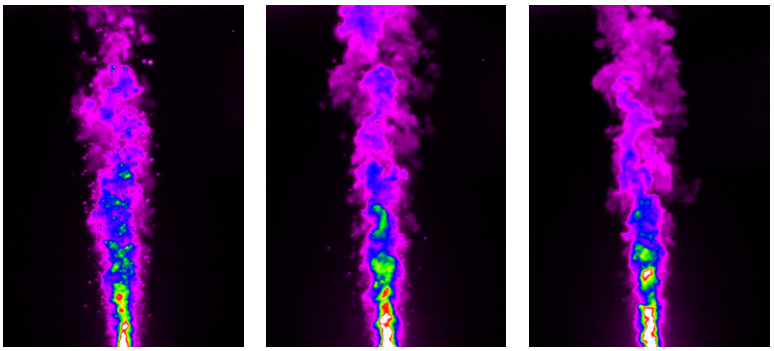

Figure 6.1. Nanomiser® flowfield images for three different temperatures.

The matrix of test conditions of this system included several conditions where a range of temperatures where used for the same flow rates. MicroCoating Technologies predicted that this transition temperature would change with the liquid (acetone in this case) flow rate. Higher liquid flow rates result in a shorter time in the heated block and thus a lower liquid temperature at the exit. As seen in Figure 6.2, however, the transition temperature appears to be correlated to the ratio of the liquid and air flow rates, at least

for the range covered here (1−1.5). The dependence is essentially linear over this small range. An explanation for this dependence is that it is the amount of hot air interacting with the acetone after the exit that is the determining factor in evaporation and not the acetone temperature itself. Obviously this curve cannot continue to grow forever, but it would take more extensive modeling and study to indicate when the absolute flow rates would become more important than the ratio of flow rates and that is beyond the scope of this research.

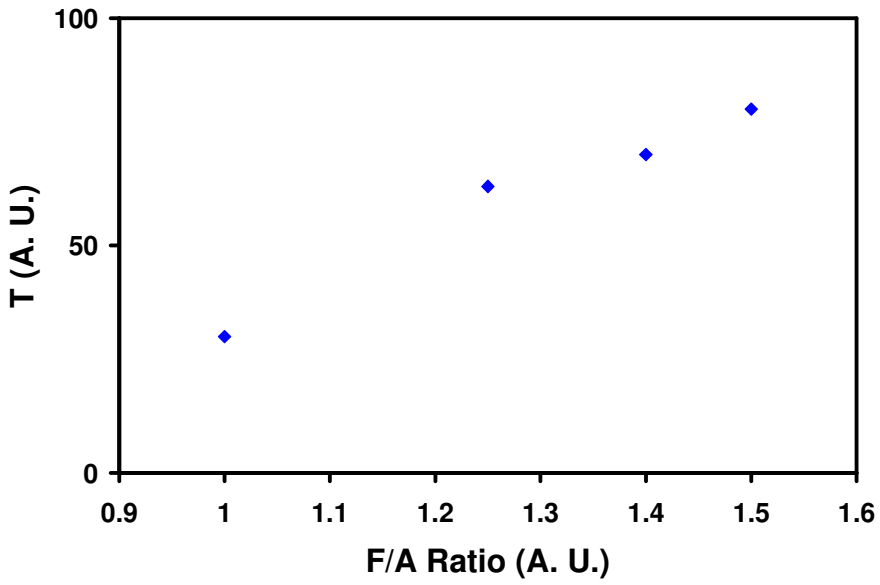

Figure 6.2. Transition temperature versus the ratio of acetone to air flow rates for the Nanomiser®.

Due to the limited scope of this research, quantitative droplet sizing and mixing measurements were not performed. This research clearly showed the technique can measure distinct pixels of higher signal against a background of acetone vapor in a flow field where small acetone droplets are expected. This lends hope to the goal of making

quantitative mixing measurements in a two-phase flowfield along with droplet sizing. This investigation also highlights the need to distinguish whether acetone fluorescence emanates from droplets or vapor, preferably from just the signal level measured by the camera. For this technique to be practical, the cutoff diameter below which the signal level alone cannot discriminate between phases needs to sufficiently low to be useful. Before running experiments, the first step is to develop a model of droplet fluorescence and provide an estimate of this cutoff value.

Droplet Model Results

The droplet model used here is fairly simple and intended to provide first order estimates of the expected fluorescence for a dilute spray of spherical droplets. The model (presented in Chapter 2), includes several variables that merit discussion. Before delving into the variables, though, it is useful to look at some typical results of the model. Figure 6.3 presents the amount of fluorescence expected from a droplet of a given diameter or a cubical pixel filled with a uniform concentration of acetone vapor. The vapor signal (S_v) grows linearly as the size increase since it is directly related to the number of acetone molecules present in the pixel. Laser absorption is insignificant due to the sizes considered here, so there is no deviation from linear growth. The vapor mole fraction represented in the figure is for saturated acetone vapor at room temperature and pressure. The liquid signal (S_d) can be represented by two limiting curves. For small droplets ($d < 10$ μm), the signal scales like d^3. This is due to the amount of laser absorption being very small over the short path lengths through the liquid acetone that these small droplets

represent. The strong absorption by acetone quickly becomes apparent as the diameter grows, with $d^{1.57}$ growth being the result for large droplets. This is due to the droplets becoming area absorbers instead of volume absorbers as the laser light is rapidly absorbed as it passes through the larger drops.

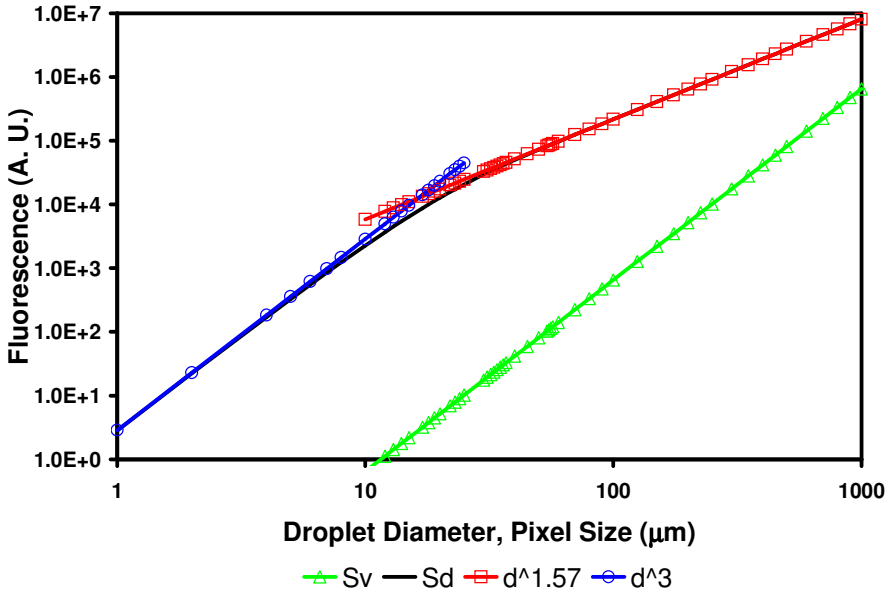

Figure 6.3. Fluorescence signal versus droplet diameter and pixel size.

From the signal curves for the two phases, it is possible to calculate the pixel size that will yield a fluorescence signal equivalent to a droplet of a given diameter (denoted the *equivalent pixel size*) or vice versa. Equivalent pixel size represents the droplet diameter beyond which signal strength alone is not sufficient to determine whether or not there is a droplet present in a given pixel. Therefore, equivalent pixel size is a useful number for planning experiments. If droplets down to a certain diameter must be measured, it provides the required camera resolution and laser sheet thickness. If the imaging system is the limiting factor, it provides a measure of what droplet sizes can be clearly delineated

as distinct from vapor. Figure 6.4 shows the equivalent pixel size for the same conditions as covered in Figure 6.3. Assuming the same imaging system as used for the jet mixing work (EPS = 170 μm), the model predicts a droplet cutoff of approximately 20 μm.

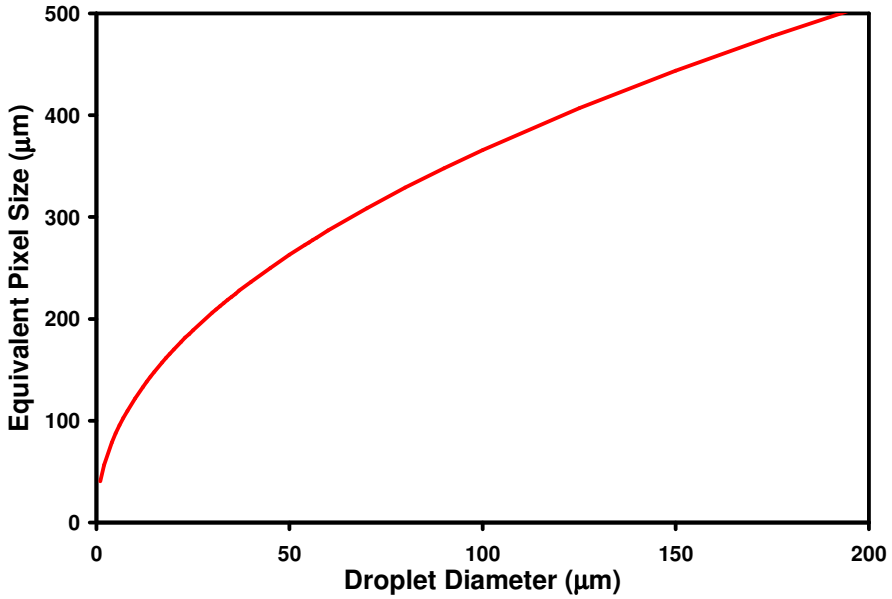

Figure 6.4. Equivalent pixel size versus droplet diameter.

The equivalent pixel size is highly dependent on the vapor mole fraction used to model the vapor signal, of course. The previous results assumed saturated vapor, which is a worst case for standard conditions. Results for a range of mole fractions are compared in Figure 6.5. It is impossible to obtain a mole fraction of 1 (i.e., pure acetone vapor) for standard conditions, but it is provided for the sake of comparison. Saturation provides $\chi = 0.3$, while $\chi = 0.525$ represents a stoichiometric mixture of acetone and air. Clearly, lower mole fractions result in smaller droplet cutoffs. For the same EPS of 170 μm, the cutoff drops to 10 μm and 7 μm for mole fractions of 0.1 and 0.0525 respectively.

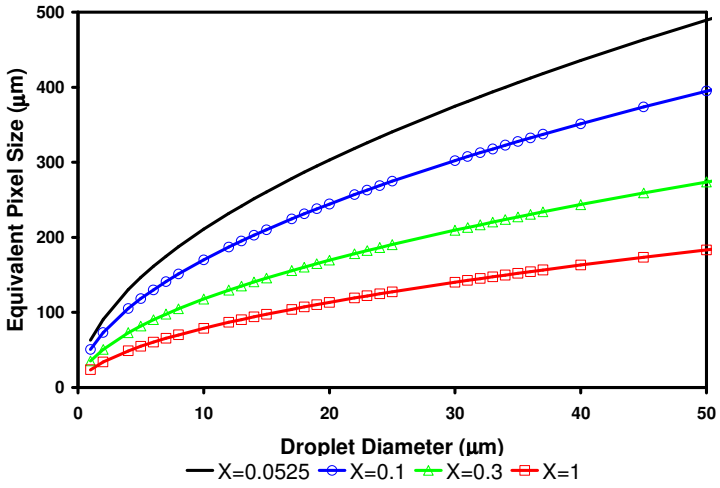

Figure 6.5. Equivalent pixel size versus the cutoff droplet diameter for a range of vapor mole fractions.

Dilute Spray Measurements

The Nanomiser® provided an excellent opportunity to test the basics of liquid acetone fluorescence, but it did not push the technique to provide quantitative results. Feeling that a reasonable estimate for liquid acetone fluorescence was possible, it was time to begin applying this new technique. In order to develop the technique, a research spray facility was constructed. The spray facility, described earlier, reused the coaxial jet setup with a water nozzle inserted inside the center tube. Cross-sectional images of the spray were acquired to provide an understanding of the spray and evaluate the application of acetone PLIF to the spray.

There are several important considerations for this technique and comparisons to the model. The model assumes there is only one droplet per pixel and that the droplet is contained entirely in that pixel. The technique is also dependent on not having large amounts of liquid acetone in the laser path or the absorption will become too strong to provide further information. A dilute spray will satisfy most of these conditions, but there may be times when a droplet is split by pixel boundaries or when multiple small droplets exist in very close proximity. The first requirement, then, is to acquire images of the spray to determine if it is dilute enough to apply this technique.

Figure 6.6 shows spray cross-sections at 1" and 10" downstream of the nozzle exit. The distinct spots due to large numbers of droplets at 1" are readily apparent. The lack of acetone vapor at 1" is also obvious. There are larger droplets around the perimeter with a limited number of smaller droplets in the middle. By 10" downstream, many of the droplets have evaporated resulting in a large amount of acetone vapor with a few droplets. The droplets still are apparent on a background of acetone vapor, implying this spray is also a good candidate for applying liquid acetone fluorescence.

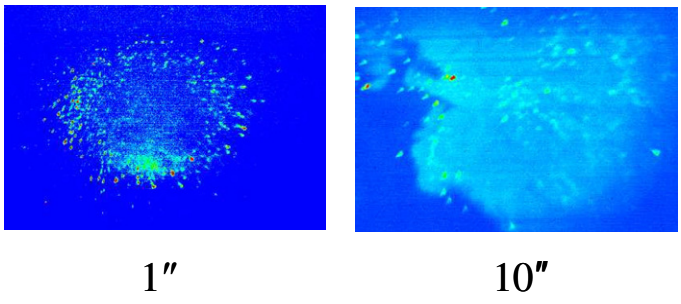

Figure 6.6. Spray cross-section at 1 and 10 inches downstream.

An initial attempt to correct the image at 10" shows the potential of the technique. A single row of the correction is shown in Figure 6.7. The evaporating acetone has created a broad region of uniform acetone vapor. Two distinct droplets are indicated by their high signal levels, above the maximum vapor signal possible. However, closer examination of the data raised some concerns. One issue can be seen in the row plots. Notice that the droplets appear to be multiple pixels wide. This means either the droplets are on the order of 1 mm in diameter and are being spatially resolved, or the signal from a droplet is being spread over multiple pixels. The signal over the range of pixels, minus the background vapor level, was summed for each peak in an attempt to size the droplets. From the vapor measurements, the correlation between vapor signal and concentration was known. Taking the modeled signal value for saturated vapor at room temperature and the corresponding droplet diameter to generate the same signal, the ratio of each droplets signal to this cutoff signal were calculated. Given the experimental conditions, initial sizing estimates of 40 and 70 μm resulted from the model.

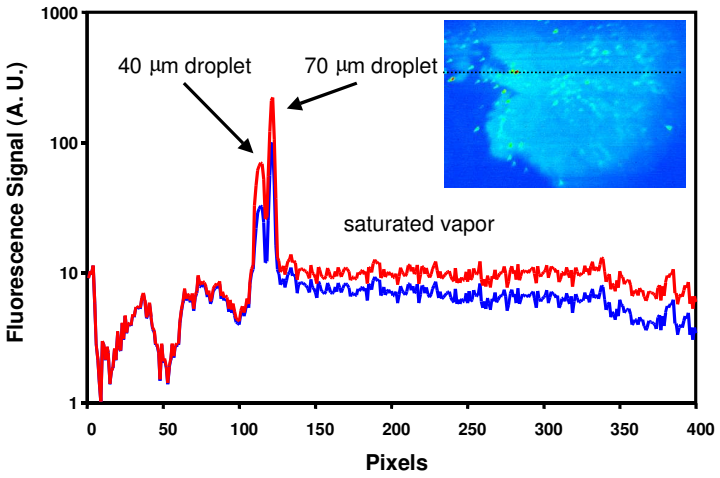

Figure 6.7. Corrected acetone fluorescence signal for a single row from the image acquired at 10" downstream (inset).

The image provides more evidence of droplets being spread over several pixels. The droplets look like streaks with a large ball and a tail. Figure 6.8 zooms in on a small region of the 10" image and shows the signal value of each pixel along two of the streaks. The heads of the streaks seem to be five pixels in diameter with an attached tail. The camera resolution was measured using a standard resolution target and it was found that a region of high contrast in signal would expand to a full width at half of the maximum value of five pixels. This agrees with the images, indicating there really should be one bright pixel with a much larger signal and a tail that is also one pixel wide. This width effect is easily accounted for during image analysis to generate the droplet size estimates, and done for the estimates given above yields droplet diameters of 95 μm for both droplets.

The tails are another matter, though. They extend in the direction of motion of the droplets (based on PDPA measurements, and indicated by arrows in the image), indicating they are motion streaks of some sort. The droplets have a larger axial than radial velocity based on the PDPA measurements, so the streaks are only indicating one component of the velocity. The difficulty is that acetone fluorescence has such a short lifetime (<2 ns) that no motion of the droplets should be observable. In order to capture motion, the signal needs to be relatively long-lived.

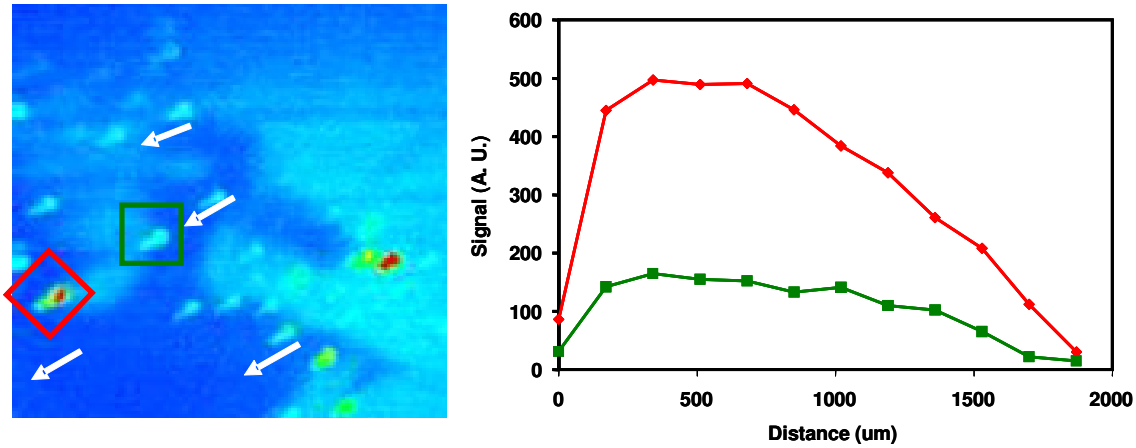

Figure 6.8. Zoomed in region of the 10" spray image along with plots of the signal through two of the streaks.

Liquid Acetone Properties

The presence of streaks in the spray images requires a rethinking of the emissions from the flowfield. Acetone can both fluoresce and phosphoresce, and phosphorescence has a much longer lifetime in vapor (200 μs) than fluorescence (2 ns). The gaseous measurements in the previous chapters represented only acetone fluorescence, because even small amounts of O_2 strongly quench acetone phosphorescence. In order to have acetone phosphorescence, there must be a lack of O_2 at that location. For these initial images, a N_2 bottle was used to pressurize the liquid acetone. However, when air was used to pressurize the liquid acetone that flowed through the atomizer, the streaks no longer occurred. Since some of the pressurizing gas can dissolve into the acetone in the supply tank, having N_2 in solution in the liquid acetone instead of O_2 was sufficient to prevent O_2 quenching of phosphorescence.

Acetone Photophysics

The first question to be addressed is whether the phosphorescence is from vapor, liquid or both. Wherever acetone vapor exists, there will be some air as well since pure vapor cannot exist at atmospheric conditions. The presence of even small amounts of air should quench any vapor phosphorescence since the O_2 quenching is so strong. It would take a tremendous amount of outgassing of dissolved N_2 from the liquid acetone to prevent air from being present, so the logical consequence is that it is the liquid acetone that is phosphorescing.

Despite many years of research into acetone photophysics[69-74,77-80], many things necessary to understanding the phosphorescence in the spray images are not known. While the fluorescence lifetimes for both vapor and liquid are well known, the liquid phosphorescence lifetime is not, especially for atmospheric conditions and with 266 nm excitation. Some measurements were performed with degassed acetone in a near-vacuum with longer wavelength excitation, but acetone luminescence is dependent on excitation wavelength and pressure (among other things) so this value is of limited use. In any case, the result was that the lifetime was found to be much shorter (30 μs)[79,80] than for vapor (200 μs). Measurements taken after the completion of this spray work,[81,82] found a lifetime around 1 μs for bulk liquid acetone when purged with N_2. This lifetime is dependent on the length of time the acetone is purged with N_2 and does not take into account spray effects, but agrees in general with all other values in the literature that liquid acetone phosphorescence is significantly shorter-lived than vapor

phosphorescence. Presumably, this is caused by the greater collisional quenching rate inherent in a liquid. Acetone vapor shows this trend as pressure increases.

Another unknown important for this work is the ratio of phosphorescence to fluorescence for liquid acetone. The ratio is nine for acetone vapor in the absence of O_2. It is difficult to know exactly what to expect of the phosphorescence yield, but the same processes that shorten the phosphorescence lifetime should also cause the phosphorescence yield to decrease. The difficulty here is that the fluorescence yield for liquid acetone is also unknown and dependent on many experimental conditions. The only value in the literature[72] is for different conditions, but found a value of 0.14% which is similar to the vapor value of 0.2%. The liquid fluorescence yield obviously affects the ratio of phosphorescence to fluorescence for the liquid as well as the ratio of liquid to vapor fluorescence. Without knowing both of these values, it is impossible to accurately model the signal expected from an acetone droplet. However, it is possible to evaluate the sensitivity of the model to a range of values for these unknowns. Figure 6.9 is a comparison of the equivalent pixel size for a range of liquid phosphorescence to fluorescence ratios, assuming a mixture fraction of 0.3 for the vapor. It is clear that phosphorescence could be very important in enabling the technique to resolve very small droplets. With P/F = 9, the droplet cutoff reduces from 20 μm to 4 μm for the experimental pixel size of 170 μm. Unfortunately, the most recent measurement in the literature[82] suggests a value of P/F = 0.012 for liquid acetone, which would not reduce equivalent pixel size appreciably. Similar results are obtained from changing the fluorescence ratio, as seen in Figure 6.10. The phosphorescence to fluorescence ratio is assumed to be 3 for all the curves. The droplet cutoff ranges from 18 μm to 4 μm as the

ratio of liquid fluorescence to vapor fluorescence increases by a factor of 10. Because there are several effects going on, it is informative to compare the best case, worst case and a more likely case to show the range of potential values. The best case would have a large phosphorescence to fluorescence ratio (P/F = 9), a large liquid to vapor fluorescence ratio (F_{liquid}/F_{vapor} = 3), and a low vapor mole fraction (χ= 0.0525). This results in a droplet cutoff of less than 1 μm, which is highly desirable but also highly unlikely to occur. The worst case would reverse all of those values (P/F = 0, F_{liquid}/F_{vapor} = 0.3, f = 0.3) to the other extreme, and produces a cutoff size of 43 μm. The more likely case is obviously between the two, but closer to the worst case. Using P/F = 0.12, F_{liquid}/F_{vapor} = 1 and χ = 0.2 leads to a droplet cutoff of 15 μm. The largest factor ends up being the fluorescence ratio since the most pessimistic values of the phosphorescence to fluorescence ratio and mixture fraction are both fairly close to the most likely values. This was assumed to be 1 in the initial spray analysis, and may not be too far off.

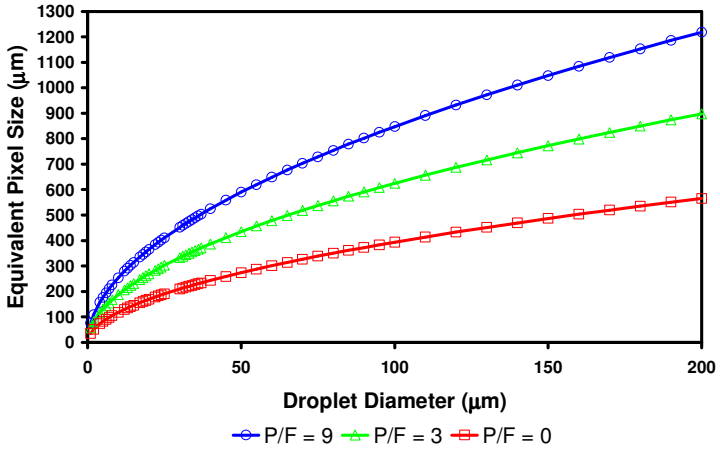

Figure 6.9. Equivalent pixel size versus droplet diameter for a range of liquid phosphorescence to fluorescence ratios.

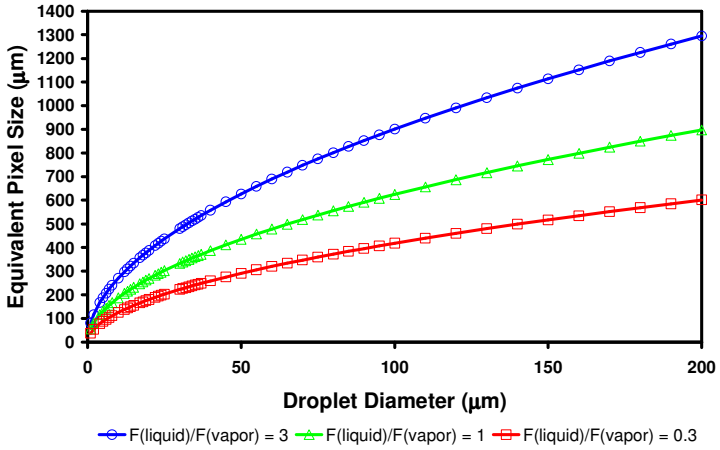

Figure 6.10. Equivalent pixel size versus droplet diameter for a range of liquid to vapor fluorescence ratios, assuming a phosphorescence to fluorescence ratio of 3.

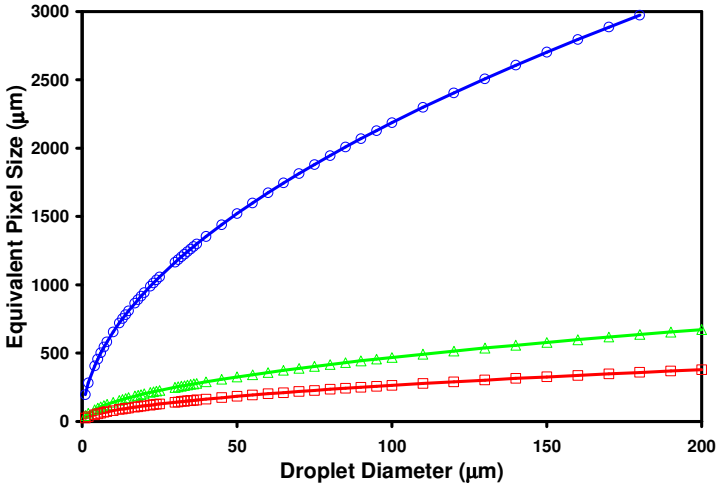

Figure 6.11. Equivalent pixel size versus droplet diameter for the best case, worst case and most likely case.

CHAPTER 7

CONCLUSIONS AND RECOMMENDATIONS

Conclusions

This investigation has introduced scalar mixing measurements for synthetic jet actuators enhancing jet mixing for the first time. Highly quantitative gaseous fuel-air mixing measurements (down to the resolution of the imaging system, <1 - 10 times the molecular mixing scale) were made in axisymmetric jet flow fields using planar laser-induced fluorescence of acetone. The image correction scheme employed here corrected for more errors than approaches previously reported for acetone PLIF, and allowed quantitative research at higher seeding levels that yield a larger signal to noise ratio, resulting in relative errors of less than 6%. It introduced a new level of accuracy for this proven measurement technique that allowed quantitative measurement, down to f = 0.005, of mixing enhancement induced by a relatively new type of actuator, synthetic jets.

Since two-phase flows are common for aerospace combustors, e.g., liquid-fueled combustors, the extension of quantitative PLIF of acetone to these flows is desirable. This investigation laid the foundation for two-phase mixing studies with acetone PLIF by showing the technique should work in at least dilute sprays. It may also be applicable to liquid jet breakup studies. While both the liquid and vapor phases of acetone emit light at

essentially the same wavelengths, signal level can be used to discriminate droplets from vapor, at least for droplets above some minimum (cutoff) value. A basic model of droplet fluorescence was created to provide estimates of the droplet fluorescence and the cutoff size. The value includes constants describing liquid and vapor photophysics. An important parameter that is not currently known with acceptable accuracy is the phosphorescence to fluorescence ratio for liquid acetone. Quantitative two-phase acetone PLIF, by reducing the cost and complexity to analyze two-phase flows, will provide a powerful new tool for the study of sprays, evaporation and mixing.

While the velocity fields induced by synthetic jets have been studied significantly, no previous mixing studies have been reported. The synthetic jet actuators, operating at high frequencies not related to natural instabilities in the flow, created visible small-scale structures in the outer mixing layers of all the jet flow fields. Similar structures were created in the inner mixing layer of the coaxial jet flows. These structures enhanced the mixing in the near field ($x/D \leq 1$) of the jets, but quickly dissipated. The mixing enhancement shortened the downstream distance required to mix the acetone-seeded stream down to a given level by approximately one jet diameter, but the unforced flows did catch up downstream. This rapid mixing enhancement would be useful for an off-design combustor condition requiring maximum mixing of the available fluids, such as a high altitude relight.

Imposing a low frequency amplitude modulation (again, not at a natural instability frequency) on the high frequency forcing of the synthetic jets generated large-scale structures, in addition to the small-scale structures produced by the high frequency, which was a novel forcing scheme. A comparison of the velocity field to the scalar field in the

amplitude modulated coaxial jets showed that the beginning of the modulation cycle generates a pinching of the core flow due to actuator suction followed by a large structure rolling outward due to the sudden appearance of the synthetic jets in the shear layer. These large coherent structures created broad regions of fluid uniformly mixed at some intermediate mixture fraction. While the amplitude modulation spread the mixing layer over a greater area for all the jet flows, the amount of mixing in the single jet compared to unmodulated forcing was reduced. The modulation increased the amount of mixing in the coaxial jets, and was especially effective for $x/D_o > 1$, indicating the reduction in the single jet case was likely due to an entrainment limitation. This indicates that the synthetic jets are best used in a design with multiple mixing layers, like a typical combustor, where they can enhance mixing in many locations simultaneously.

The inner mixing layer (for the coaxial jets) was less influenced by amplitude modulation than the outer layer, yielding similar results under both forms of actuation, and the unmodulated case mixed faster to the centerline than the modulated case. A comparison of different velocity ratios in the coaxial jets found that the small-scale structures were more effective in both mixing layers the faster the annulus was moving. These results imply that the best choice for mixing enhancement would involve actuators radially located between the centerline and the wall, a control scheme that can vary the choice of actuators and the forcing amplitude, and flows with strong shear layers. Highly asymmetric actuation schemes created significant distortion of the flow field cross-section. The 6 on configuration demonstrated the ability to divert the jet fluid to one side, while a spinning amplitude modulation of the configuration induced a swirl velocity.

Based on the range of abilities the synthetic jets demonstrated in this investigation, they are a promising technology for mixing control and enhancement. For operation near the flammability limit, synthetic jets could provide the mixing needed for flame stabilization. At near-stoichiometric operation, they could be used to help limit NO_x production. The ability to shorten the downstream distance required for mixing is useful for nonpremixed combustion applications. Spatially redirecting the main jet flow could aid in compensating for a plugged fuel injector, or reducing hot spots in the turbine pattern factor.

Recommendations for Future Work

This study answered several questions about the effectiveness of synthetic jets for mixing enhancement in axisymmetric jets, but there are some issues worthy of future study and some different approaches of interest. Due to the increase in computational power and storage capacity, it would helpful to acquire full images instead of image slices. Full images capture entire structures and allow for some spatial correlations for which slices do not provide sufficient data. An extension of the range of flow fields would also be useful. One suggested change is to enclose the flow and evaluate the impact of walls on the enhancement.

While this study did not aim to optimize the actuation, that clearly should be investigated. One facet of actuation that received no attention was varying the strength of the actuators relative to the flows. Changes to consider are the power driving the actuators, the actuator exit size/shape and the flow velocities. Radial actuation should be

re-examined, especially with a shorter downstream distance between the synthetic jet exits and the jet exit plane than existed in this investigation. This distance limited the ability of the actuators to mix air into the jet fluid. Based on the results here, radial actuation in coaxial jets should prove more effective as well. A range of frequencies for the actuators need examination, especially the medium frequency (200-400 Hz) range that would persist farther downstream than the high frequency and cause more direct mixing enhancement than the low frequency.

In addition, some different actuation patterns should be investigated. Amplitude modulation might work better not as a binary cycle (on/off) but with an intermediate value so the small scales are always present. Instead of spinning a pattern around, rotating the pattern one actuator in each direction might create a larger area for the mixing layer. Modulating only some of the actuators while the others run continuously and modulating groups of actuators at different frequencies are two other suggestions to evaluate the capabilities of the actuators. A study capable of axisymmetric forcing should also be investigated.

The most important future work will be to study these actuators in reacting systems. The heat release will disturb the flowfield from the cold flow measurements, and the ability of the synthetic jets to control the mixing for a real combustor is still unproven. Based on the measurements here, such as the mixture fraction contours (Figure 5.22) and the pure fluid measurements (Figure 5.4, Figure 5.19), the actuators should be very useful for nonpremixed combustors, where mixing is at a premium, and should be evaluated in one.

To enable the development of quantitative acetone PLIF for two-phase flows, the photophysics of liquid acetone require further study. Accurate values for the fluorescence and phosphorescence yields from liquid acetone, as a function of the relevant variables (T, p, λ, ambient gases), are crucial to the development of this technique. The droplet model needs to become more detailed and the technique calibrated. A proper algorithm should also be created to size droplets below the cutoff diameter when they are visually distinct from the vapor signal using the improved model.

REFERENCES

[1] Hill, P. and Peterson, C., "Aerothermodynamics of Inlets, Combustors, and Nozzles," Chapter 5 in Mechanics and Thermodynamics of Propulsion 2nd Edition, Addison-Wesley Publishing Company, 1992.

[2] Tang, S. K. and Ko, N. W. M., "Experimental Investigation of the Structure Interaction in an Excited Coaxial Jet," Experiemental Thermal and Fluid Science 8, 214-229, 1994.

[3] Long, T. A. and Petersen, R. A., "Controlled Interactions in a Forced Axisymmetric Jet. Part 1. The Distortion of the Mean Field," Journal of Fluid Mechanics 253, 37-55, 1992.

[4] Wicker, R. B. and Eaton, J. K., "Near Field of a Coaxial Jet With and Without Axial Excitation," AIAA Journal 32, 542-546, 1994.

[5] Smith, B. L. and Glezer, A., "Vectoring and Small-Scale Motions Effected in Free Shear Flows Using Synthetic Jet Actuators," AIAA Paper 97-0213, 35th AIAA Aerospace Sciences Meeting and Exhibit, January 1997, Reno, NV.

[6] Smith, B. L. and Glezer, A., "The Formation and Evolution of Synthetic Jets," Physics of Fluids 10, 2281-2297, 1998.

[7] Wiltse, J. M. and Glezer, A., "Direct Excitation of Small-Scale Motions in Free Shear Flows," Physics of Fluids 10, 2026-2036, 1998.

[8] Chen, Y., Liang, S., Aung, K., Glezer, A. and Jagoda, J., "Enhanced Mixing in a Simulated Combustor Using Synthetic Jet Actuators," AIAA Paper 99-0449, 37th AIAA Aerospace Sciences Meeting and Exhibit, January 1999, Reno, NV.

[9] Rizzeta, D. P., Visbal, M. R. and Stanek, M. J., "Numerical Investigation of Synthetic-Jet Flowfields," AIAA Journal 37, 919-927, 1999.

[10] Lee, C. Y. and Goldstein, D. B., "Two-Dimensional Synthetic Jet Simulation," AIAA Journal 40, 510-516, 2002.

[11] Freund, J. B., and Moin, P., "Jet Mixing Enhancement by High-Amplitude Fluidic Actuation," AIAA Journal 38, 1863-1870, 2000.

[12] Wang, H. and Menon, S., "Fuel-Air Mixing Enhancement by Synthetic Microjets," AIAA Journal 39, 2308-2319, 2001.

[13] Davis, S. A., "The Manipulation of Large- and Small-Scale Flow Structures in Single and Coaxial Jets Using Synthetic Jet Actuators," Ph. D. dissertation, School of Mechanical Engineering, Georgia Institute of Technology, 2000.

[14] Lockwood, F. C. and Moneib, H. A., "Fluctuating Temperature Measurements in a Heated Round Free Jet," Combustion Science and Technology 22, 63-81, 1980.

[15] Becker, H. A., Hottel, H. C. and Williams, G. C., "The Nozzle-Fluid Concentration Field of the Round, Turbulent, Free Jet," Journal of Fluid Mechanics 30, 285-303, 1967.

[16] Dimotakis, P. E., Miake-Lye, R. C. and Papantoniou, D. A., "Structure and Dynamics in the Near Field of a Coaxial Jet," Physics of Fluids 26, 3185-3192, 1983.

[17] Feikema, D. A., Everest, D. and Driscoll, J. F., "Images of Dissipation Layers to Quantify Mixing Within a Turbulent Jet," AIAA Journal 34, 2531-2538, 1996.

[18] King, G. F., Dutton, J. C. and Lucht, R. P., "Instantaneous, Quantitative Measurements of Molecular Mixing in the Axisymmetric Jet Near Field," Physics of Fluids 11, 403-416, 1999.

[19] Meyer, T. R., Dutton, J. C. and Lucht, R. P., "Vortex Interaction and Mixing in a Driven Gaseous Axisymmetric Jet," Physics of Fluids 11, 3401-3415, 1999.

[20] Broadwell, J. E. and Briedenthal, R. E., "A Simple Model of Mixing and Chemical Reaction in a Turbulent Shear Layer," Journal of Fluid Mechanics 125, 397-410, 1982.

[21] Ko, N. W. M. and Kwan, A. S. H., "The Initial Region of Subsonic Coaxial Jets," Journal of Fluid Mechanics 73, 305-332, 1976.

[22] Dahm, W. J. A., Frieler, C. E. and Tryggvason, G., "Vortex Structure and Dynamics in the Near Field of a Coaxial Jet," Journal of Fluid Mechanics 241, 371-402, 1992.

[23] Ribeiro, M. M. and Whitelaw, J. H., "Coaxial Jets With and Without Swirl," Journal of Fluid Mechanics 96, 769-795, 1980.

[24] Champagne, F. H. and Wygnanski, I. J., "An Experimental Investigation of Coaxial Turbulent Jets," International Journal of Heat and Mass Transfer 14, 1445-1464, 1971.

[25] Eckbreth, A. C., Laser Diagnostics for Combustion Temperature and Species, Gordon and Breach Publishers, Amsterdam, 1996.

[26] Miles, R. B., "Flow-Field Diagnostics," Chapter 7 in Applied Combustion Diagnostics, ed. K. Kohse-Höinghaus and J. B. Jeffries, Taylor & Francis, New York, 2002.

[27] Marques, Jr., S. J., "Passive Scalar Measurements in Actively Excited Free Shear Flows," Master's thesis, Department of Mechanical Engineering, Virginia Polytechnic Institute and State University, 1998.

[28] Seitzman, J. M. and Hanson, R. K., “Planar Fluorescence Imaging in Gases,” Chapter 6 in Instrumentation for Flows with Combustion, ed. A. M. K. P. Taylor, Academic Press, London, 1993.

[29] van Cruyningen, I., "Quantitative Imaging of Turbulent Gaseous Jets Using Planar Laser-Induced Fluoerscence," Ph. D. dissertation, Department of Mechanical Engineering, Stanford University, 1990.

[30] Lozano, A., Yip, B. and Hanson, R. K., "Acetone: A Tracer for Concentration Measurements in Gaseous Flows by Planar Laser-Induced Fluorescence," Experiments in Fluids 13, 369-376, 1992.

[31] Lozano, A., Smith, S. H., Mungal, M. G. and Hanson, R. K., "Concentration Measurements in a Transverse Jet by Planar Laser-Induced Fluorescence of Acetone," AIAA Journal 32, 218-221, 1994.

[32] Lempert, W. R., Jiang, N., Sethuram, S. and Samimy, M., "Molecular Tagging Velocimetry Measurements in Supersonic Microjets," AIAA Journal 40, 1065-1070, 2002.

[33] Thurber, M. C., Grisch, F. and Hanson, R. K., "Temperature Imaging with Single- and Dual-Wavelength Acetone PLIF," AIAA Paper 96-2936, 32nd AIAA/ASME/SAE/ASEE Joint Propulsion Conference, July 1996, Lake Buena Vista, FL.

[34] Thurber, M. C., Kirby, B. J., Grisch, F. and Hanson, R. K., "Instantaneous Temperature Imaging with Single-Wavelength Acetone PLIF," AIAA Paper 97-0151, 35th AIAA Aerospace Sciences Meeting and Exhibit, January 1997, Reno, NV.

[35] Thurber, M. C., Grisch, F. and Hanson, R. K., "Temperature Imaging with Single- and Dual-Wavelength Acetone Planar Laser-Induced Fluorescence," Optics Letters 22, 251-253, 1997.

[36] Thurber, M. C., Kirby, B. J. and Hanson, R. K., "Instantaneous Imaging of Temperature and Mixture Fraction with Dual-Wavelength Acetone PLIF," AIAA Paper 98-0397, 36th AIAA Aerospace Sciences Meeting and Exhibit, January 1998, Reno, NV.

[37] Yip, B., Miller, M. F., Lozano, A. and Hanson, R. K., "A Combined OH/Acetone Planar Laser-Induced Fluorescence Imaging Technique for Visualizing Combusting Flows," Experiments in Fluids 17, 330-336, 1994.

[38] Grisch, F., Bresson, A., Bouchardy, P. and Attal-Tretout, B., "Advanced Optical Diagnostics Applied to Dynamic Flames and Turbulent Jets," Aerospace Science and Technology 6, 465-479, 2002.

[39] Thurber, M. C., "Acetone Laser-Induced Fluorescence for Temperature and Multiparameter Imaging in Gaseous Flows," Ph. D. dissertation, Department of Mechanical Engineering, Stanford University, 1999.

[40] Thurber, M. C. and Hanson, R. K., "Simultaneous Imaging of Temperature and Mole Fraction Using Acetone Planar Laser-Induced Fluorescence," Experiments in Fluids 30, 93-101, 2001.

[41] Bryant, R. A., Donbar, J. M. and Driscoll, J. F., "Acetone LIF for Flow Visualization at Temperatures Below 300 K," AIAA Paper 97-0156, 35th AIAA Aerospace Sciences Meeting and Exhibit, January 1997, Reno, NV.

[42] Thurber, M. C., Grisch, F., Kirby, B. J., Votsmeier, M. and Hanson, R. K., "Measurements and Modeling of Acetone Laser-Induced Fluorescence with Implications for Temperature-Imaging Diagnostics," Applied Optics 37, 4963-4978, 1998.

[43] Grossman, F., Monkhouse, P. B., Ridder, M., Sick, V. and Wolfrum, J., "Temperature and Pressure Dependences of the Laser-Induced Fluorescence of Gas-Phase Acetone and 3-Pentanone," Applied Physics B Lasers and Optics 62, 249-253, 1996.

[44] Thurber, M. C. and Hanson, R. K., "Pressure and Composition Dependences of Acetone Laser-Induced Fluorescence with Excitation at 248, 266, and 308 nm," Applied Physics B Lasers and Optics 69, 229-240, 1999.

[45] Hodges, J. T., Baritaud, T. A. and Heinze, T. A., "Planar Liquid and Gas Fuel and Droplet Size Visualization in a DI Diesel Engine," SAE Technical Paper 910726, 1991.

[46] Diwakar, R., Fansier, T. D., French, D. T., Ghandhi, J. B., Dasch, C. J. and Heffelfinger, D. M., "Liquid and Vapor Fuel Distributions from an Air-Assist Injector – An Experimental and Computational Study," SAE Technical Paper 920422, 1992.

[47] Senda, J., Fukami, Y., Tanabe, Y. and Fujimoto, H., "Vizualization of Evaporative Diesel Spray Impinging Upon Wall Surface by Exciplex Fluorescence Method," SAE Technical Paper 920578, 1992.

[48] Fansier, T. D., French, D. T. and Drake, M. C., "Fuel Distributions in a Firing Direct-Injection Spark-Injection Engine Using Laser-Induced Fluorescence Imaging," SAE Technical Paper 950110, 1995.

[49] Bazile, R. and Stepowski, D., “Measurements of Vaporized and Liquid Fuel Concentration in a Burning Spray Jet of Acetone Using Planar Laser Induced Fluorescence,” Experiments in Fluids 20, 1-9, 1995.

[50] Hunt, R. E. and Noyes, Jr., W. A., "Photochemical Studies. XXXIX. A Further Study of the Fluorescence of Acetone," Journal of the American Chemical Society 70, 467-476, 1948.

[51] Heicklen, J. and Noyes, Jr., W. A., "The Photolysis and Fluorescence of Acetone and Acetone-Biacetyl Mixtures," Journal of the American Chemical Society 81, 3858-3863, 1959.

[52] Heicklen, J., "The Fluorescence and Phosphorescence of Biacetyl Vapor and Acetone Vapor," Journal of the American Chemical Society 81, 3863-3866, 1959.

[53] Johnston, H. S. and Heicklen, J., "Photochemical Oxidations. III. Acetone," Journal of the American Chemical Society 86, 4249-4254, 1964.

[54] Cundall, R. B. and Davies, A. S., "The Mechanism of the Gas Phase Photolysis of Acetone," Proceedings of the Royal Society of London A 290 n1423, 563-582, 1966.

[55] Gandini, A. and Kutschke, K. O., "The Primary Process in the Photolysis of Hexafluoroacetone Vapour. II. The Fluoresence and Phosphorescence, Proceedings of the Royal Society of London A 306 n1487, 511-528, 1968.

[56] O'Neal, H. E. and Larson, C. W., "Primary Processes in the Acetone Photochemical System," Journal of Physical Chemistry 73, 1011-1022, 1969.

[57] O'Sullivan, M. and Testa, A. C., "Fluorescence of Aliphatic Ketones," Journal of the American Chemical Society 92, 5842-5844, 1970.

[58] Breuer, G. M. and Lee, E. K. C., "Fluorescence Decay Times of Cyclic Ketones, Acetone, and Butanal in the Gas Phase," Journal of Physical Chemistry 75, 989-990, 1971.

[59] Gandini, A. and Hackett, P. A., "Electronic Relaxation Processes in Acetone and 1,1,1-trifluoroacetone Vapor and the Gas Phase Recombination of the Acetyl Radical at 22 Degrees C," Journal of the American Chemical Society 99, 6195-6205, 1977.

[60] Baba, M. and Hanazaki, I., "The S/sub 1/, /sup 1/A/sub 2/(n, pi *) State of Acetone in a Supersonic Nozzle Beam. Methyl Internal Rotation," Chemical Physics Letters 103, 93-97, 1983.

[61] Greenblatt, G. D., Ruhman, S. and Haas, Y., "Fluorescence Decay Kinetics of Acetone Vapour at Low Pressures," Chemical Physics Letters 112, 200-206, 1984.

[62] Copeland, R. A. and Crosley, D. R., "Radiative, Collisional and Dissociative Processes in Triplet Acetone," Chemical Physics Letters 115, 362-368, 1985.

[63] Costela, A., Crespo, M. T. and Figuera, J. M., "Laser Photolysis of Acetone at 308 nm," Journal of Photochemistry 34, 165-173, 1986.

[64]Zuckermann, H., Schmitz, B. and Haas, Y., "The Radiative Lifetime of Acetone: Resolution of an Apparent Discrepancy," Chemical Physics Letters 151, 323-327, 1988.

[65] Zuckermann, H., Schmitz, B. and Haas, Y., "Acetone Photophysics in Seeded Supersonic Molecular Beams," Journal of Physical Chemistry 93, 4083-4091, 1989.

[66] Zuckermann, H., Schmitz, B. and Haas, Y., "Dissociation Energy of an Isolated Triplet Acetone Molecule," Journal of Physical Chemistry 92, 4835-4837, 1988.

[67] Borge, M. J. G., Figuera, J. M. and Luque, J., "Study of the Emission of the Excited Acetone Vapour at Intermediate Pressures," Spectrochimica Acta 46A, 617-621, 1990.

[68] Lozano, A., "Laser-Excited Luminescent Tracers for Planar Concentration Measurements in Gaseous Jets," Ph. D. dissertation, Department of Mechanical Engineering, Stanford University, 1992.

[69] Borkman, R. F. and Kearns, D. R., "Triplet-State Energy Transfer in Liquid Solutions. Acetone-Photosensitized cis-trans Isomerization of Pentene-2," Journal of the American Chemical Society 88, 3467-3475, 1966.

[70] O'Sullivan, M. and Testa, A. C., "Monomer and Excimer Emission of Acetone," Journal of the American Chemical Society 90, 6245-6246, 1968.

[71] Dalton, J. C. and Turro, N. J., "Determination of the Reactivity of First Excited Singlet States of Organic Compounds toward Unimolecular Primary Photochemical Processes from Molecular Fluorescence Characteristics. Application to Intramolecular Gamma-Hydrogen Abstraction Reactions of Alkyl Ketones," Journal of the American Chemical Society 93, 3569-3570, 1971.

[72] Halpern, A. M. and Ware, W. R., "Excited Singlet State Radiative and Nonradiative Transition Probabilities for Acetone, Acetone-d_6, and Hexafluoroacetone in the Gas Phase, in Solution, and in the Neat Liquid," Journal of Chemical Physics 54, 1271-1276, 1971.

[73] Turro, N. J., Steinmetzer, H.-C. and Yekta, A., "Tetramethyl-1,2-dioxetane. Simple Procedures for Chemiexcitation or Photoexcitation of Acetone Phosphorescence in Fluid Solution," Journal of the American Chemical Society 95, 6468-6470, 1973.

[74] Turro, N. J., Lechtken, P., Schore, N. E., Schuster, G., Steinmetzer, H.-C. and Yekta, A., "Tetramethyl-1,2-dioxetane. Experiments in Chemiexcitation, Chemiluminecence, Photochemistry, Chemical Dynamics, and Spectroscopy," Accounts of Chemical Research 7, 97-105, 1974.

[75] van de Hulst, H. C., Light Scattering by Small Particles, Dover Publications, New York, 1981.

[76] Pitts, W., "Resolution Requirements for Scalar Dissipation Measurements in Turbulent Jets and Flames," Proceedings of the 52nd Annual Meeting of the Division of Fluid Dynamics of the American Physical Society, 37, New Orleans, LA, 1999.

[77] Buch, K. A. and Dahm, W. J. A., "Fine Scale Structure of Conserved Scalar Mixing in Turbulent Shear Flows: Sc >> 1, Sc ≈ 1 and Implications for Reacting Flows," Report 026779-5, University of Michigan, 1991.

[78] Lefebvre, A. H., "Atomizer Performance," Chapter 6 in Atomization and Sprays, Hemisphere Publishing, 1989.

[79] Bortolus, P., Dellonte, S., Faucitano, A and Gratani, F., "Photostabilizing Mechanisms of Hindered-Amine Light Stabilizers: Interaction with Electronically Excited Aliphatic Carbonyls," Macromolecules, 19, 2916-2922, 1986.

[80] Pischel, U. and Nau, W. M., "Switch-Over in Photochemical Reaction Mechanism from Hydrogen Abstraction to Exciplex-Induced Quenching: Interaction of Triplet-Excited versus Singlet-Excited Acetone versus Cumyloxyl Radicals with Amines," Journal of the American Chemical Society 123, 9727-9737, 2001.

[81] Tran, T., Kochar, Y. and Seitzman, J., "Measurements of Liquid Acetone Fluorescence and Phosphorescence for Two-Phase Fuel Imaging," AIAA Paper 2005-0827, 43rd AIAA Aerospace Sciences Meeting and Exhibit, January 2005, Reno, NV.

[82] Tran, T., Kochar, Y. and Seitzman, J., "Measurements of Acetone Fluorescence and Phosphorescence at High Pressures and Temperatures," AIAA Paper 2006-0831, 44th AIAA Aerospace Sciences Meeting and Exhibit, January 2006, Reno, NV.